HZDR-088

INVESTIGATION OF DECOMMISSIONED REACTOR PRESSURE VESSELS OF THE NUCLEAR POWER PLANT GREIFSWALD

Hans-Werner Viehrig, Eberhard Altstadt, Mario Houska, Gudrun Mueller, Andreas Ulbricht, Joerg Konheiser, Matti Valo

Wissenschaftlich-Technische Berichte
HZDR-088 · ISSN 2191-8708

WISSENSCHAFTLICH-
TECHNISCHE BERICHTE

HZDR
HELMHOLTZ
ZENTRUM DRESDEN
ROSSENDORF

Wissenschaftlich-Technische Berichte
HZDR-088

Hans-Werner Viehrig, Eberhard Altstadt, Mario Houska,
Gudrun Mueller, Andreas Ulbricht,
Joerg Konheiser, Matti Valo

INVESTIGATION OF DECOMMISSIONED REACTOR PRESSURE VESSELS OF THE NUCLEAR POWER PLANT GREIFSWALD

HZDR

HELMHOLTZ
ZENTRUM DRESDEN
ROSSENDORF

Druckausgabe: ISSN 2191-8708

Elektronische Ausgabe: ISSN 2191-8716

https://www.hzdr.de/publications/Publ-27130

urn:nbn:de:bsz:d120-qucosa-235681

2018

Herausgegeben vom

Helmholtz-Zentrum Dresden - Rossendorf

Bautzner Landstraße 400

01328 Dresden

Germany

Investigation of decommissioned reactor pressure vessels of the nuclear power plant Greifswald

Hans-Werner Viehrig*, Eberhard Altstadt*, Mario Houska*, Gudrun Mueller*, Andreas Ulbricht*, Joerg Konheiser* and Matti Valo**

* Helmholtz-Zentrum Dresden-Rossendorf, Bautzner Landstraße 400, 01328 Dresden, Germany

** MAV Consulting, Toolontullinkatu 7A24, 00250 Helsinki, Finland.

Abstract

The investigation of reactor pressure vessel (RPV) material from the decommissioned Greifswald nuclear power plant representing the first generation of Russian-type WWER-440/V-230 reactors offered the opportunity to evaluate the real toughness response. The Greifswald RPVs of 4 units represented different material conditions as follows:

- Irradiated (Unit 4),
- irradiated and recovery annealed (Units 2 and 3) and
- irradiated, recovery annealed and re-irradiated (Unit1).

The recovery annealing of the RPV was performed at a temperature of 475° for about 152 hours and included a region covering ±0.70 m above and below the core beltline welding seam.

Material samples of a diameter of 119 mm called trepans were extracted from the RPV walls. The research program is focused on the characterisation of the RPV steels (base and weld metal) across the thickness of the RPV wall. This report presents test results measured on the trepans from the beltline welding seam No. SN0.1.4. and forged base metal ring No. 0.3.1. of the Units 1, 2 and 4 RPVs. The key part of the testing is focussed on the determination of the reference temperature T_0 of the Master Curve (MC) approach following the ASTM standard E1921 to determine the fracture toughness, and how it degraded under neutron irradiation and was recovered by large scale thermal annealing. Other than that the mentioned test results included hardness, Charpy-V and tensile testing and small angle neutron scattering (SANS) measurements. Following results have been determined:

- K_{Jc} values of the weld metals from the beltline welding seam SN0.1.4. generally followed the course of the MC though with a large scatter.
- There was a large variation in the T_0 values evaluated across the thickness of the multilayer welding seams. Generally, the progression of the T_0 values through the thickness of the welding seam was not in accordance with the current understanding of what could be expected - a decrease in T_0 with the attenuation of the neutron fluence.
- Generally, the volume fraction of irradiation induced clusters measured by SANS decreased with the attenuation of the neutron loading through the thickness of the beltline welding seam SN0.1.4. of the Unit 4 RPV. An exception was a thickness location towards the RPV outer wall, where also the highest T_0 was measured, the volume fraction of clusters and the hardness was locally higher.
- The T_0 measured on T-S oriented SE(B) specimens from different thickness locations of the welding seams strongly depended on the intrinsic structure along the crack front.
- The reference temperature RT_0 determined according to the "Unified Procedure for Lifetime Assessment of Components and Piping in WWER NPPs - VERLIFE" and the fracture toughness lower bound curve based thereon are applicable on the investigated weld metals.
- A strong scatter of the fracture toughness K_{Jc} values of the recovery annealed and re-irradiated and the irradiated base metal of Unit 1 and 4, respectively is observed with clearly more than 2% of the values below the MC for 2% fracture probability. The application of the multimodal MC-based approach was more suitable and described the temperature dependence of the K_{Jc} values in a satisfactory manner.

- It was demonstrated that T_0 evaluated according to the SINTAP MC extension represented the brittle fraction of the data sets and is therefore suitable for the nonhomogeneous base metal.
- The efficiency of the large-scale thermal annealing of the Greifswald WWER 440/V230 Unit 1 and 2 RPVs could be confirmed by the test results and SANS measurements.
- The main focus in the investigation of the cladding of the Unit 4 RPV was on the measurement of J vs. Δa curves by using the unloading compliance technique and the evaluation of initiation fracture toughness values according to the test standard ASTM E1820.
- The fracture toughness of the cladding is reduced by intercrystalline fracture at low temperature and the decreasing yield strength at high temperature. This resulted in a maximum of the interim initiation fracture toughness values, K_{JQ}, in the temperature range between ambient temperature and 80 °C.
- Based on the measured results, it can be concluded that the overlay cladding of the Greifswald Unit 4 RPV would remain intact and increase confidence in the safety of the structural integrity of the RPV after the operation up to 25 % of the designed neutron loading for 30 full power years.

Contents

Nomenclature

A	fitting parameter of the tanh model for modelling Charpy impact energy vs. temperature curves: the mean energy level between the upper and lower shelves
A_F^T	irradiation embrittlement factor according to the Russian code [PNAE G-1986] for irradiation at temperature T, °C,
a	crack depth (small half axis of the ellipse)
a_i	actual crack length determined by unloading compliance
a_0	initial crack length
a_{0q}	initial crack length estimated according to ASTM E1820 with the a_i values up to maximum load
B	specimen thickness
B	fitting parameter of the tanh model for modelling Charpy impact energy vs. temperature curves: the plus or minus deviation from the mean energy level
b	temperature independent material constant of the $\sigma_{YS}(T)$ fit
bcc	body centred cubic
C	fitting parameter of the tanh model for modelling Charpy impact energy vs. temperature curves: the plus or minus deviation of the intercepts of the tangent to the transition of T_0 and the upper and lower shelves
c	large half axes of the ellipse
c	volume fraction of irradiation induced clusters obtained by SANS
COD	crack opening displacement
DBTT	ductile-to-brittle transition temperature
E	Young's modulus
E_{eff}	effective E-modulus determined with the unloading compliance technique according to ASTM E1820
FEM	finite element method
F_n:	neutron fluence, E > 0.5 MeV, n/m^2
F_0:	10^{22}, n/m^2
h	temperature independent material constant of the $\sigma_{YS}(T)$ fit
ICP MS	inductively coupled plasma mass spectrometry
J_c	J-integral at the onset of cleavage fracture
J_R	crack extension curve fitted with J - Δa data according to ASTM E1820
J_Q	interim J integral according to ASTM E1820 at 0.2 mm crack extension excluding blunting
J_{Ic}	J_Q becomes J_{Ic} when properly qualified against the criteria proposed in the test standard procedure ASTM E1820
K_f	final stress intensity factor according to ASTM E1921 applied during precracking
K_{JIc}	J_{Ic} based fracture toughness according to ASTM E1820
K_{Jc}	elastic-plastic equivalent stress intensity factor derived from the J-integral at the point of onset of cleavage fracture, J_c
$K_{Jc\text{-}1T}$	K_{Jc} adjusted to a specimen thickness of 1T (25.4 mm)
$K_{Jc(med)}$	median fracture toughness according to ASTM E1921 for a single or multi-temperature data set
K_{JQ}	J_Q based fracture toughness according to ASTM E1820

KLST	sub sized impact specimen (dimension: 3 mm · 4 mm · 27 mm)
K_{max}	maximum stress intensity factor according to ASTM E1921 applied during precracking
KV_2	absorbed energy for a V-notched test piece using a 2 mm striker
K_I	stress intensity factor
LSC	liquid scintillation counting
LLD	load line deflection
MC	Master Curve
MLNH	maximum likelihood non-homogeneous criteria
MM	multi modal Master Curve approach
N	total number of uncensored and censored K_{Jc} data in ASTM E1921
N	number density of irradiation induced clusters obtained by SANS
NPP	nuclear power plant
Q	scattering vector
r	number of uncensored K_{Jc} data in ASTM E1921
R	reconstituted specimen
R_{mean}	mean radius of irradiation induced clusters obtained by SANS
R_m	ultimate tensile strength
RPV	reactor pressure vessel
$R_{p0.2}$	proof strength at 0.2% plastic deformation
PTS	pressurized thermal shock
RT_0	reference temperature of the VERLIFE lower bound fracture toughness curve
RT_0^{SINTAP}	reference temperature based on T_0 determined according to the SINTAP MC extension
s	thickness of the cladding
SANS	Small-angle neutron scattering
SD	standard deviation
SE(B)	single edge bend specimen
SIF	stress intensity factor
T	Temperature in K
T	thickness of the RPV wall
T	thickness of a specimen 1T = 1 inch
T_K	critical embrittlement temperature according to the Russian code [PNAE G-1986]
T_{K0}	critical embrittlement temperature for the initial condition according to the Russian code [PNAE G-1986]
T_0	reference temperature according to ASTM E1921
T_0	fitting parameter of the tanh model for modelling Charpy impact energy vs. temperature curves: it represents the mid energy transition temperature
T_0^{MM}	reference temperature determined according to the multi modal MC approach
$T_0^{SINTAP-3}$	reference temperature determined according to step 3 of the SINTAP MC extension
TT_{41J}	DBTT related to a Charpy energy of 41 J
TT_{47J}	DBTT related to a Charpy energy of 47 J
UC	unloading compliance technique
W	specimen width

WWER	Russian type pressurized water reactor (water operated and moderated)
β	refers to the determination of standard deviation in ASTM E1921
Φ	neutron fluence
Δa	crack propagation
ΔT_F:	shift of the critical embrittlement temperature due to irradiation
ΔT_T:	shift of the critical embrittlement temperature due to thermal aging
ΔT_N:	shift of the critical embrittlement temperature due to cyclic damage
σ	margin
σ	uniform hoop stress
σ_{exp}	experimental uncertainty on the MC reference temperature T_0 and may be taken as 4 K.
σ^{MM}	standard deviation of the multi modal MC approach,
σ_Y	yield stress
$\sigma_{YS}(T)$	temperature-dependent component of the yield stress
σ_{YG}	temperature-independent component of the yield stress
δT_M	margin of the VERLIFE procedure considering a possible uncertainty of the material
δT_{type}	margin of the VERLIFE procedure considering the bias of the specimen type

Introduction

Nuclear power plant (NPP) operators must demonstrate that the structural integrity of a nuclear reactor pressure vessel (RPV) is assured during routine operations and under postulated accident conditions. The aging of the RPV steels is monitored by surveillance programs or predicted by trend curves. The actual Russian [PNAE-1986, Brumovsky-2005, -2018a] and international codes [ASME NB-2300, KTA 3201.2] for the RPV integrity assessment applies indirect and correlative approaches to determine the fracture toughness of RPV steels in the initial and irradiated condition. These indirect and correlative approaches use Charpy V-notch transition temperatures shifts as the measure of radiation embrittlement. Embrittlement forecast with trend curves and surveillance specimens may not reflect the reality. Accordingly, the most realistic evaluation of the toughness response of RPV material to irradiation is done directly on RPV wall samples from decommissioned NPPs. Such an opportunity was offered with material from the decommissioned Greifswald NPP. The Greifswald WWER-440/V-230 nuclear reactors represent the first generation of this Russian-type. The RPVs were designed by OKB Gidropress and manufactured by the Izhora Plant in the former Soviet Union at the end of the 1960s and the beginning of the 1970s. The aging of the RPV steels was not monitored with surveillance specimen program and the embrittlement forecast for these RPVs is based on trend curves. The four Greifswald NPP units were shut down in 1990 after 11 to 15 years of operation [Boehmer-1999, Konheiser-2006].

Table 1 presents the operation characteristics of the units 1 to 4 and the expected neutron fluences. RPVs in three different conditions are available:

- the uncladded RPV of Unit 1 is irradiated, annealed and re-irradiated (IAI),
- the uncladded RPV of Unit 2 is irradiated and annealed (IA),
- the cladded RPV of Unit 3 is irradiated and annealed (IA), and
- the cladded RPV of Unit 4 is irradiated (I).

The circumferential beltline welding seam No. SN0.1.4. and a region of 0.7 m above and below of the units 1 to 3 RPVs were subjected to a heat treatment at 475°C for 152 hours in order to mitigate the irradiation embrittlement (Table 1). Unit 1 was operated for additional 2 campaigns, whereas Units 2 and 3 were not put in operation after the annealing.

Table 1: Operation characteristics and estimated maximum accumulated neutron fluences of Greifswald Units 1 to 4 [Boehmer 1999].

unit	operation period		effective days	annealed in	$\phi_{E>0.5MeV}$ in 10^{18} n/cm^2	
	date	cycles			inner wall axial maximum	inner wall weld SN0.1.4
1	1974-1988	13	4205.0	1988	68.5	57.2
1*	1988-1990	2	627.4	-	2.8	2.3
2	1975-1990	14	4067.4	1990	85.2	72.3
3	1978-1990	12	3581.8	1990	71.2	60.6
4	1979-1990	11	3207.9	not	64.3	54.7

* re-irradiated

Trepans were extracted from the decommissioned Unit 1, 2 and 4 RPVs. The investigation programme has been finished. This report presents a summary of the test results measured on

the trepans sampled from the beltline welding seam and forged base metal ring of the RPV's of Greifswald Unit 1, 2 and 4.

The main focus of the investigations is on the application of the Master Curve (MC) approach on the sampled materials with following key aspects:

- the determination of the reference temperature T_0 following the ASTM Test Standard E1921 to determine the fracture toughness,
- how T_0 varies through the thickness of the multi-layer beltline welding seam and the forged base metal ring after irradiation and recovery annealing,
- application of the European "Unified Procedure for Lifetime Assessment of Components and Piping in WWER NPPs - VERLIFE" [VERLIFE-2012, Brumovsky-2018a], which directly utilizes the fracture toughness measured according to ASTM E1921,
- with additionally determined tensile strength and Charpy-V impact test parameters the current WWER RPV integrity assessment code PNAE G-7-008-86 [PNAEG-1986] is also assessed, and
- investigation of the irradiation behaviour of the austenitic cladding.

Optical metallographic and scanning electron microscopic investigations on fractured surfaces of the specimens were performed to interpret the fracture toughness values and the associated reference temperature T_0 through the welding seam and the forging. In addition SANS investigations were performed to investigate irradiation induced microstructural changes.

Integrity Assessment of the WWER-400 RPV

The WWER-440 RPVs belong to the normal operation system, seismic Class I and are designed for safe and reliable operation for 30 effective full-power years (Table 2).

Table 2: Effective full-power years fluence of WWER-440 RPV [Brumovsky-2005].

beltline RPV material	Neutron flux n/m^2s (E > 0.5 MeV)	30 full-power effective years neutron fluence n/m^2 (E > 0.5 MeV)
welding seam SN0.1.4	$1.7 \cdot 10^{15}$	$1.6 \cdot 10^{24}$
maximum forged ring 0.3.1	$2.5 \cdot 10^{15}$	$2.4 \cdot 10^{24}$

The Russian code [PNAEG-1986] provides material data and toughness trend curves for the WWER RPV materials. The trend curves are indexed with a so called "critical embrittlement temperature", which is based on Charpy-V ductile-to-brittle transition temperatures, DBTT. As mentioned above, the WWER-440 RPVs of the first generation were not provided with surveillance specimens. Another issue is the limited information about the initial critical embrittlement temperature, T_{K0}, of the RPV materials [Brumovsky-2005, -2018a], which was estimated by its correlation with the chemical composition in case of the Greifswald RPVs [Böhmer-1999]. The critical embrittlement temperature for the irradiated condition, T_K, is estimated by PNAEG-1986 as follows [Brumovsky-2005, -2018a]:

$$T_K = T_{K0} + \Delta T_F + \Delta T_T + \Delta T_N \quad (1)$$

ΔT_F: shift of the critical embrittlement temperature due to irradiation,

ΔT_T: shift of the critical embrittlement temperature due to thermal aging, and

ΔT_N: shift of the critical embrittlement temperature due to cyclic damage.

The most relevant DBTT shift is caused by neutron irradiation. This is determined for the RPVs of the second WWER-440 generation by testing of surveillance specimens or estimated by the prediction formula according to PNAE G-7-008-86 [PNAEG-1986, IAEA- 1997, Brumovsky-2018a]:

$$\Delta T_K = A_F^T \cdot \sqrt[3]{\frac{F_n}{F_0}} \qquad (2)$$

A_F^T: irradiation embrittlement factor for irradiation at temperature T, °C,
= 800·(P + 0.07 Cu) for WWER-440 10KhMFT welds (T_{irr} = 270°C, Cu and P in wt. %)
= 18 for WWER-440 15 Kh2MFA base metal (T_{irr} = 270°C)

F_n: neutron fluence, E > 0.5 MeV, n/m^2,

F_0: 10^{22}, n/m^2.

The lower bound fracture toughness, K_{IC}, curve Eq. (3) used for the WWER RPV integrity assessment is indexed with T_K [PNAEG-1986, IAEA- 1997, Brumovsky-2018a].

$$K_{IC} = 26 + 36 \cdot e^{[0.2\cdot(T-T_K)]};\ K_{IC} \le 200 MPa\sqrt{m} \qquad (3)$$

For WWER reactors the "Unified Procedure for Lifetime Assessment of Components and Piping in WWER NPPs - VERLIFE" [VERLIFE-2015, Brumovsky-2018a] defines a MC-based reference temperature, RT_0, used in integrity assessment of WWER reactors as:

$$RT_0 = T_0 + \sigma + \delta T_{type} \qquad (4)$$

T_0 reference temperature according to ASTM E1921

σ margin $\sigma = \sqrt{\sigma_1^2 + \delta T_M^2}$

σ_1 $= 1.64 \cdot \frac{\beta}{\sqrt{N}}$

β = 18 K according to ASTM E1921

N number of tested specimens

δT_M considers a possible uncertainty of the material: = 16 K

δT_{type} considers the bias of the specimen type:
= 15 K if pre-cracked Charpy size specimens are tested
= 0 K if pre-cracked C(T) specimens are tested

The VERLIFE procedure suggests the following RT_0 indexed lower bound curve for WWER base and weld metal:

$$K_{Jc}^{5\%}(T) = \min\left\{25.2 + 36.6 \cdot e^{[0.019\cdot(T-RT_0)]};\ 200\right\} \quad in\ MPa\sqrt{m} \qquad (5)$$

Eq. (5) agrees with the standard MC for 5% fracture probability in ASTM E1921.

Austenitic overlay cladding has been originally designed to protect the low alloyed RPV base and weld metals against corrosion. Usually, the overlay cladding remains out of consideration in the current RPV integrity assessment regulatory codes [Brumovsky-1997, Gillemot-2007]. Some codes allow the inclusion of the overlay cladding on condition that its properties are known during the RPV lifetime [Brumovsky-2003, -2018b, Gillemot-2007]. The fracture behaviour of an operating nuclear RPV, particularly during certain overcooling transients, may strongly depend on the properties of the irradiated overlay cladding [Haggag-1990]. Investigations have shown that the integrity of the overlay cladding strongly influences the

loading of a crack in the base or weld metal during an emergency pressurized thermal shock, PTS, event. An intact overlay cladding clamps an under clad crack and results in a lower stress intensity factor K_I at the crack tip. In contrast a surface crack is additionally loaded due to the tension stress in the overlay cladding caused by different thermal properties with respect to the base or weld metal [Abendroth-2007]. Therefore, knowledge about the properties of the overlay cladding, mainly of its fracture toughness, is also necessary for a precise evaluation of the RPV integrity during a PTS event. Overlay cladding material is currently not included in the RPV surveillance specimen programmes. Therefore, mechanical and fracture toughness data are not available from operated RPVs.

Trepanning Technology

The trepans were taken with a specially designed trepanning device (Fig. 1) which enables the following actions:

- labelling of the position and orientation of the trepan to be sampled,
- milling of the trepan out of the RPV and then pushing into the RPV, and
- closing of the resulted hole in the RPV by a lead plug.

The cutting tool consisted of 4 hard metal blades with a width of 2.5 mm each (Fig. 1b). The design of the trepanning machine and the sampling at place was a contract work performed by the company Studsvik GmbH & Co. KG, Niederlassung Blankenloch.

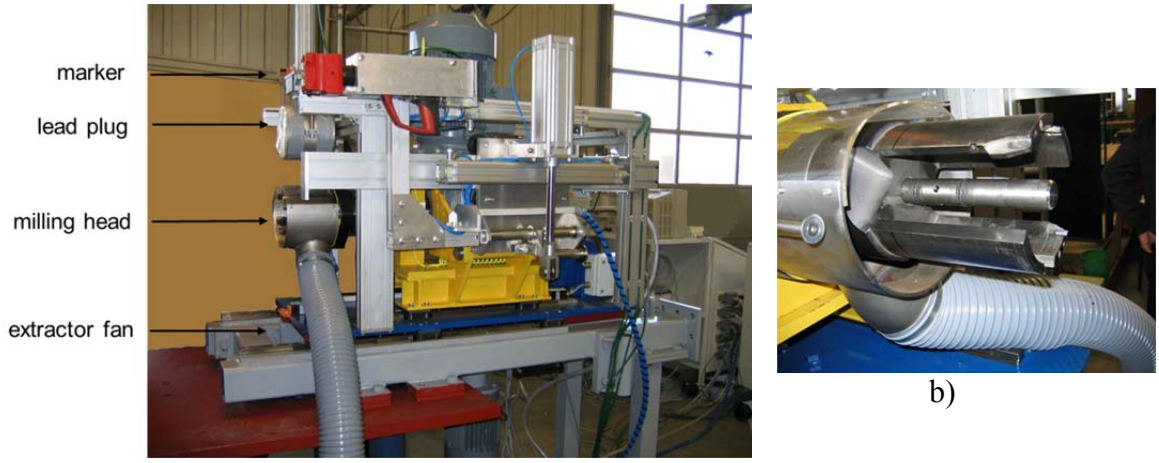

a) b)

Fig. 1: Trepanning device a) and cutting tool with ejector b) of the milling head.

Trepans were extracted from different azimuthal locations of the circumferential beltline welding seam SN0.1.4. and the forged base metal ring 0.3.1 of Greifswald RPVs. The trepanning device was mounted outside the RPV at the height of the coolant loops on the top of the water tank (Fig. 2b). The water tank had a shielding function and additionally formed the foundation of the RPV. As the nozzles of the RPV had been cut off during the decommissioning, the RPV could be lifted and rotated by crane towards the predefined positions of the trepans (Fig. 2). After the RPV reached the desired position, it was fixed by three extendable supports in his vertical position. Before the actual drilling event, the selected position was marked by a vertical line (to identify/reassign the orientation afterwards) and numbered (to distinguish the trepans from each other). The trepan was drilled using an air-cooled hollow milling tool (Fig. 1b) featuring an extractor fan for the removal of millings. Then, the trepan was pushed into the RPV. Finally, the resulted hole in the RPV wall was

sealed by a lead plug. All of the aforementioned actions were remote-controlled. The diameter of the trepan (Fig. 3) is 119 mm over the whole RPV wall thickness. By thermographic measurement it was proven that the maximum temperature never exceeded 190°C in vicinity of the drilling region and 80°C within the trepan itself.
Regarding the azimuthal distribution of the neutron flux, the reactor core of the Greifswald RPVs can be divided in 60° sectors. The trepans originate from the azimuthal locations with the highest neutron flux.

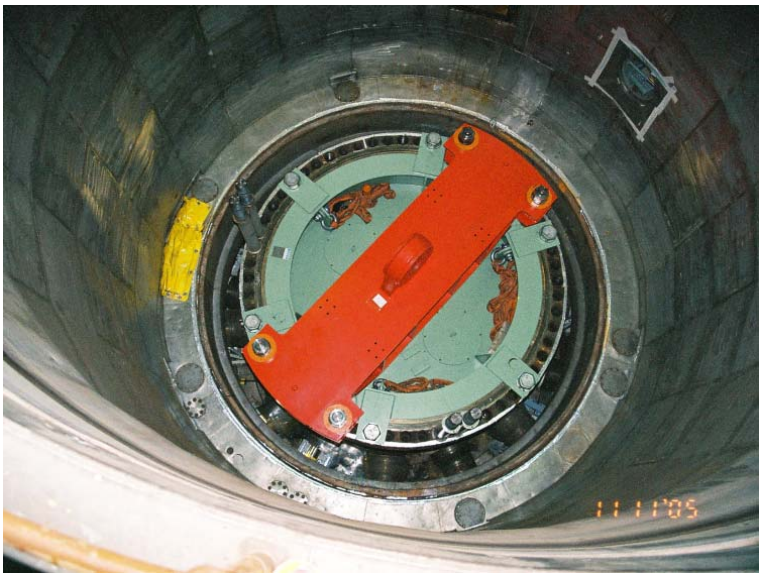

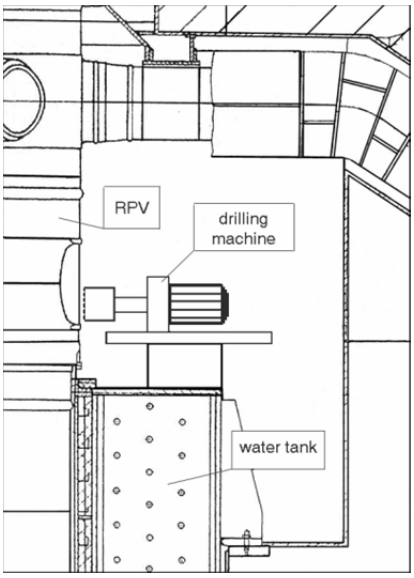

a) b)

Fig. 2 RPV of Greifswald Unit 1: a) top view with biological cover and lifting beam; b) location of the trepanning device on the water tank.

Fig. 3: Trepan sampled from the Greifswald Unit 1 RPV.

Table 3 gives an overview about the trepans sampled from the RPVs of the Greifswald WWER-440/V230 units. Trepans from the beltline welding seam SN0.1.4. of the Units 1, 2 and 4 RPVs were provided to VTT Espoo and specimens machined from these materials were additionally irradiated in the RPVs of the Finish Loviisa WWER-440 Units. This material was used to verify the large scale annealing of the WWER-440 Lovisa Unit 1 and the live time extension of both Loviisa Units. The irradiation experiments and the investigations are in progress.

Table 3: Summary of trepans sampled from the RPVs of the Greifswald WWER-440/V230 units.

Unit	RPV-material	condition	temperature during recovery annealing	trepan
1	welding seam SN0.1.4.	IAI	475°C	1-1
				1-2
				1-5
1	forged base metal ring 0.3.1.	IAI	475°C	1-4
		U	<300°C	1-3
2	welding seam SN0.1.4.	IA	475°C	2-1
				2-2
				2-3
	welding seam SN0.1.3	U	< 300°C	2-4
	forged base metal ring 0.3.1.	IA	475°C	2-5
				2-6
4	welding seam SN0.1.4.	I	-	4-3
				4-4
				4-5
				4-6
4	forged base metal ring 0.3.1.	I	-	4-1
				4-2
total number of the sampled trepans				17

	provided to FORTUM (Finland)		already investigated

Irradiation Loading

Monte Carlo Program TRAMO

The neutron flux through the RPV was calculated with the code TRAMO, [Bartz-1998a, 1998b], which is a multi-group Monte Carlo code for neutron and gamma transport calculations. The code is an in-house development especially for reactor dosimetry purposes and shielding problems. It has been tested and validated in many relevant benchmarks. The geometrical options were optimized for fission reactor geometry. The basic geometry is a system of non-intersecting bodies arbitrarily nested among each other and all having parallel axes. Theses bodies can have independent and arbitrary subdivisions in vertical direction. To speed up the calculations, special routines for typical reactor geometries were implemented (for example hexagons). The most essential support to obtain results with low statistical error is a reasonable set of zone weights. For the calculation of optimal weights the code TRAWEI was developed (Monte-Carlo Code with the help of recursive procedures) [Barz-1998b].
The program has its own data supply. On the basis of microscopic group cross sections generated by NJOY [MacFarlane-1994a], the own code MODAJ [Barz-1998b] provides macroscopic cross sections using the Bondarenko method [Bondarenko- 1964] by considering different dilutions and temperatures. Equiprobable angular intervals for different energy points are used for the treatment of elastic scattering and scattering in the thermal region. The Polynominal Legrendre (PL)-approximation is applied for all non-elastic scatterings and gamma scattering. The numbers of groups is variable.

Input Data and Calculation Option

Full geometrical information was used for the investigated units. The 30° symmetry is typical for WWER cores. As the neighbouring 30˚ sectors show slightly asymmetrical source distributions, a 60˚ sector had to be used for the calculation model. Fig. 4 shows the horizontal sectional drawing of the model used in the calculation at the height of the reactor core with dummy assemblies. Dummy assemblies (with structure) were inserted in the outer assembly rows in the last 4 cycles of unit 1. A separate model was used for these cycles. The red assemblies have sources in the calculations because only these practically contribute to the neutron fluence in the RPV. The yellow assemblies serve as reflector. The inner assemblies (black) have no significance for the result, because the neutrons are set as complete absorbed. Fig. 5 shows an axial cross section indicating the position of the core and the height of the positions of the sampled trepans in the RPVs. The depicted internal and the peripheral details were considered in the fluence calculations. Neutron fluence calculations were performed for the position summarized in Table 3. The selected geometrical model includes all important features of the system.
The compositions of the different materials were taken from [Suschowk-2002]. Uranic dioxide (enrichment 3.6%) was generally used as fuel without considering the burnup. The different water densities in the reactor core were taken into account. Resonance self-shielding was considered complying with the Bondarenko model in form of the F-factors formalism [Bondarenko-1964]. The complete data file for the Monte Carlo calculations contains 31 different compositions based on 48 different nuclides.

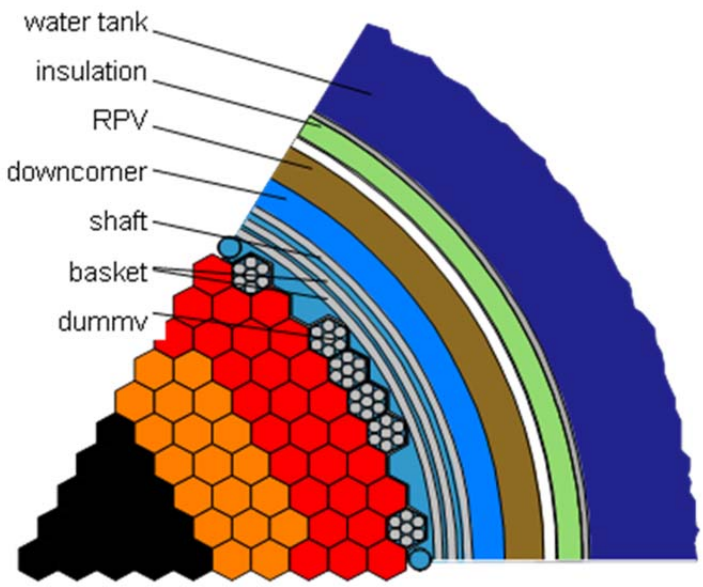

Fig. 4: Horizontal drawing in the core region of the calculation model of TRAMO with dummy, sources (red), refection (yellow) and black assemblies.

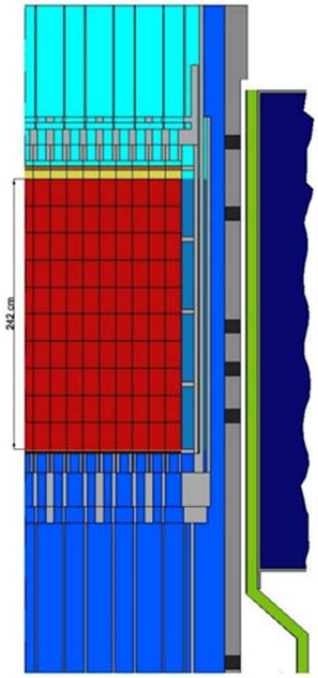

Fig. 5: Axial calculation Model and trepan positions (dark-gray-squares).

The necessary neutron source data were calculated based on the power data of all cycles of the units [Suschowk-2002]. These were available for all assemblies, 10 height layers and for time steps of about 20 effective days. In addition, the pin-wise burnup and power distribution was given [Suschowk-2002] for the three outer fuel assembly rows. The gamma sources were assumed to be proportional to those of the neutrons. The proportionality factor was determined on the basis of U-235 fission. By default, neutrons were originated in the outer three rows of fuel assemblies pin by pin. An equal distribution would here lead to a considerable error. In contrast, for the transport calculations, the assembly structure can be homogenized. For few calculations, the number and the position of the used source zones were optimized corresponding to its influence on the corresponding result. Generally a source biasing was applied. The energy distribution of neutron and gamma sources corresponds to the fission spectra of U-235, taking into account 415 neutron and 19 gamma energy groups a quota sampling was used for the source. The coupled neutron and gamma calculations were started only with neutrons. The fission reaction was treated as a capture reaction without gamma production. The photons were produced only by neutron reactions from inelastic scattering and capture reactions. Separate calculations were carried out for the photons from fission.

The ENDF/B-VI [MacFarlane-1994] and newest ENDF/B-VII [Chadwick-2006] nuclear data libraries were used for the group section calculations. The SAND II [MacFarlane-1994] structure with 640 groups for neutrons and the CSEWG [MacFarlane-1994] structure with 94 groups for gammas were the standard group structure. Scattering matrices, calculated with the help of the free gas model or with the momentum and energy transfer factors α, β [MacFarlane-1994], were used for the thermal scattering. Different variance reducing techniques were used. Besides a source biasing, the "Weight Window" method is primarily used. Moreover, the upper energy groups were separately calculated, with the effect of a

strong reduction of the statistical errors in these groups. Integral and spectral fluences of neutrons and gammas via the RPV were determined in steps of 1 cm for each trepan. A distribution on these surfaces can be calculated by their fragmentation. The activities were determined based on the calculated fluence spectra. The reaction cross sections and the half-life were compared with the experiment.

Comparison of Neutron Fluences

The influence of the data library, of the number of energy groups and of the thermal scattering matrix on the neutron fluence was studied. Calculations, C, with B6 and B7 data in two energy groups (47 and 640) were carried out. Besides, two above named scattering models were used. The reference values, C_R, were calculated with B7 data, 640 energy groups and using α/β factors for the thermal matrix. The comparison between the different thermal scattering matrices has shown that their influence can be neglected. Table 4 shows therefore only the C/C_R ratio between the results obtained using different group numbers and libraries, for fluences evaluated on the inner wall surface (inside), 7 cm from the inner wall surface (middle) and on the outer wall surface of the RPV.

Table 4: C/C_R ratio of calculations in different points of RPV.

Comparison	energy	inside	middle	outside
B7 47 / B7 640	fast	1.03	0.98	0.95
	thermal	0.91	0.80	0.61
	total	0.97	1.00	0.96
B6 47 / B7 47	fast	0.81	0.84	0.83
	thermal	0.83	0.70	0.59
	total	0.83	0.84	0.86

Larger differences were found in the results between the 47 and 640 group calculations especially in the thermal energy region. The values calculated with 640 groups are considerably higher. This effect is caused by the improved conversion of the cross section resonances. In most calculations, a rough energy group structure (here 47 groups) results in an overestimation of the cross sections. The effect can be minimized by the use of fine energy groups. A correct calculation of the thermal fluence is important for the determination of the activities. The large difference between the B6 and B7 calculations was surprising. Bigger values - on average 15 % - were calculated with the new data. The reason is seen in the new iron data. Calculations based on the JENDL3.3 [Shibata-2002] nuclear data library were also carried out. The results were practically identical to the reference values. This shows that the differences are reduced in the libraries.

Comparison Calculation and Experiment

The "Verein für Kernverfahrenstechnik und Analytik", VKTA, in Dresden has carried out the experimental determination of the activities. The activities of nuclides ^{93m}Nb, ^{99}Tc, and ^{63}Ni were determined. The preferred measuring method of the activities was liquid scintillation counting (LSC) and of the quantity was inductively coupled plasma mass spectrometry (ICP-MS). The radiochemical separation is based on anion exchange chromatography. The statistical uncertainty of the LSC measurements was very low (<3 %) and for the ICP-MS is approximately at the level of 5 %.

The radiochemical separation of niobium is described in detail in [Baers-1992]. Standard techniques were used for the chemical processing of nickel and technetium. The measured activities of nickel are due to superposition of ^{59}Ni and ^{63}Ni activities. Separation of the results is not possible with LSC measurement, but the activity is 99% ^{63}Ni due to the long half life time of ^{59}Ni.

Samples were taken at different depth of the RPV and the activities from ^{93m}Nb, ^{63}Ni and ^{99}Tc in them were determined. Table 5 and Table 6 show the comparisons. ^{93m}Nb was measured in seven samples, while ^{63}Ni and ^{99}Tc in two samples. For the comparison of ^{93m}Nb it is important to know that the activities were generated from ^{93}Nb and ^{92}Mo. Table 5 shows the calculated activities (generated by both paths), the measured activities and the C/E (C: calculation, E: experiment) values. The C/E ratios are very different. One reason could be the very small concentration of niobium and then error associated in the measurement.

Table 6 shows the C/E ratios of the ^{63}Ni and ^{99}Tc. For all samples, the calculated activities are smaller than the measured. One reason could be small errors in density. The used activities are generated by thermal scattering and the material densities have a big influence on thermal fluences and consequently on the calculated values. Despite the many different influences on the results, good agreement was achieved between the calculated and measured activities selectively. The results show that, for the single activity, the calculated results can be validated by analysing the nuclides contained in the RPV material.

Table 5: Measured and calculated activities of ^{93m}Nb and their C/E ratios in the weld (SN0.1.4.) and base (0.3.1.) metals of the Unit 1 RPV.

Distance*	activities Bq/g		C/E
	Experiment	Calculation	
0.0	479	261	0.54
1.0	998	196	0.20
2.0	288	139	0.48
4.5	104	105	1.01
7.0	79	80	1.01
9.0	121	71	0.59
11.0	38	43	1.13

* distance from inner RPV wall in cm

Table 6: Measured and calculated activities of ^{63}Ni and of ^{99}Tc and their C/E ratios in the weld (SN0.1.4.) and base (0.3.1.) metals of the Unit 1 RPV.

nuclide	Distance*	activities Bq/g		C/E
		Experiment	Calculation	
^{63}Ni	4.5	11200	9074	0.81
	7.0	5200	4022	0.77
^{99}Tc	4.5	28.9	26.3	0.91
	7.0	21.2	19.3	0.91

* distance from inner RPV wall in cm

Results of the Neutron Fluence Calculations

The operation data of the Greifswald Units are summarised in Table 1. Table A 1 and Table A 2 contain the data of the neutron loading of the discs machined though the thickness of the welding seam SN0.1.4. (trepan 1-1) and the forged base metal ring 0.3.1. (trepan 1-4),

respectively, of the Greifswald Unit 1 RPV. Unit 1 was operated for the first 11 campaigns without shielding assemblies and for the last 4 campaigns with shielding assemblies. Unit 1 was large scale thermally annealed after 13 campaigns and operated for two campaigns thereafter (Table 1). Table A 3 contains the neutron loading of the discs machined though the thickness of the welding seam SN0.1.4. (trepan 2-3) of the Greifswald Unit 2 RPV. Unit 2 was not put in operation after large scale annealing (Table 1). The Table A 4 and Table A 5 contains the neutron loading of the discs machined through the thickness of the Unit 4 forged base metal ring 0.3.1. (trepans 4-1 and 4-2). These trepans were sampled in the position of the maximum flux of the Greifswald Unit 4 RPV. The neutron fluences of discs of the trepans 4-4 and 4-6 sampled from the beltline welding seam SN0.1.4 of the unit 4 RPV are summarized in Table A 6 and Table A 7, respectively. Unit 4 was shut down after 11 campaigns operation (Table 1).

Materials and Specimens

The wall thickness is 140 mm and 150 mm for uncladded and cladded RPVs, respectively. Fig. 6 shows the trepan and exemplifies the cutting schemes from the forged base metal ring, 0.3.1 and the multilayer welding seam SN0.4.1.. As the first work step, a vertical cut was made to transfer the former orientation of the trepan in the RPV to the discs to be cut. In the following step the curvature at the inner side of the trepan was cut to get a plane reference surface followed by the cutting of the discs of 3 mm and 10 mm thickness. From the 3 mm and 10 mm discs, rectangular tensile and Charpy size SE(B) specimens were machined, respectively. The first disc towards the inner RPV wall of Unit 4 contains the overlay cladding.

The orientation of the specimens according to ASTM E1823 is as follows (Fig. 6):

- Charpy V-notched and Charpy size SE(B) specimens:
  - welding seam SN0.1.4.: T-S (specimen axis along vessel axial direction and crack growth direction across the vessel wall), and
  - forged base metal ring 0.3.1.: L-S (specimen axis circumferential and crack growth direction across the vessel wall).
- rectangular (gauge section: 3 mm · 4 mm) and miniature (gauge section: 1 mm · 2 mm) tensile specimens:
  - welding seam SN0.1.4.: T (specimen axis along the vessel axial direction), and
  - forged base metal ring 0.3.1.: L (specimen axis circumferential).

The orientation of the specimens is in accordance with the orientation of the surveillance specimens of the Russian WWER-440 second generation RPVs.

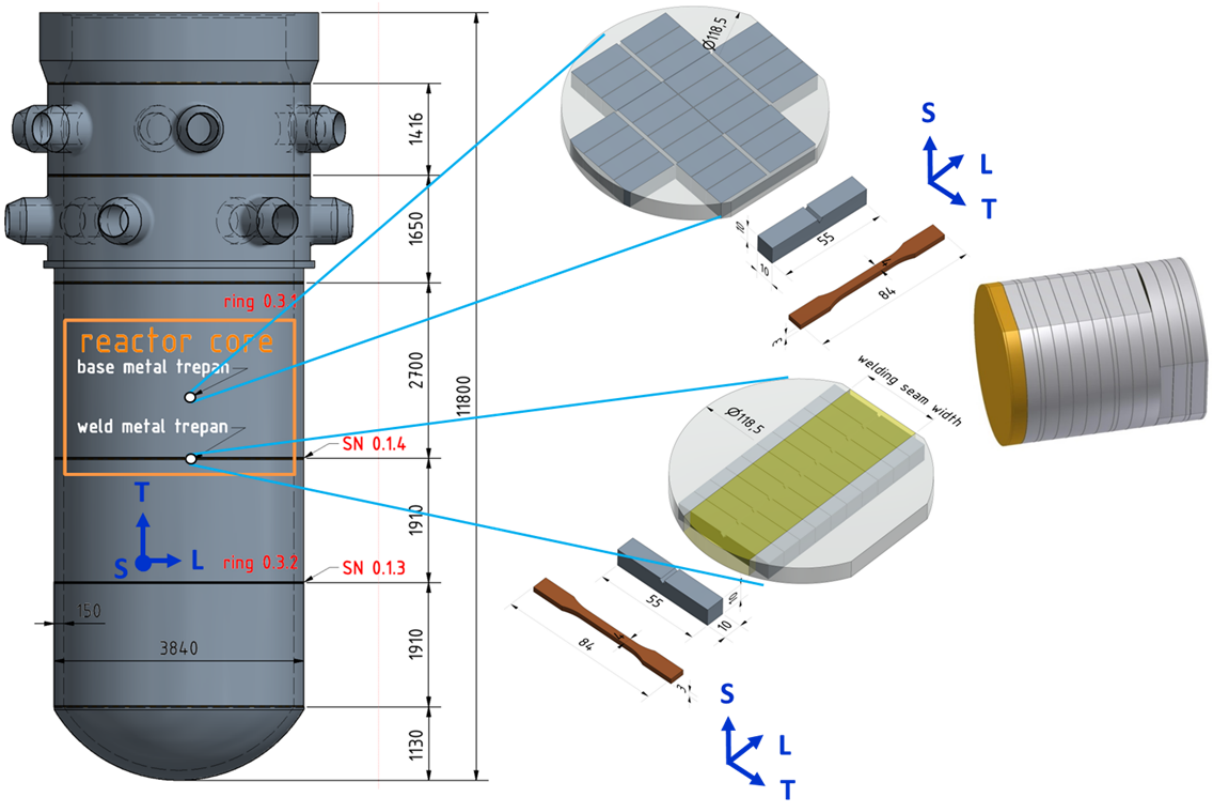

Fig. 6: Location and exemplary cutting scheme of the trepan from the forged base metal ring 0.3.1. and the multilayer welding seam SN0.1.4.

SE(B) specimens were also machined from the first disc towards the inner RPV wall containing the overlay cladding (Fig. 6). From this disc 14, Charpy size SE(B) specimens in L-S orientation (specimen axis along vessel circumferential direction and crack growth direction in the vessel radial direction) according to ASTM E1823 were machined as shown in Fig. 6. In addition, sub-sized rectangular flat tensile specimens were machined from broken halves of the tested Charpy size SE(B) specimens as schematically depicted in Fig. 7. From one half, 2 specimens from the first layer and 4 specimens from the second layer of the overlay cladding were machined. The orientation of the tensile specimens was L (specimen axis along vessel circumferential direction) according to ASTM E1823.

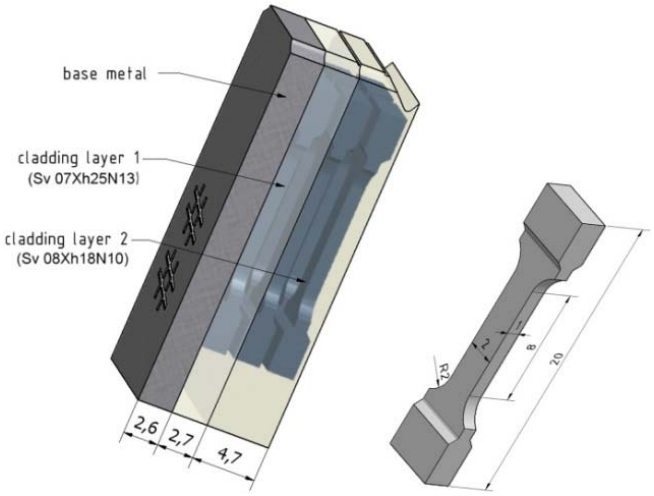

Fig. 7: Scheme of the machining of sub-size tensile specimens from broken halves of Charpy size SE(B) specimens.

Table 7 summarizes the material conditions of the trepans sampled from the Greifswald RPVs and the neutron fluences calculated at the inner and outer RPV wall. The neutron fluence decreases through the RPV wall by approximately 80%.

Table 7: Condition, accumulated neutron fluence and estimated ductile-to-brittle transition temperature of the RPV weld and base metals sampled from des Greifswald Units.

unit	RPV-material	condition	$\Phi_{E>0.5MeV}$ in 10^{18} n/cm^2		T_{K0}**	T_k**	TT_{41J}***
			inner wall*	outer wall*	°C	°C	°C
1	15Kh2MFA, 0.3.1.	irradiated + 475°C/152h + irradiated	53.11	14.04	0	<70	-
			1.61	0.49	-	-	-
	10 KhMFT, SN0.1.4		40.48	9.05	46	186	30
			1.17	0.33	-	-	-
2	15Kh2MFA, 0.3.1.	irradiated + 475°C/152h	64.27	16.32	0	<70	
	10 KhMFT, SN0.1.4.		47.38	11.59	4	146	19
4	15Kh2MFA, 0.3.1.	irradiated	53.84	12.67	0	<70	
	10 KhMFT, SN0.1.4.		40.92	9.20	-13	127	

* calculated for the axial position of the trepans [Rindelhard-2009, Viehrig-2011]
** condition (before large scale annealing) taken from the documentation [Boehmer-1999]
*** condition after large scale annealing measured with KLST-specimens sampled from the RPV inner wall [Ahlstrand-1993]

Beltline Welding Seam SN0.1.4

The location of the multilayer welding seam within trepans was metallographically examined. As shown in Fig. 8, the WWER-440 X-butt multilayer submerged arc welding seam consists of a welding root welded with an unalloyed wire Sv-08A and the filler material welded with the alloyed wire Sv-10KhMFT and flux AN-42. The welding seams of cladded RPVs have additional cover layers welded with the unalloyed wire Sv-08A [Boehmer-1999].

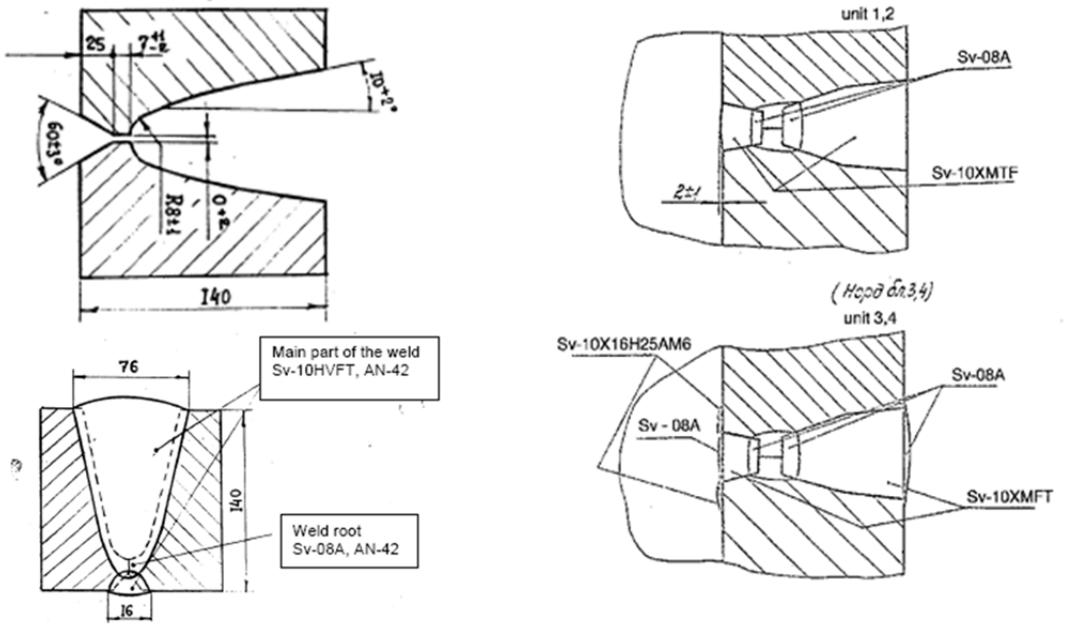

Fig. 8: Shape and welding sequence of the beltline multilayer welding seams SN0.1.4. of the Greifswald WWER-440/V213 RPVs [Boehmer-1999].

The metallographic sections and the distribution of deleterious elements Cu, P and main alloying elements through the thickness of the investigated beltline welding seams from Greifswald Units are depicted in Fig. 9 to Fig. 11.

The shape of Unit 1 welding seam (Fig. 9) differs from the WWER-440 first generation standard welding seams as shown in Fig. 8. It is assumed that the original welding seam was replaced by a second one, which was not welded according to the standard welding technology.

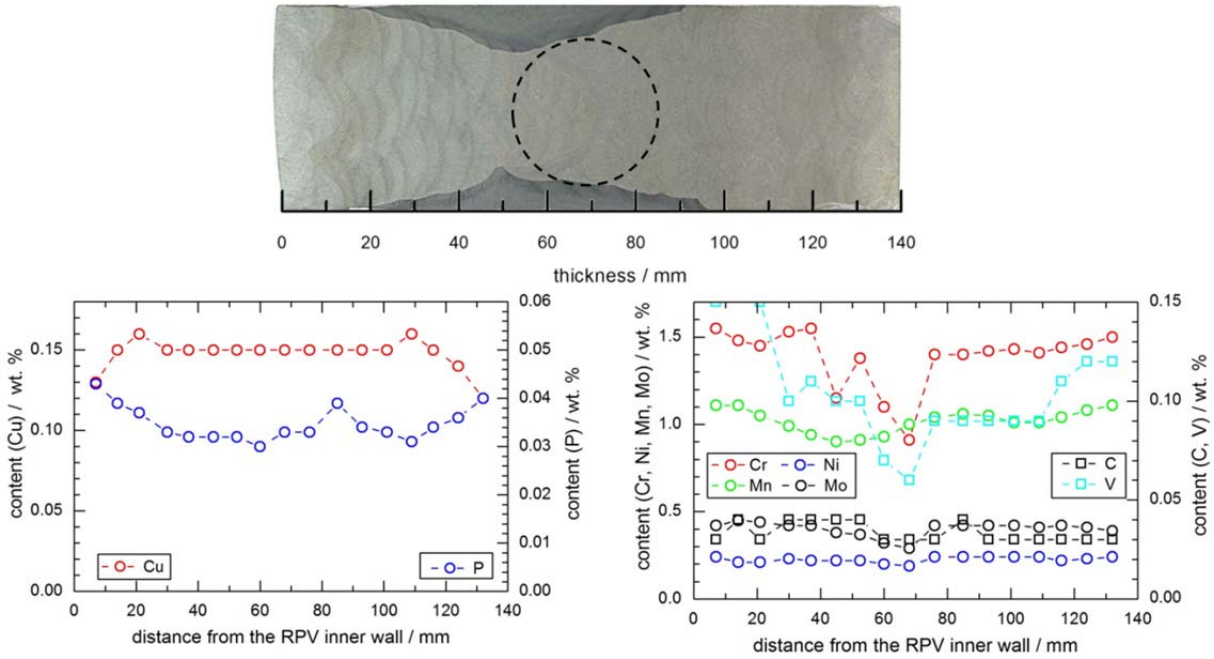

Fig. 9: Metallographic section and chemical composition of the multilayer welding seam from the uncladded Unit 1 RPV [Valo-2011].

The standard welding technology as described above resulted in a welding root region containing a mixture of the welding wires (Sv-10KhMFT and flux AN-42) and the base metal from the adjacent forged rings. This was reflected in chemical composition within the welding root region which showed a sink on the Cu and P content and an increase of the C, Cr and V content as visible in Fig. 10 and Fig. 11 for the Units 2 and 4, respectively. A distinct welding root with the sink in Cu and P is not visible in Fig. 9. There is also no increase in the C content, but a decrease of the Cr and V content in the region where the beads welded from the inner and outer wall join together.

The mean chemical compositions measured by optical emission of the filling layers are summarized in Table 8. The chemical composition the Cu and P contents were within the range as specified in the manufacturing guidelines of the first-generation WWER-440/V-230, but both were higher than in the specification of the next generation units (WWER-440/V-213) with maximum allowed P and Cu contents of 0.01% and 0.1%, respectively [Brumovsky-2005].

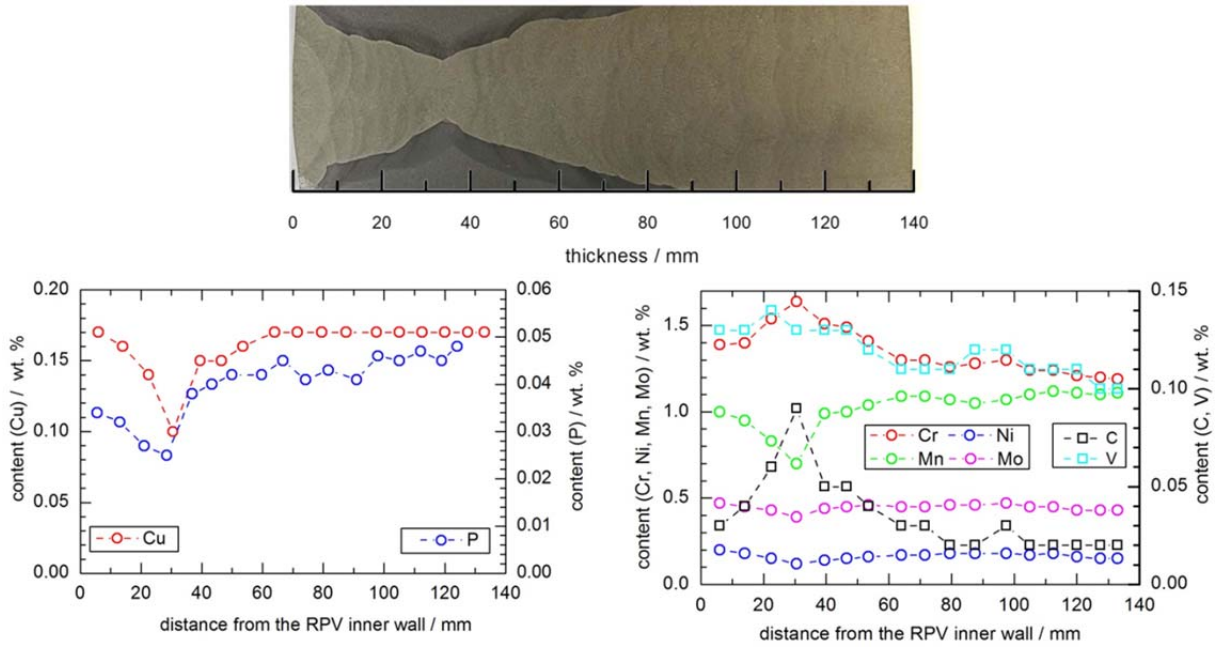

Fig. 10: Metallographic section and chemical composition of the multilayer welding seam from the uncladded Unit 2 RPV [Valo-2011].

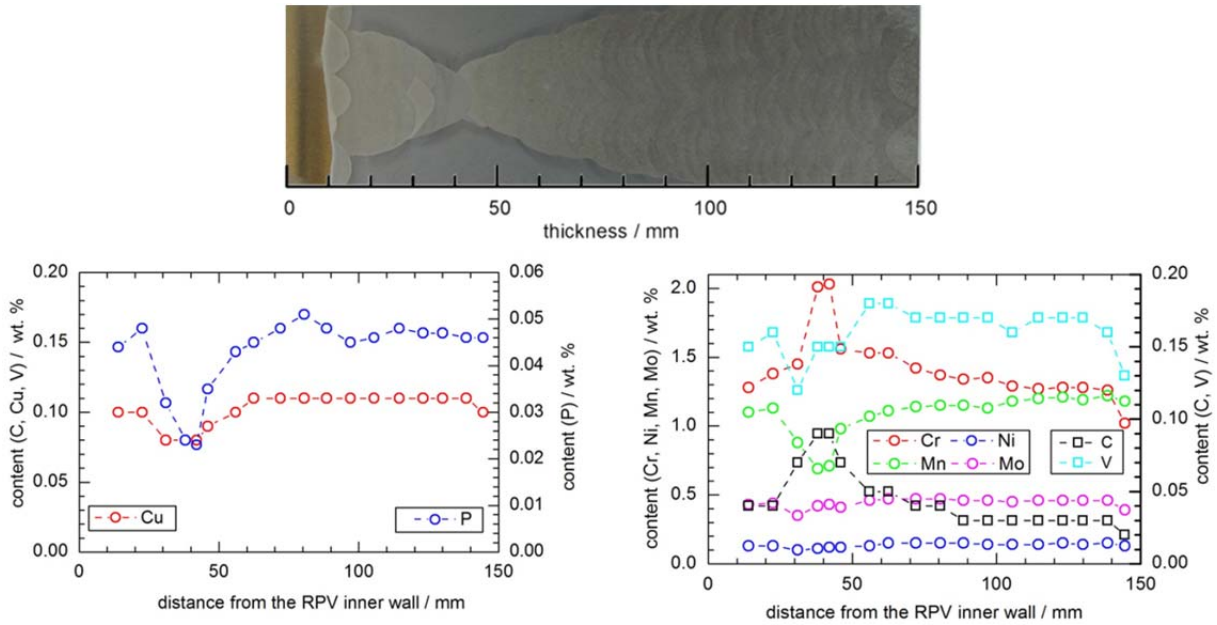

Fig. 11: Metallographic section and chemical composition of the multilayer welding seam from the cladded Unit 4 RPV [Valo-2011].

Table 8: Mean chemical composition of the filling passes beyond the welding root region of the beltline welding seam SN0.1.4. in wt. % [Valo-2011].

Unit	RPV material	C	Si	Mn	Cr	Ni	Mo	V	P	Cu
1	10KhMFT	0.03	0.35	1.03	1.42	0.24	0.42	0.09	0.034	0.15
2		0.03	0.42	1.08	1.28	0.17	0.45	0.11	0.044	0.17
4		0.04	0.47	1.16	1.36	0.14	0.46	0.17	0.047	0.11

An important fact is that the fatigue crack front in a T-S oriented SE(B) specimen from the multilayer welding seam is virtually located in an uniform microstructure of one welding bead. In contrast the crack front of T-L specimens includes several welding beads with a non-uniform microstructure [Viehrig-2009b].

Forged Base Metal Ring 0.3.1.

The chemical composition measured by optical emission and the main heat treatment of the investigated forgings are summarized in Table 9. The copper and phosphorus contents are within the range as specified in the manufacturing guidelines of the WWER-440/V-230 first generation, however, both are higher than what was specified for the next generation units (WWER-440/V-213) with maximum allowed P and Cu contents of 0.012% and 0.08%, respectively [Brumovsky-2005].

Table 9: Mean chemical composition within ¼ and ¾ thickness in wt. % [Valo-2011] and heat treatment [Boehmer-1999] of the forged ring 0.3.1..

Unit	RPV material	C	Si	Mn	Cr	Ni	Mo	V	P	Cu
1	15Kh2MFA	0.13	0.29	0.40	2.91	0.18	0.58	0.26	0.012	0.16
2		0.14	0.23	0.40	2.84	0.15	0.63	0.21	0.015	0.11
4		0.11	0.27	0.40	2.93	0.15	0.60	0.20	0.014	0.09
heat treatment forged ring 0.3.1.: austenitising: 1000°C/9h; quenching: oil; tempering: 690°C/18h										
heat treatment RPV after welding: tempering: 660 - 680°C/15h										

Overlay Cladding

The RPV of Greifswald Unit 4 is overlay cladded by austenitic stainless materials using automatic submerged welding methods. The cladding was welded in two layers overlay with three welding passes (Alekseenkov-1997, Timofeev-2006):

- first layer (one pass) with a thickness of 3 to 4 mm: ribbon of Sv-07Cr25Ni13 and OF-10 flux, and
- second layer (two passes) with a thickness of 6 to 9 mm: ribbon of Sv-08Cr19Ni10Mn2Nb and OF-10 flux.

Consequently, the total thickness of the cladding amounts to 8-10 mm after mechanical machining.

Table 10: Chemical composition of the cladding materials (wt. %)

material	C	Cr	Ni	Mn	Cu	P	Nb
Sv-07Cr25Ni13*	<0.09	23.0-26.5	11.0-14.0	0.8-2.0	-	<0.03	
Sv-08Cr19Ni10Mn2Nb**	<0.10	17.5-20.5	8.5-11.0	1.3-2.5	-	<0.03	
Sv-08Cr19Ni10Mn2Nb (base metal trepan 4-1)***	-	18.7	10.20	1.42	0.24	0.031	0.65
Sv-08Cr19Ni10Mn2Nb (weld metal trepan 4-6)***	-	18.3	9.85	1.37	0.23	0.026	0.62

* 1st layer according to the specification (Brumovsky-1997, Timofeev-2006)

**2nd layer according to the specification (Brumovsky-1997, Timofeev-2006)

*** chemical analysis of the material from the 2nd layer

The welding of the cladding and the assembling of the forged rings that form the RPV were performed simultaneously, with the aim to reduce the number of heat treatments. Within these technological processes, the cladding in the core region of the RPV, which includes the forged base metal ring 0.3.1. and the welding seam SN0.1.4., was tempered five times in the temperature range 660-675 °C with a total duration of 50 h (Timofeev-2006). The overlay cladding contains up to 8% δ-ferrite to avoid hot cracks. The chemical composition of the overlay cladding is summarized in Table 10.

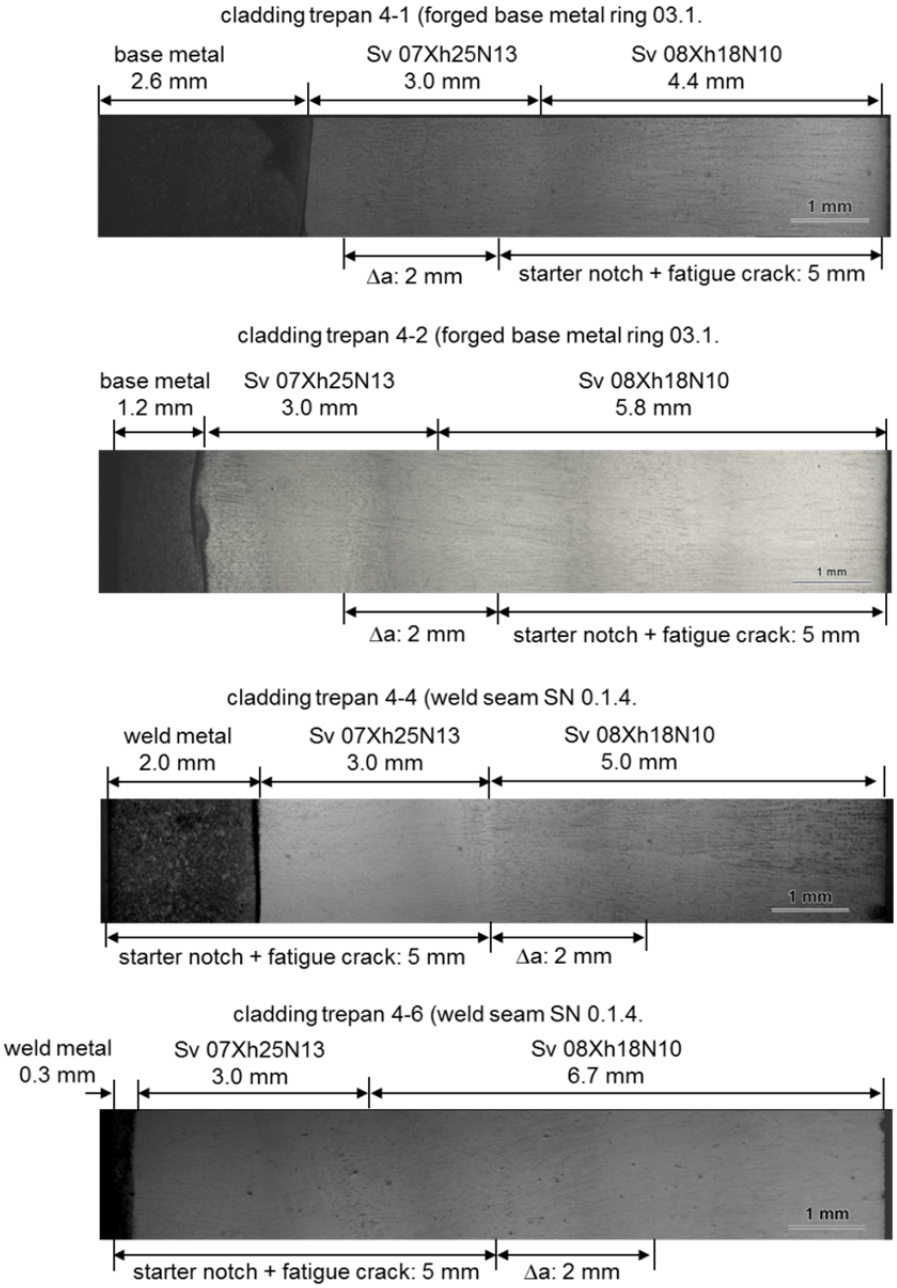

Fig. 12: Overview of the microstructure of the investigated overlay cladding from the individual trepans and the location of the crack tip.

As mentioned before, a disc with a thickness between 1.5 and 4 mm was cut from the inner side of the trepan. Therefore the crack tips in the SE(B) specimen were at different locations in the cladding for the individual trepans. Fig. 12 gives an overview about the crack tip locations in the microstructure of the investigated overlay claddings. In the base metal, trepans 4-1 and 4-2 the crack tips were located in the 1st and the 2nd layer of the cladding,

respectively. During the testing of the specimens, the cracks propagated by about 2 mm towards the base metal within the 1st and 2nd layer in the cladding from the trepans 4-1 and 4-2, respectively (Fig. 12). In the weld metal trepans 4-4 and 4-6, the crack tips were located in the 2nd layer and the cracks moved within this layer towards the RPV inner wall surface during the fracture mechanics testing. The reason for this change of the crack propagation direction was to maintain the crack propagation in the same material during the testing. Otherwise the crack would move from the first to the second layer. Generally, it has to be taken into account that the locations of the crack tips varied within one disc because of the curvature of the RPV and differences of the fatigue crack length. The difference can amount up to 0.25 mm.

Testing and Evaluation

The irradiated specimens were tested remote controlled with a servohydraulic testing system installed in a hot cell laboratory. Tensile and ductile fracture toughness tests were performed on tensile and SE(B) specimens, respectively from different thickness locations according to DIN EN ISO 6892-1 and ASTM E1820. For the testing according to ASTM E1921 and ISO 148-1, SE(B) and Charpy V-notched specimens, respectively machined from one disc (thickness location) constituted a set of specimens, for which T_0 and TT_{47J} values were defined. In addition, the microstructure of the forged base metals and multilayer welding seams were characterised by metallographic micrographs and hardness measurements.

Tensile Testing According to DIN EN ISO 6892-1

Tensile testing was conducted with the rectangular and miniature tensile specimens as shown in Fig. 6 and Fig. 7, respectively in a temperature range of -100 to 270 °C. The rectangular tensile specimens (gauge section of 3 mm · 4 mm) and miniature tensile specimens (gauge section of 1 mm · 2 mm) were loaded with an actuator speed of 1 mm/min and 0.25 mm/min, respectively. The travel on the rectangular tensile specimens (Fig. 6) was measured with a mechanical axial extensometer. Because of the situation in the hot cell and the small size of the miniature tensile specimens (Fig. 7), the travel was measured with an extensometer attached on the clamping device.

The temperature dependence of the measured yield tensile strength values were approximated according to a relation proposed by Margolin [Margolin-2017]:

$$\sigma_Y(T) = \sigma_{YG} + \sigma_{YS}(T) \quad (6)$$

where $\sigma_{YS}(T)$ is the temperature-dependent component of the yield stress:

$$\sigma_{YS}(T) = b \cdot EXP(-h \cdot (T + 273)) \quad (7)$$

Charpy Pendulum Impact Test

Charpy V-notch specimens were tested according to DIN EN ISO 148-1:2011 by an instrumented 300 J pendulum impact tester. The temperature dependences of the measured impact energies were approximated by a hyperbolic tangent.

$$KV_2(T) = A + B \cdot TANH\left(\frac{T-T_0}{C}\right) \quad (8)$$

Master Curve Testing According to ASTM E1921

Pre-cracked and side-grooved Charpy-size SE(B) specimens were monotonically loaded with an actuator speed of 0.2 mm/min (loading rate: 0.9 MPa√m/s) until they failed by cleavage instability. Standard MC reference temperatures, T_0, were evaluated with the measured

cleavage fracture toughness values, K_{Jc}, by applying the multi-temperature option of ASTM E1921. Deviating from the evaluation procedure of ASTM E1921, lower-shelf K_{Jc} values below 50 MPa√m were not size adjusted because they are not amenable to the statistical analysis methods employed in this test method [Wallin-2010]. In addition, the MC extension of the SINTAP procedure [SINTAP-1999, Wallin-2004, Viehrig-2006] and the multi modal (MM) evaluation [Wallin-2004, Viehrig-2006] was applied. A $K_{Jc\text{-}1T}$ data set is considered to be non-homogeneous if maximum likelihood non-homogeneous criteria, MLNH, in Eq. (9) is larger than 2 [Scibetta 2010]:

$$MLNH = \frac{\sigma^{MM}}{\sqrt{\beta/(r+\sigma_{exp}^2)}} \qquad (9)$$

The yield and ultimate tensile strength vs. temperature trends determined on flat and miniature tensile specimens from the neighbouring thickness locations were used for the MC evaluation.

Ductile Fracture Toughness Testing According to ASTM E1820

Crack extension curves were measured with Charpy size SE(B) specimens using the unloading compliance (UC) technique according to ASTM E1820. Following test conditions for the UC testing were applied:

- Charpy size SE(B) specimens, 20% side-grooved, a/W = 0.5,
- radius of the side grooves: 0.4 mm,
- integral knifes for COD-Clip-On extensometer,
- pre-cracking with the servohydraulic testing machine (K_{max}: 25 MPa√m, K_f: 15 MPa√m),
- test temperature range: -100 °C to 270 °C,
- loading velocity: 0.2 mm/min,
- partial unloading: 25% of the actual load,
- relaxation time: 30 s,
- distance between the unloading sequences (ΔCOD): 0.04 mm,
- unload and reload ramp rate: 100 N/s, and
- end of test criteria: 2 mm crack extension, 4 mm COD and when the load reached a value 50% below of the maximum load, whatever was exceeded first.

The recorded data of the load, the deflection and COD were evaluated according to the test standard ASTM E1820. Accordingly, J_R curves (J integral vs. Δa) were determined. Interim engineering crack initiation fracture toughness values, J_Q, were evaluated from the J_R curves. The majority of the interim J_Q values could not be qualified as J_{Ic}, because they did not adhere to the validity criteria given in the test standard ASTM E1820. The J_Q values were converted into their equivalents in units of stress intensity factors K_{JQ}. For some tests on the cladding material, all J-Δa data between the 0.15 mm and 1.5 mm exclusion line could not be used for the fitting of the power law regression line because of their unsteady progression. Otherwise the regression line would intersect the 0.2 mm offset line away from the data points, which results in an unrealistic J_Q value.

Test Results

Unit 1 RPV

As stipulated in Table 1 a region of 0.7 m above and below the circumferential beltline welding seam No. SN0.1.4. of the Greifswald Unit 1 RPV was large scale annealed.

Thereafter, the Unit was operated for another two campaigns. Table 7 contains the estimated neutron fluences at the inner and outer RPV till annealing and for the re-irradiation and the critical embrittlement temperatures estimated according to the Russian code [PNAEG-1986] and the TT_{41J} measured on KLST specimens sampled from the beltline welding seam SN0.1.4. at the inner wall of the RPV after annealing [Ahlstrand-1999].

Beltline welding seam SN0.1.4.

The detailed progression of the neutron fluence through the thickness of the Unit 1 RPV beltline welding seam is summarized in Table A 1. Fig. 13 shows the progression of the hardness HV10 through the thickness of the beltline welding seam SN0.1.4. The HV10 values were measured on plane LS and TS of 0.4T-SE(B) specimens. The hardness varies through the thermally annealed and re-irradiated multilayer welding seam. There is no systematic hardness decrease through the thickness due to the reduction in neutron fluence. Because of the low fluence of the re-irradiation the hardness is mainly influenced by the microstructure of the multilayer welding seam.

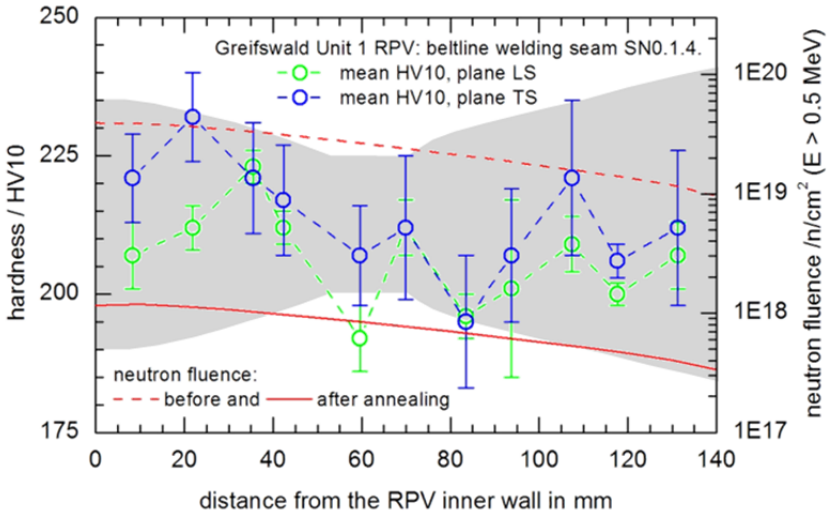

Fig. 13: Progression of the hardness HV10 and the neutron fluence through the large scale thermally annealed and re-irradiated beltline welding seam SN0.1.4. of the Greifswald Unit 1 RPV (trepan 1-1).

Table A 8 summarizes the fit parameters of Eq. (6) evaluated with tensile specimens from different thickness locations of the beltline welding seam SN0.1.4 of the Unit 1 RPV. Fig. 14 graphically depicts the temperature dependence of the yield and ultimate tensile strength. The strength values can roughly be grouped in two levels, before and beyond the welding root. Before and in the area of the welding root higher values were measured. As shown in Fig. 15, the room temperature yield and ultimate tensile strength values show a slight decrease through the thickness of the welding seam towards the RPV outer wall.

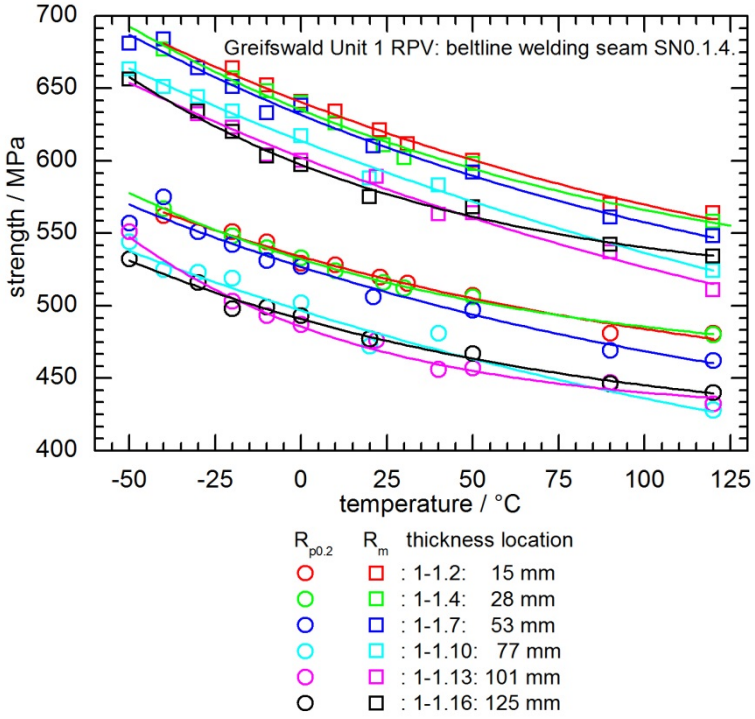

Fig. 14: Tensile strength vs. temperature measured on rectangular tensile specimens from different thickness locations of the large scale thermally annealed and re-irradiated beltline welding seam SN0.1.4. of the Greifswald Unit 1 RPV (trepan 1-1).

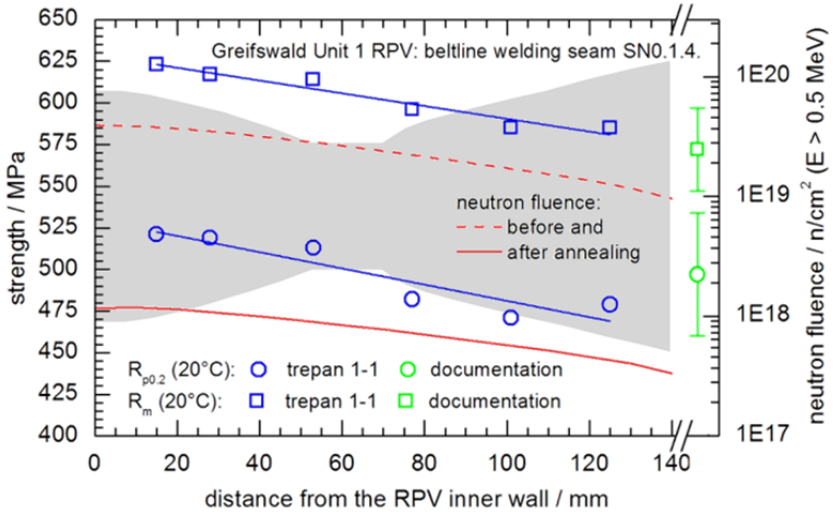

Fig. 15: Progression of the tensile strength through the thickness of the large scale thermally annealed and re-irradiated beltline welding seam SN0.1.4. of the Greifswald Unit 1 RPV (trepan 1-1).

Table A 9 summarizes the fit parameters according to Eq. (8) evaluated with impact energies measured on Charpy V-notched specimens from different thickness locations. The impact energy-temperature dependence is shown graphically in Fig. 16. Fig. 17 shows the progression of the ductile-to-brittle transition temperatures TT_{47J} measured on reconstituted Charpy V-notched specimens. It shows the expected decreasing trend from 62 °C at the location near the inner RPV wall towards a mean value of about 23 °C outside of the welding root region. Taking into account an estimated T_K of 186 °C after 13 campaigns operation (Table 7), the results presented here and the results determined on sub size impact specimens (Table 7 [Ahlstrand-1999]) show that the embrittlement was almost fully mitigated due to the

large scale recovery annealing. The re-embrittlement during the 2 campaigns operation can be assumed to be low.

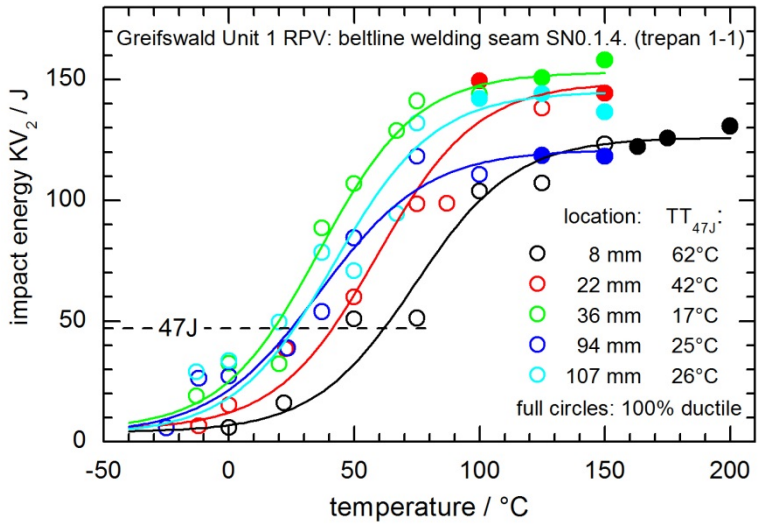

Fig. 16: Impact energy, KV_2, vs. temperature measured on Charpy V-notched specimens from different thickness locations of the large scale thermally annealed and re-irradiated beltline welding seam of the Greifswald Unit 1 RPV (trepan 1-1).

The MC test results evaluated according to ASTM E1921 are summarized in Table A 10. Fig. 17 graphically depicts the progression of MC reference temperature, T_0, and the accumulated neutron fluences through the beltline welding seam SN0.1.4.. After an initial increase of T_0 from 9 °C at the inner surface to 49 °C at 22 mm distance from it, T_0 decreases to -36 °C at a distance of 70 mm, finally increasing again to a maximum 59 °C near the outer RPV wall. The lowest T_0 value was measured in the joint region of the passes welded from the inner and outer wall (Fig. 9).

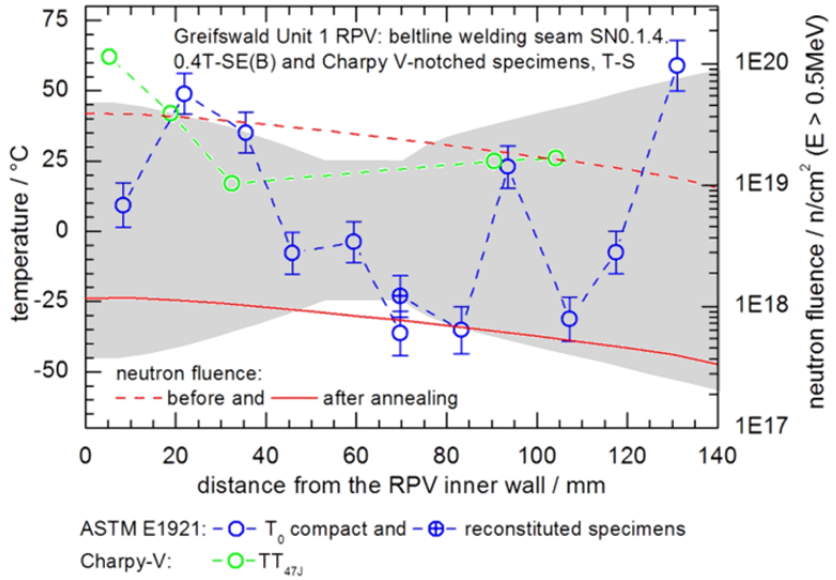

Fig. 17: Progression of the MC reference temperature T_0, Charpy-V TT_{47J} and the neutron fluence through the large scale thermally annealed and re-irradiated beltline welding seam SN0.1.4 of Greifswald Unit 1 RPV (trepan 1-1).

At 70 mm a T_0 value of -23 °C was measured with additionally tested reconstituted specimens. Hence, for the same thickness location, a difference in T_0 of 13 K was determined. The reason is due to the different locations of the crack tips in the weld bead microstructure of

the original compact and reconstituted specimens. Beyond the welding root, T_0 also varies with a span of about 59 K.

Fig. 18 depicts the microstructure in the vicinity of the crack tip of T-S oriented SE(B) specimens at thickness locations of 22 mm and 70 mm. Generally, T-S oriented specimens had a uniform microstructure along the fatigue crack front (plane LS). The crack tip of specimens from different thickness locations was located in unequal welding beads. At a thickness location of 22 mm (Fig. 18a) the crack tip was located in a coarse grain bainitic microstructure, whose grains are framed with pro-eutectoid ferrite. This coarse grain microstructure resulted in a T_0 of 49 °C. For comparison, Fig. 18b shows the microstructure in the region of the welding root in a thickness location of 70 mm, where a T_0 of -36°C was determined. There, the crack tip was located directly in a fine grain microstructure of high ferrite content. Hence, the variation of T_0 measured through the thickness of the multilayer welding seam SN0.1.4. resulted basically from differences in the microstructure of the welding beads. In contrast to the T_0 measured on fatigue pre-cracked specimens, the Charpy-V transition temperature measured on notched specimens was less sensitive to different microstructures.

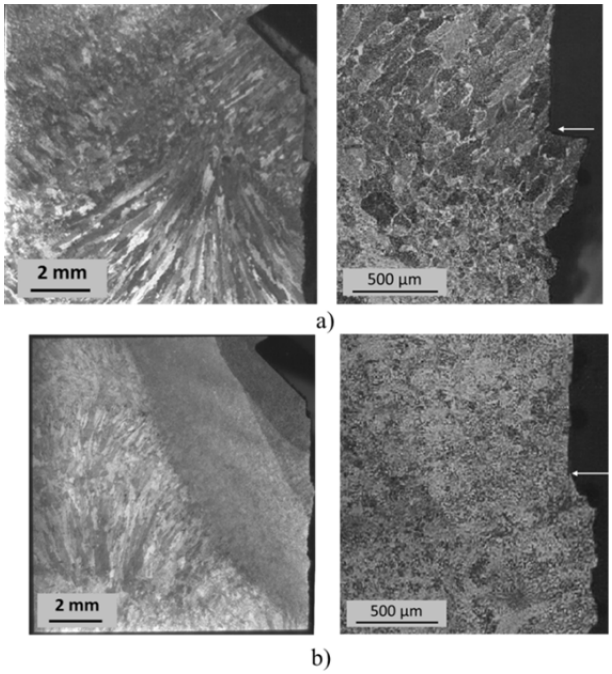

Fig. 18: Metallographic sections of the T-S oriented SE(B) specimens from thickness location a) 22 mm (T_0 = 49 °C) and b) the welding root location 70 mm (T_0 = -36 °C), arrow at fatigue crack tip location.

Fig. 19 shows the $K_{Jc\text{-}1T}$ values versus the test temperature normalised with single-specimen-set T_0 values. The K_{Jc} values generally followed the trend of the MC, though the scatter was large. Nevertheless, 5 out of about 109 $K_{Jc\text{-}1T}$ values (4.6 %) lie below the 2 % fracture probability curve (Table A 10).

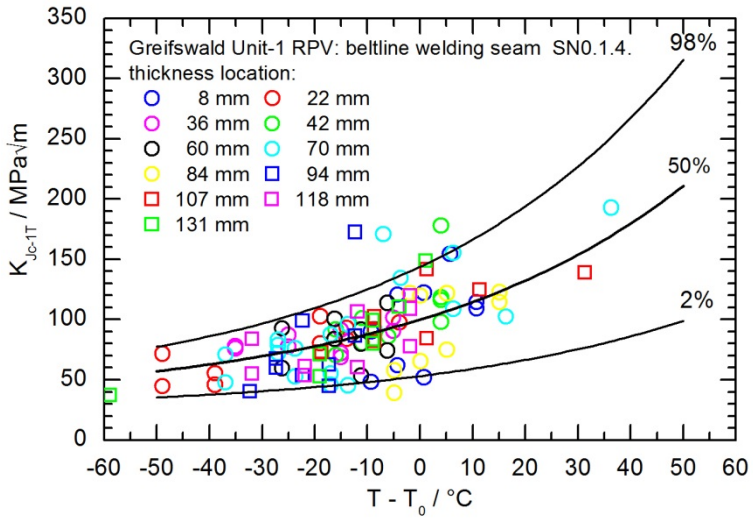

Fig. 19: $K_{Jc\text{-}1T}$ values normalised with the single-specimen-set T_0 values and MCs of the large scale thermally annealed and re-irradiated beltline welding seam SN0.1.4. of the Unit 1 RPV (trepan 1-1).

Beyond the welding root till 25 mm distance from the outer RPV wall, a mean T_0 was calculated to be -19 °C, whereby the total span between the maximal and minimal T_0 is 59 K (Fig. 17). Within this thickness location, the decline of the neutron loading during the re-irradiation for two campaigns (Table 7) can be neglected and the K_{Jc} values were summarized and evaluated according to ASTM E1921.

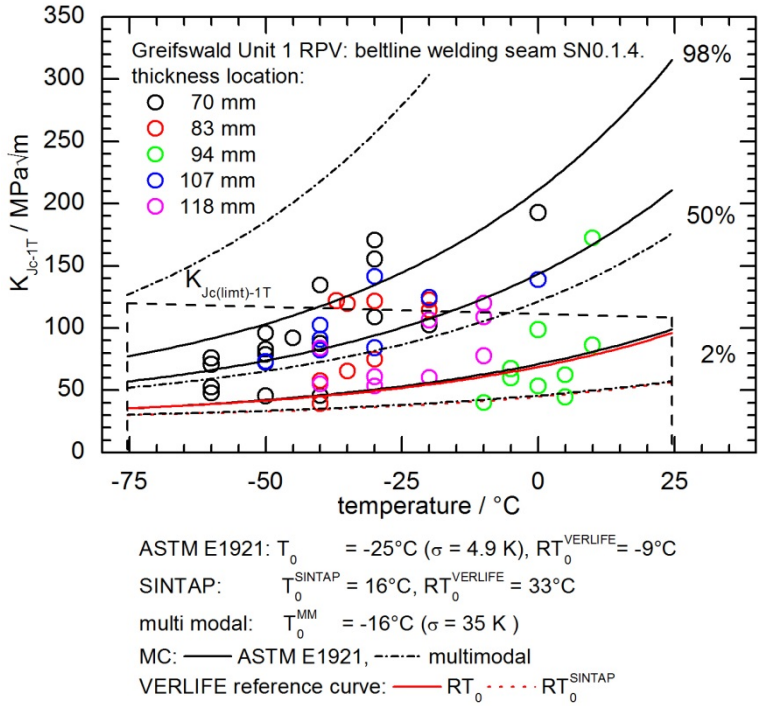

Fig. 20: $K_{Jc\text{-}1T}$ values, standard MCs and MM fracture toughness and VERLIFE reference curves measured with 0.4T-SE(B) specimens sampled from thickness locations beyond the welding root till 25 mm from the outer wall of the large scale thermally annealed and re-irradiated beltline welding seam SN0.1.4. of the Unit 1 RPV (trepan 1-1).

The result of the evaluation is summarized in Table A 26 and graphically depicted in Fig. 20. The large scatter of $K_{Jc\text{-}1T}$ values could be expected because of the span of T_0 resulting from the heterogeneous welding bead microstructure through the thickness of the multilayer

welding seam (Fig. 17). In total 7 out of 55 $K_{Jc\text{-}1T}$-values (13 %) mainly from the thickness location of 94 mm (T_0 = 22 °C) are not enveloped by the 2 % MC and hence resulted in a T_0 value which is not adequate. In this case modified MC-based evaluation procedures have to be applied like SINTAP [SINTAP-1999] and multi modal approach [Wallin-2004, Viehrig-2006, Scibetta-2010] to get fracture toughness values which are representative for the most brittle fraction and the continuous distribution of $K_{Jc\text{-}1T}$ values, respectively. Fig. 20 contains also the MM fracture toughness and the VERLIFE reference curves indexed with T_0 and T_0^{SINTAP}. The 2% MM fracture toughness curve and the SINTAP reference curve do not envelop 2 out of 55 $K_{Jc\text{-}1T}$ values (3.6%). The MLNH value according to Eq. (9) of the evaluated weld metal (Fig. 20) amounts to 7.2 and is consequently assessed to be non-homogeneous.

The results of the J_R testing according to ASTM E1820 are summarized in Table A 11. Fig. 21 shows the progression of the interim J_Q values through the thickness of the beltline welding seam SN0.1.4. of Greifswald Unit 1. At the test temperature of 200 °C a mean J_Q of 147 kJ/m^2 was determined for the filling layers before and beyond the welding root. The maximum J-integral capacity of the 0.4T-SE(B) specimen amounts about 250 kJ/m^2 at this test temperature.

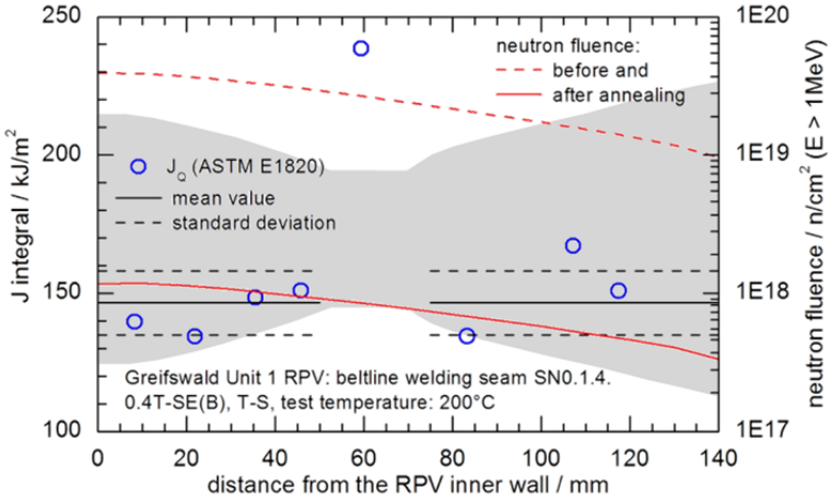

Fig. 21: J_Q values measured with 0.4T-SE(B) specimens sampled through the thickness of the large scale thermally annealed and re-irradiated beltline welding seam SN0.1.4. of the Unit 1 RPV (trepan 1-1).

Forged base metal ring 0.3.1.

The trepan from the Unit 1 forged base metal ring 0.3.1 was sampled from the thermally annealed region 200 mm above the beltline welding seam SN0.1.4.. The detailed progression of the neutron fluence through the thickness at the sampling position is summarized in Table A 2.

The hardness HV10 was measured in three lines on the plane TS of a 0.4T-SE(B) specimen beyond the fractured surface as exemplarily depicted in Fig. 46. Fig. 22 shows the progression of the hardness HV10 through the large scale thermally annealed and re-irradiated forged base metal ring 0.3.1.. The highest hardness values were measured at the RPV inner wall. There is a slight decrease towards the RPV outer wall, but in the scatter band.

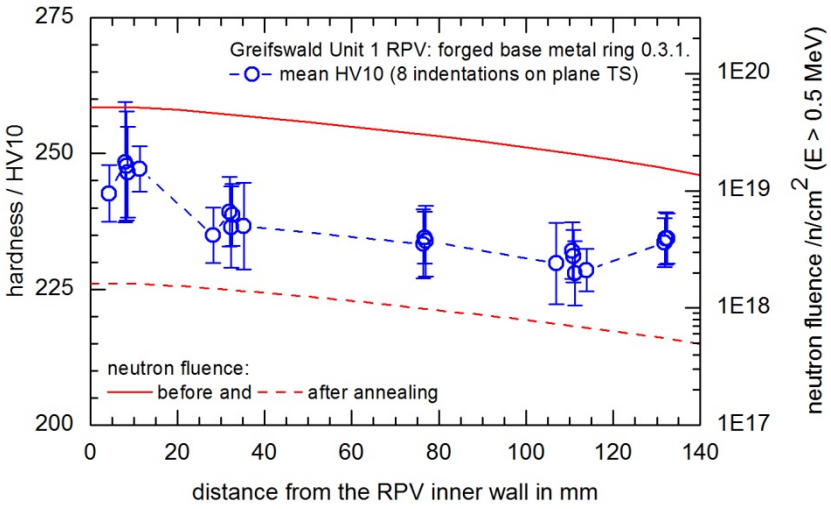

Fig. 22: Progression of the hardness HV10 and the neutron fluence through the large scale thermally annealed and re-irradiated forged base metal ring 0.3.1. of the Greifswald Unit 1 RPV (trepan 1-4).

As shown in Fig. 23 the yield and ultimate tensile strength measured in different thickness locations do not differ and the temperature dependency was therefore evaluated together (Table A 12).

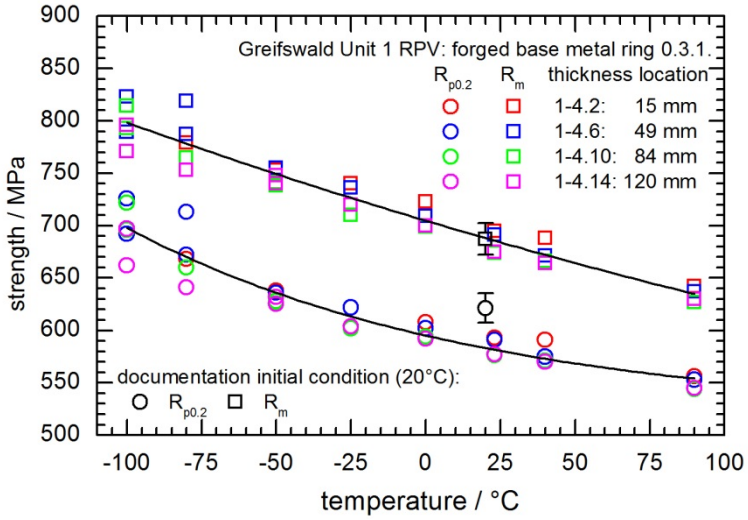

Fig. 23: Tensile strength vs. temperature measured on rectangular tensile specimens from different thickness locations of the large scale thermally annealed and re-irradiated forged base metal ring 0.3.1. of the Greifswald Unit 1 RPV (trepan 1-4).

Fig. 24 shows the KV_2 values measured on Charpy V-notched specimens from different thickness locations of the forged base metal ring 0.3.1. versus the test temperature. The KV_2 values strongly scatter. The tanh fit parameter and the evaluated TT_{47J} DBTT of the different thickness locations and the joint evaluation are summarized in Table A 9. The decreasing trend of the TT_{47J} values towards outer wall lies within the uncertainty of the Charpy-V impact test. Therefore, the values from the different thickness locations were evaluated together. The fitted curve is depicted in Fig. 24. As shown in Fig. 24 the KV_2 values are mainly within a span of $TT_{47J} \pm 35$ K.

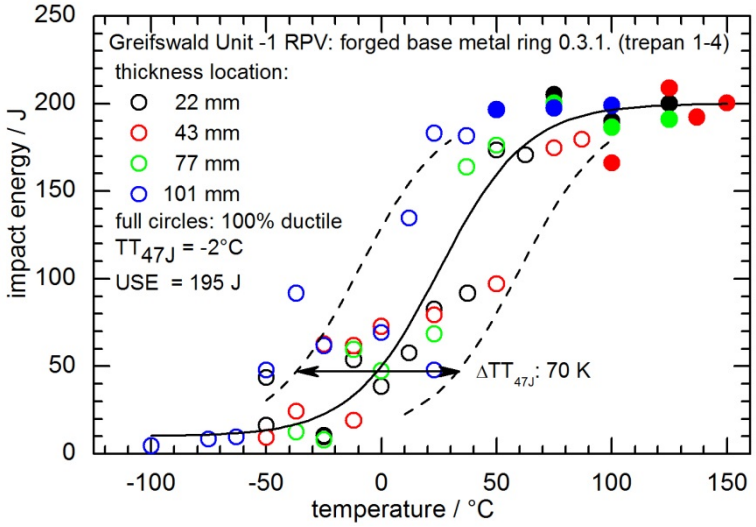

Fig. 24: Impact energy vs. temperature measured on Charpy V-notched specimens from different thickness locations of the large scale thermally annealed and re-irradiated forged base metal ring 0.3.1. of the Greifswald Unit 1 RPV (trepan 1-4).

Table A 14 summarizes the results of the MC evaluation of the $K_{Jc\text{-}1T}$ values measured on SE(B) specimens from different thickness locations of the forged base metal ring 0.3.1.. The progression of T_0 through the forged base metal ring 0.3.1. is shown in Fig. 25. Close to the inner and outer wall T_0 values of -116 °C and -120 °C were determined, respectively. Within the ¼ to ¾ thickness location, the mean value of T_0 amounts -107 °C with a standard deviation of 3 K. Taking into account the estimated T_K of 0 °C (Table 7), the base metal (±700 mm above SN0.1.4.) can be assumed to be fully mitigated by the large scale thermal annealing.

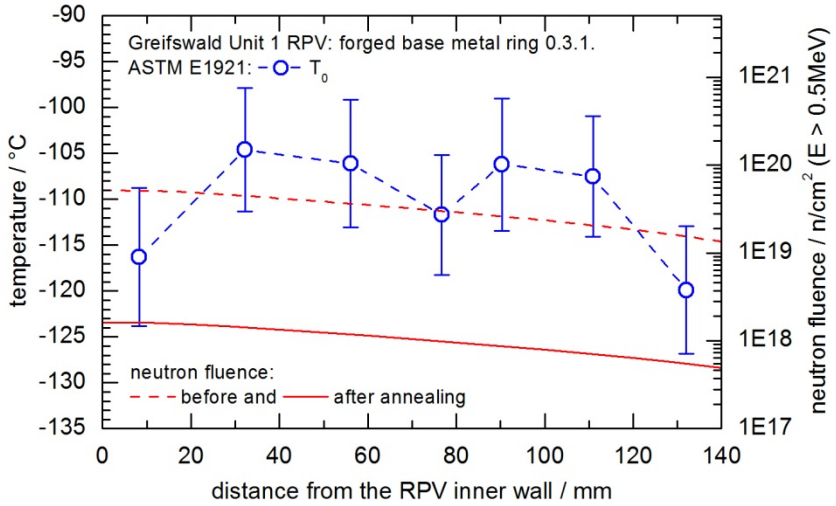

Fig. 25: Progression of the MC reference temperature, T_0, and the neutron fluence through the large scale thermally annealed and re-irradiated forged base metal ring 0.3.1 of the Greifswald Unit 1 RPV (trepan 1-4).

Fig. 26 summarizes the $K_{Jc\text{-}1T}$ values versus the test temperature normalised with the single-specimen-set T_0 values. The $K_{Jc\text{-}1T}$ values generally follow the MC description, but the scatter is large and 15 out of 84 $K_{Jc\text{-}1T}$ values (17.8%) are not enveloped by the 2% and 98% tolerance curves (Table A 14).

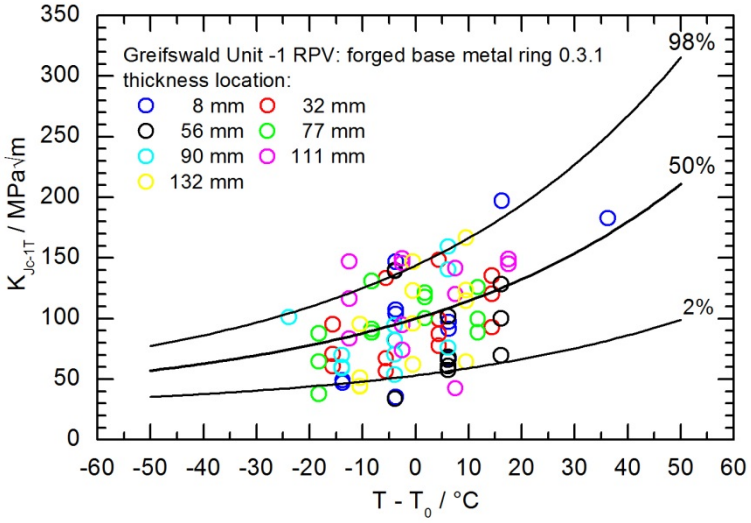

Fig. 26: $K_{Jc\text{-}1T}$ values normalised with the single-specimen-set T_0 values and MCs of the large scale thermally annealed and re-irradiated forged base metal ring 0.3.1. of the Greifswald Unit 1 RPV (trepan 1-4).

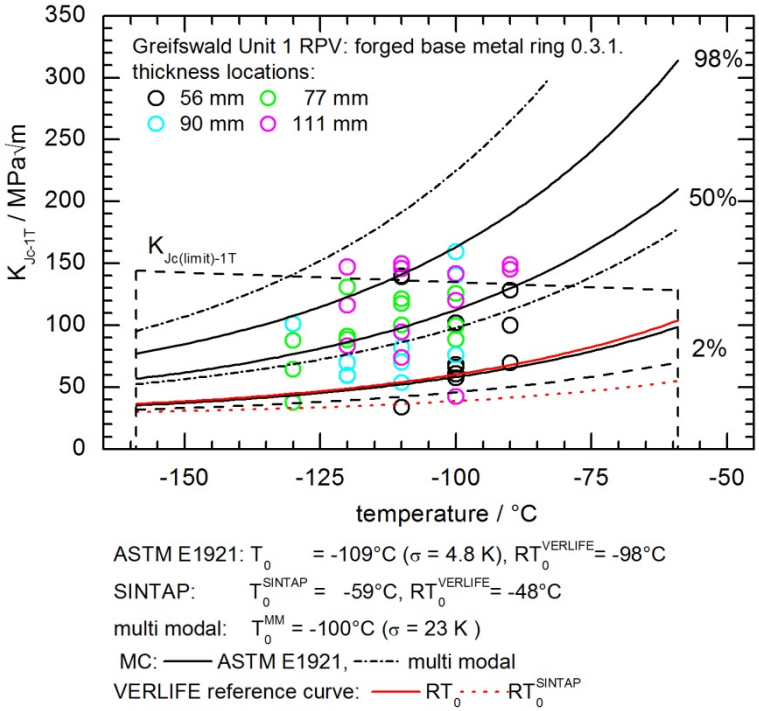

Fig. 27: $K_{Jc\text{-}1T}$ values, standard MCs and MM fracture toughness and VERLIFE reference curves measured with 0.4T-SE(B) specimens sampled from WWER-440 generation 2 surveillance thickness locations of the large scale thermally annealed and re-irradiated forged base metal ring 0.3.1. of the Greifswald Unit 1 RPV (trepan 1-4).

The collective evaluation of $K_{Jc\text{-}1T}$ values measured on specimens sampled from the thickness locations at a distance between 30 mm and 90 mm from the RPV outer wall, where the surveillance specimens of the WWER-440 second generation RPV origin [Brumovsky-2005], is depicted in Fig. 27. Here a T_0 of -109 °C is evaluated which is comparable with the mean value of the ¼- to ¾-T single series evaluation. The scatter is large and 4 out of 49 $K_{Jc\text{-}1T}$ values (8.2%) are not enveloped by the 2% MC. The VERLIFE reference curve does not envelop 5 out of 49 $K_{Jc\text{-}1T}$ values (10.2 %). Also the MM evaluation does not improve substantially the situation, also here 3 out of 49 $K_{Jc\text{-}1T}$ values are not enveloped by the 2%

MM fracture toughness curve. The MLNH value according to Eq. (9) of the evaluated base metal (Fig. 27) amounts to 4.8 and is consequently assessed to be non-homogeneous. The VERLIFE reference curve indexed with RT_0^{SINTAP} MC does not envelop 1 $K_{Jc\text{-}1T}$ value (2%).

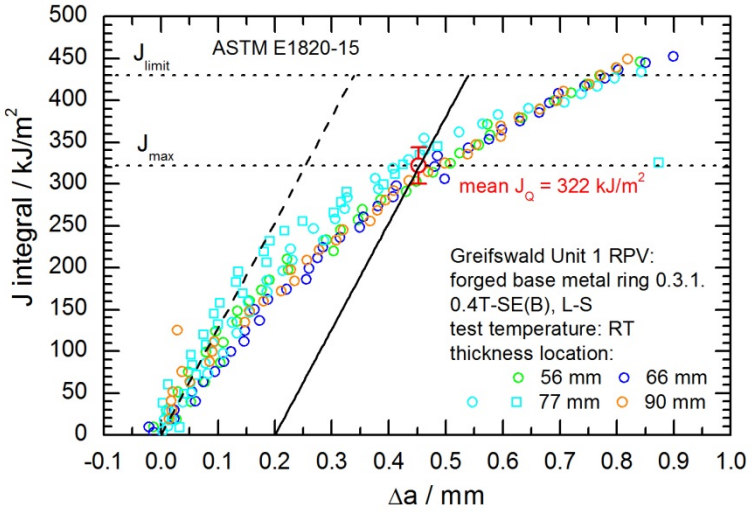

Fig. 28: J vs. Δa data measured on 0.4T-SE(B) specimens from thickness locations between ¼-T to ¾-T from the forded base metal ring 0.3.1. of the Unit 1 RPV.

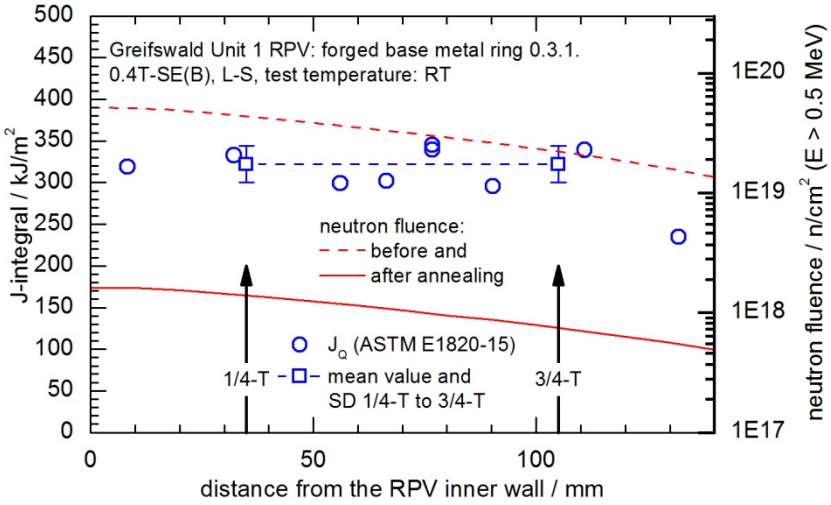

Fig. 29: J_Q values measured with 0.4T-SE(B) specimens sampled through the thickness of the large scale thermally annealed and re-irradiated forged base metal ring 0.3.1. of the Greifswald Unit 1 RPV (trepan 1-4).

The results of the J_R testing according to ASTM E1820 are summarized in Table A 15. Fig. 28 shows the J versus Δa data measured on 0.4T-SE(B) specimens from thickness locations between ¼-T to ¾-T from the forded base metal ring 0.3.1. of the Unit 1 RPV. The mean value $J_{Q/IC}$ value was 322 kJ/m² and the standard deviation 22 kJ/m², which corresponds approximately to the maximum J-integral capacity of the 0.4T-SE(B) specimen of 320 kJ/m² at room temperature. The inhomogeneity of the base metal 15Kh2MFA resulted in a large scatter of the interim J_Q values through the thickness of the forged base metal ring shown in Fig. 29. The low J_Q of specimen 1-4.16.263 (Table A 15) from the thickness location close to the RPV outer wall resulted from a shallow slope of the J - Δa data between 0.1 mm and 0.3 mm. Also pop-ins cannot be excluded at RT, which is shown for the second specimen from the thickness location 77 mm (Fig. 28).

Unit 2 RPV

Beltline welding seam SN0.1.4.

The circumferential beltline welding seam SN0.1.4. of the Greifswald Unit 2 RPV was large scale thermally annealed and not put in operation afterwards (Table 1). Table 7 contains the estimated neutron fluences at the inner and outer RPV wall till large scale annealing, the critical embrittlement temperatures estimated according to the Russian code [PNAE-1986] and the TT_{41J} measured on KLST specimens sampled from the beltline welding seam SN0.1.4. at the inner wall of the RPV after annealing [Ahlstrand-1999]. From this Unit, only the trepan sampled from the beltline welding seam SN0.1.4. has been investigated. The detailed progression of the neutron fluence through its thickness is summarized in Table A 3. The shape of the welding seam equated to the documentation [Boehmer-1999] and hence was the original first welding seam.

Fig. 30 shows the progression of the hardness HV10 through the large scale thermally annealed beltline welding seam SN0.1.4.. The hardness was measured on the planes TS and LS (Fig. 6) of a SE(B) specimens at VTT Espoo [Valo-2010] and HZDR, respectively. The single values on plane TS strongly scatter with a decreasing trend towards the RPV outer wall. Also, the mean values of 8 indentations measured on plane LS strongly scatter. They do not show any trend towards the thickness of the welding seam SN0.1.4..

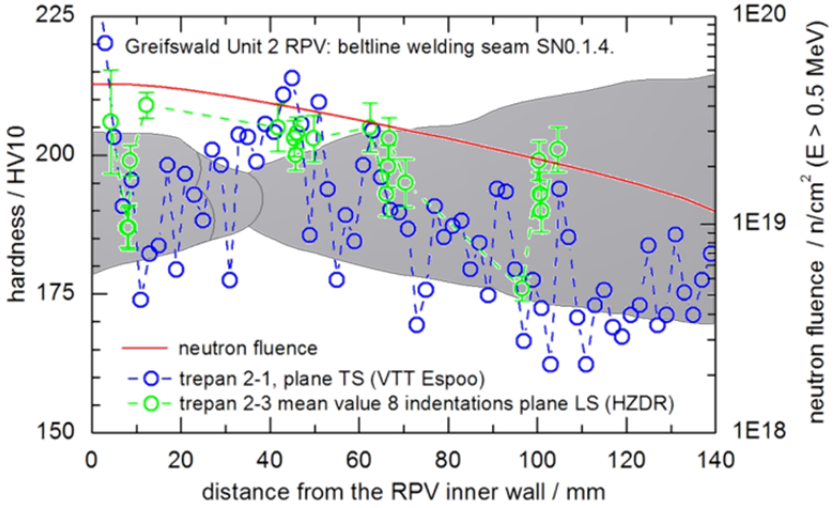

Fig. 30: Progression of the hardness HV10 and the neutron fluence through the large scale thermally annealed beltline welding seam SN0.1.4. of the Greifswald Unit 2 RPV.

There is also no continuous trend of the yield and ultimate tensile strength measured in different thickness locations as shown in Fig. 31. The strength vs. temperature fitting parameter according to Eq. (6) are summarized in Table A 16. Fig. 32 shows the decreasing progression of the yield and ultimate tensile strength estimated at 20 °C through the thickness of the Unit 2 RPV beltline welding seam SN0.1.4. (Table A 16).

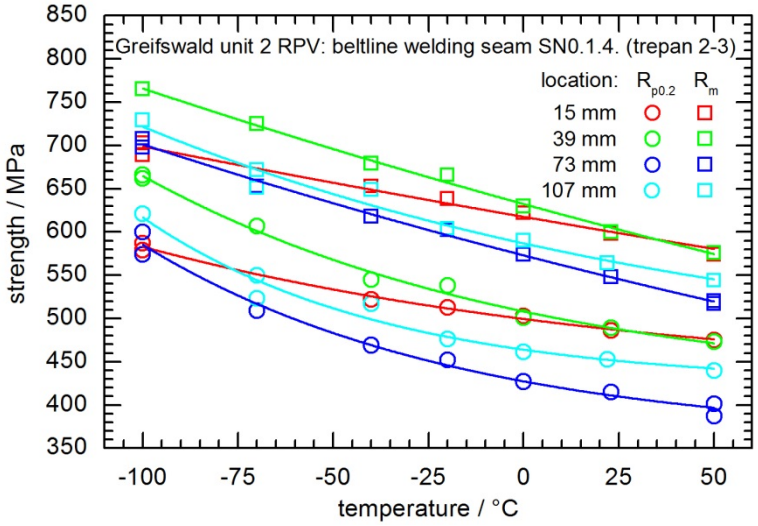

Fig. 31: Tensile strength vs. temperature measured on rectangular tensile specimens from different thickness locations of the large scale thermally annealed beltline welding seam SN0.1.4. of the Greifswald Unit 2 RPV (trepan 2-3).

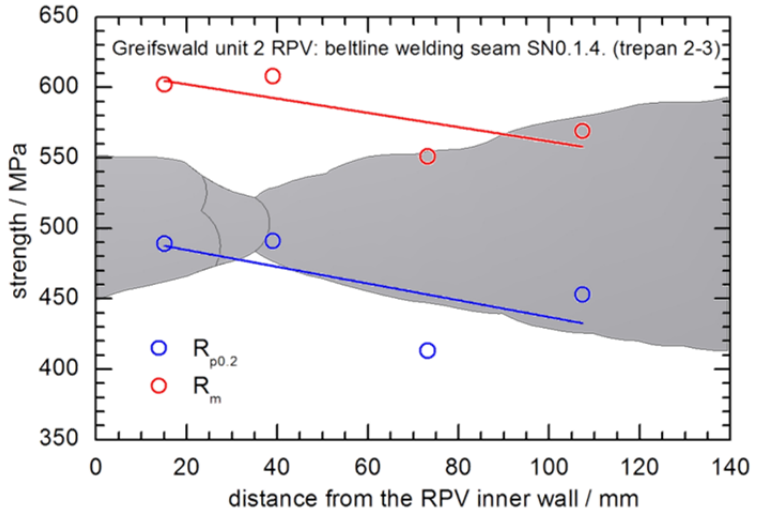

Fig. 32: Progression of the tensile strength through the thickness of the large scale thermally annealed beltline welding seam SN0.1.4. of the Greifswald Unit 2 RPV (trepan 2-3) at 20 ˚C.

Table A 17 summarizes the results of the MC evaluation of the K_{Jc} values measured on SE(B) specimens from different thickness locations of the Unit 2 RPV beltline welding seam SN0.1.4.. The progression of T_0 through this welding seam showed a strong variation (Fig. 33). Close to the inner wall T_0 values of -41 °C and -38 °C were measured. After an increase to -12 °C T_0 decreased to -62 °C in the welding root region. Beyond the welding root the T_0 varied between -43 °C and +6 °C. Taking into account the estimated T_K of 146 °C (Table 7) the welding seam can be assumed to be fully mitigated by the large scale thermal annealing. The variation of the T_0 values is likely caused by the varying welding microstructure in the vicinity of the crack tip.

Fig. 34 shows the $K_{Jc\text{-}1T}$ values versus the test temperature normalised with the single-specimen-set T_0 values. Also for this welding seam, the K_{Jc} values generally follow the trend of the MC, though the scatter is large and 12 out of about 104 $K_{Jc\text{-}1T}$ values (11.5 %) are not enveloped by the 2% and 98% tolerance curves (Table A 17).

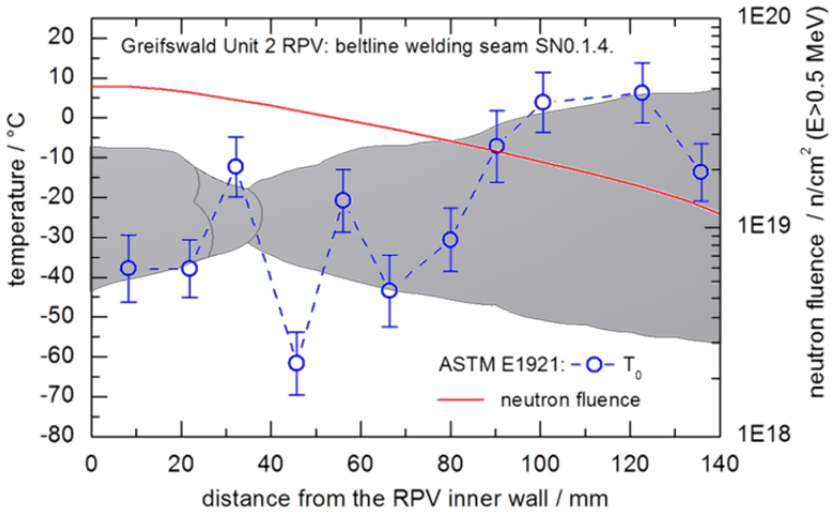

Fig. 33: Progression of the MC reference temperature T_0 and the neutron fluence through the large scale thermally annealed beltline welding seam SN0.1.4 of the Greifswald Unit 2 RPV (trepan 2-3).

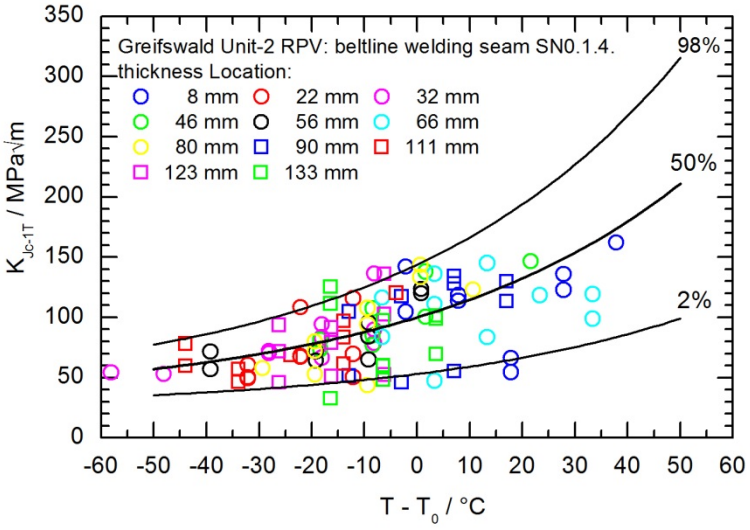

Fig. 34: $K_{Jc\text{-}1T}$ values normalised with the single-specimen-set T_0 values and MCs of the large scale thermally annealed beltline welding seam SN0.1.4 of the Greifswald Unit 2 RPV (trepan 2-3).

As stated above, the toughness of the Unit 2 beltline welding seam SN0.1.4. can be assumed to be fully mitigated by large scale thermal annealing. The collective evaluation of $K_{Jc\text{-}1T}$ values measured on specimens sampled from thickness location of the WWER 440 second generation surveillance specimens resulted in a T_0 of -26 °C (Fig. 35, Table A 26). The scatter is large and 7 out of 48 $K_{Jc\text{-}1T}$ values (14.6 %) are not enveloped by the 2 % MC which also applies to the VERLIFE reference curve. The MM evaluation results in a T_0^{MM} of -20 °C and a standard deviation of 33 K. All $K_{Jc\text{-}1T}$ values lie within the 2% and 98% MM fracture toughness curves. The MLNH value according to Eq. (9) amounts to 6.5 and the weld metal within the surveillance locations is consequently assessed to be non-homogeneous. The VERLIFE reference curve indexed with RT_0^{SINTAP} does not envelop one $K_{Jc\text{-}1T}$ value (2.1 %).

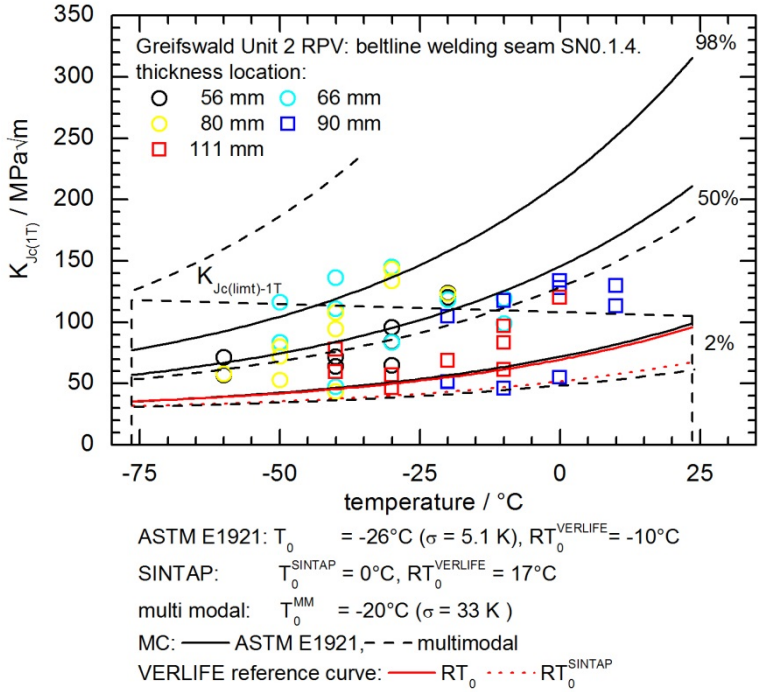

Fig. 35: $K_{Jc\text{-}1T}$ values, standard MCs and MM fracture toughness and VERLIFE reference curves measured with 0.4T-SE(B) specimens sampled from surveillance thickness locations of the large scale thermally annealed beltline welding seam SN0.1.4. of the Greifswald Unit 2 RPV (trepan 2-3).

Unit 4 RPV

The Greifswald Unit 4 RPV was operated for 11 campaigns. Table 7 contains the neutron fluences at the outer and inner RPV wall and the critical embrittlement temperatures estimated according to the Russian code [PNAEG-1986].

Beltline welding seam SN0.1.4.

The detailed progression of the neutron fluence through the thickness of the Unit 4 RPV beltline welding seam is summarized in Table A 6 (trepan 4-4) and Table A 7 (trepan 4-6).

The influence of the neutron fluence on the hardness and strength through the thickness of the Unit 4 beltline welding seams SN0.1.4. is depicted in Fig. 36 and Fig. 38, respectively.

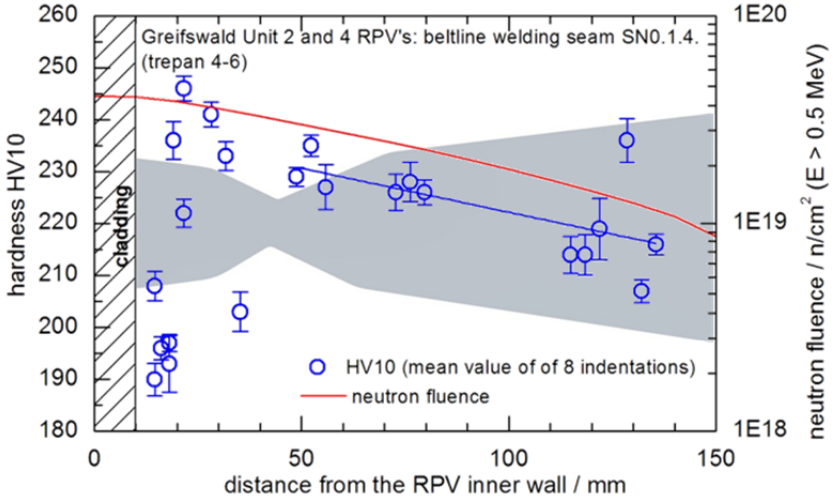

Fig. 36: Progression of the hardness HV10 through the beltline welding seam SN0.1.4. of the Greifswald Unit 4 RPV (trepan 4-6).

The hardness values show a large scatter which indicates the inhomogeneous welding bead microstructure. Beyond the cladding up to about 20 mm thickness the hardness is influenced by the welding of the cladding. However, there is a decreasing trend beyond the welding root towards the RPV outer wall (Fig. 36).

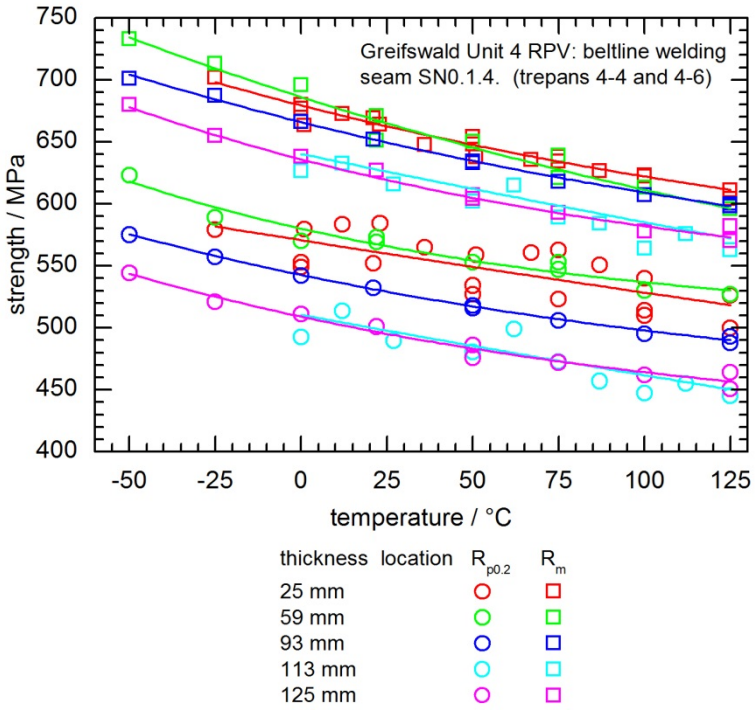

Fig. 37: Tensile strength vs. temperature measured on rectangular and miniature tensile specimens from different thickness locations of beltline welding seam SN0.1.4. of the Greifswald Unit 4 RPV (trepans 4-4 and 4-6).

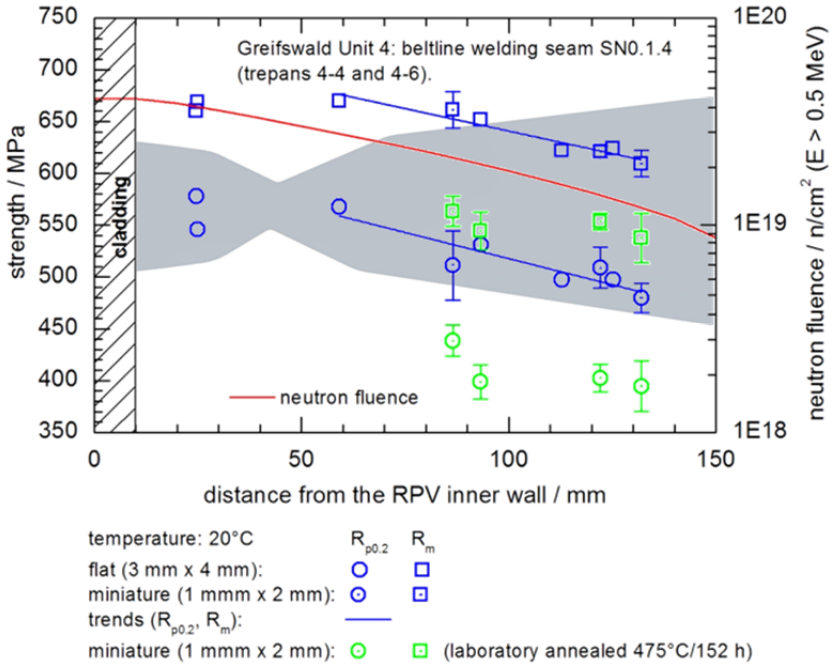

Fig. 38: Progression of the strength through the beltline welding seam SN0.1.4. of the Greifswald Units 4 RPV (trepans 4-4 and 4-6).

Fig. 37 shows the temperature dependence of the yield and ultimate tensile strength measured on specimens from different thickness locations of the Unit 4 beltline welding seam SN0.1.4.. The fitting parameters according to Eq. (6) are summarized in Table A 18. Also the yield and

ultimate tensile strength values show a decreasing trend beyond the welding root of Unit 4 beltline welding seam. The tensile values measured on specimens sampled from the large-scale thermally annealed Unit 2 beltline welding seam are significantly lower (Fig. 32) and comparable with laboratory thermally annealed specimens from the Unit 4 beltline welding seam (Fig. 38). The mitigation of the hardness and strength due to large scale thermal annealing is clearly indicated.

For comparison with the current approach to determine the critical temperature of brittleness according to the Russian code [PNAEG-1986], the progression of the Charpy-V ductile-to-brittle transition temperature TT_{47J} through the thickness of the Unit 4 beltline welding seam was determined (Fig. 39). In addition to the measured TT_{47J} the critical embrittlement temperature, T_K, predicted according to Eqs. (1) and (2) is also depicted. The T_{K0} is based on the TT_{47J} of 14°C measured on thermally annealed Charpy V-notched specimens from thickness locations beyond the welding root (Fig. 40). Further ΔT_K (Eq. (2)) takes into account the attenuation of the neutron fluence and the variation of the phosphorus and copper contents at the specific thickness locations (Fig. 11). It should be noted that the used T_{K0} cannot be assumed as uniform through the thickness of the multi-layer welding seam because of the compositional variations known to be associated with the mixture of the alloyed filler with the unalloyed filler and the base metal in the vicinity of the welding root. Before and in the region of the welding root, T_K is overestimated, thereafter the TT_{47J} values scatter and lie within a span of about 16 °C. An exception is the thickness location of 140 mm, where the notch roots of the Charpy V-notched specimens are located in the cover layers welded with the unalloyed wire. In comparison to the filling layers, a higher initial toughness is expected here. Taking into account an average $A_F^{270°C}$ of 43.5 within the thickness locations from 65 mm to 150 mm, the Russian PNAEG code predicts a decrease of T_K by about 38 K, which is not measured on the tested Charpy V-notched specimens within that thickness range. Fig. 40 shows the impact energy vs. temperature curves for the irradiated and thermally annealed condition. As depicted in Fig. 39 the TT_{47J} values of the four test series within thickness locations from 59 mm to 119 mm distance from the inner RPV wall are comparable and provide an average value of 124 °C and a standard deviation of 7.4 °C (Table A 19). That means the decrease of TT_{47J} expected because of fluence reduction from 2.8 to $1.5 \cdot 10^{19}$ n/cm^2 is not visible. Therefore, the KV_2 values measured on specimens sampled from that thickness range were evaluated together and results in a TT_{47J} of 127 °C (Fig. 40, Table A 19). The thermally annealed specimens give a TT_{47J} of 21 °C (Fig. 40, Table A 19), which is 34 K higher than the T_{K0} of -13 °C as reported in the documentation [Boehmer-1999]. The resulting recovery is 106 K. As expected the slope of the impact energy curve becomes steeper due to the thermal annealing. Former results have shown that 100% mitigation can be reached with the applied thermal cycle [Viehrig-2000].

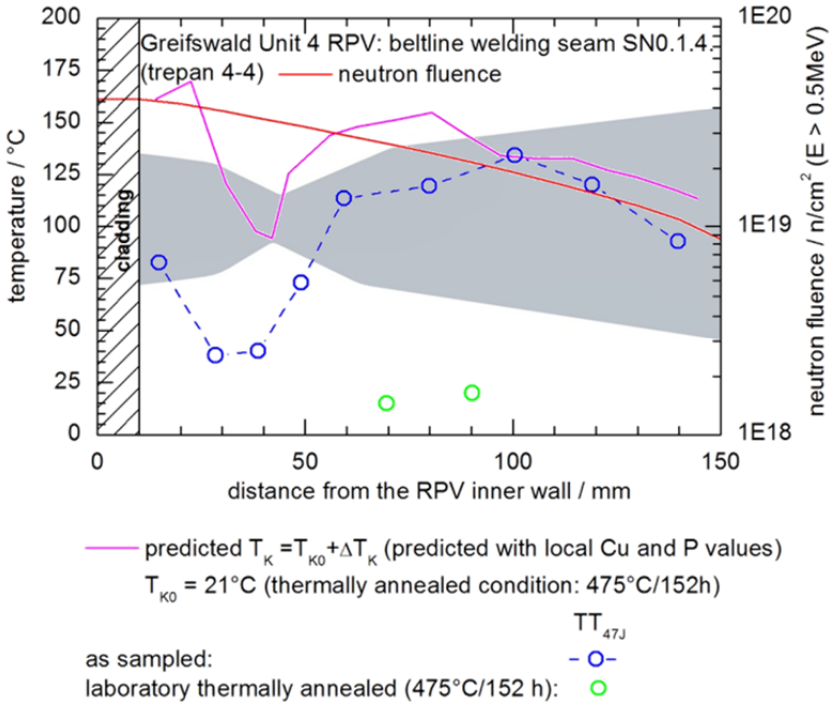

Fig. 39: Charpy-V TT_{47} and predicted T_K through the thickness of the Greifswald Unit 4 beltline welding seam SN0.1.4. measured on as sampled and laboratory thermally annealed specimens (trepans 4-4).

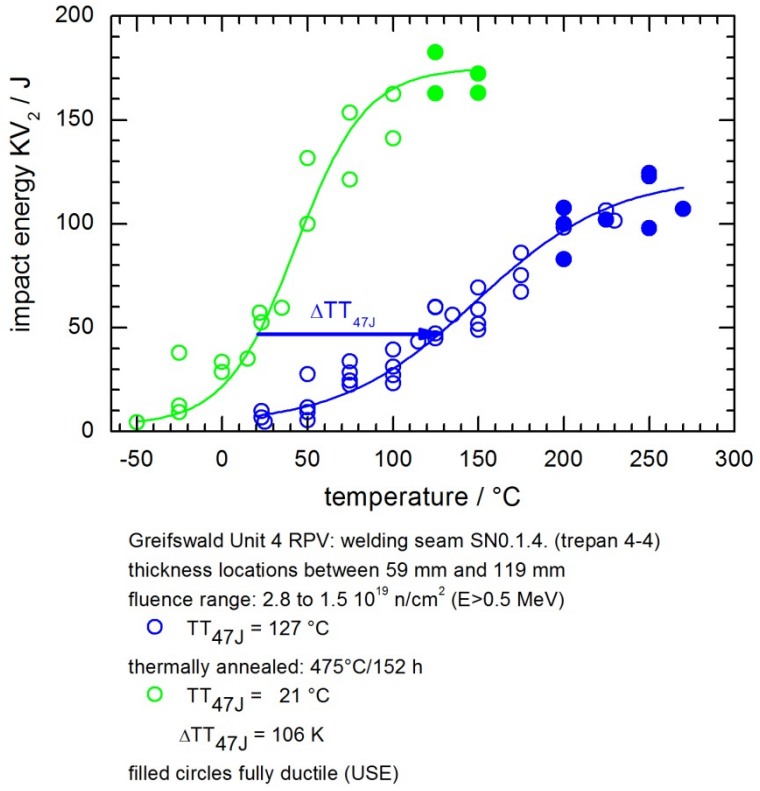

Fig. 40: Charpy-V impact energy vs. temperature of the Greifswald Unit 4 beltline welding seam SN0.1.4. in the irradiated and thermally annealed condition.

The results of the MC testing according to ASTM E1921 are summarized in Table A 20. Fig. 41 graphically depicts the progression of the T_0 values through the thickness of Unit 4 RPV

beltline welding seam SN0.1.4.. The fracture toughness values, K_{Jc}, were measured on Charpy size SE(B) specimens from the trepans 4-4 and 4-6 (Table 3). The T_0 values vary largely across the welding seam. Beyond the cladding on the inner surface, a T_0 value of 26 °C was measured. The lowest measured T_0 value was 6 °C in the root region of the welding seam. Beyond the welding root, T_0 increased continuously with a large scatter towards the outer RPV wall. The progression of the T_0 values through the thickness of the welding seam was not in accordance with the current understanding of what could be expected - a decrease in T_0 with the attenuation of the neutron fluence. The low T_0 values in the welding root region can be explained with the reduced irradiation susceptibility because of the remarkable lower Cu and P content compared to the filling layers (Fig. 11). Furthermore, in the welding root region a lower initial toughness can be expected because of the microstructure resulting from the mixture of the welding wires and the base metal from the adjacent forged rings. On the other hand, the chemical composition near the inner wall is comparable with the filling layers beyond the welding root, but the T_0 is about 55 K lower in spite of the higher neutron loading. Metallographic investigations and hardness measurements in the vicinity of the fatigue crack tip indicate that the variation of the T_0 values measured through the filling layers of the multilayer welding seam SN0.1.4. resulted basically from variation of the intrinsic welding bead microstructure [Viehrig-2012a, -2015, -2018]. Hence, the position of the fatigue crack tip in the multilayer welding seam is crucial and defines the cleavage fracture toughness. Fig. 42 shows metallographic sections of different planes in the vicinity of the crack tip of a compact (a) and a reconstituted (b) SE(B) specimen from the thickness location 118 mm. The metallographic sections of the TL planes indicated that the weld bead microstructure was uniform along the whole crack front. T_0 measured with original compact and reconstituted SE(B) specimens amounted 117 °C and 81 °C, respectively [Viehrig-2012a, -2015,-2018]. Hence, for the same neutron loading, a difference in T_0 of 36 K was determined. As shown in Fig. 42 the crack tips in the original compact and reconstituted specimens are at different locations in the weld bead microstructure. The original compact SE(B) specimen showed an increase of the grain size of the ferritic bainitic microstructure in the vicinity of the fatigue crack tip, in which the bainite content is increasing. It ended in the coarse grain bainite region surrounded by ferrite after about one millimetre crack propagation (Fig. 42a). In contrast the reconstituted specimen (Fig. 42b) showed a higher bainite content in the vicinity of the fatigue crack tip. The bainitic grains were surrounded by ferrite. The different welding bead microstructures accounted for the variation of T_0 through the multilayer welding seam.

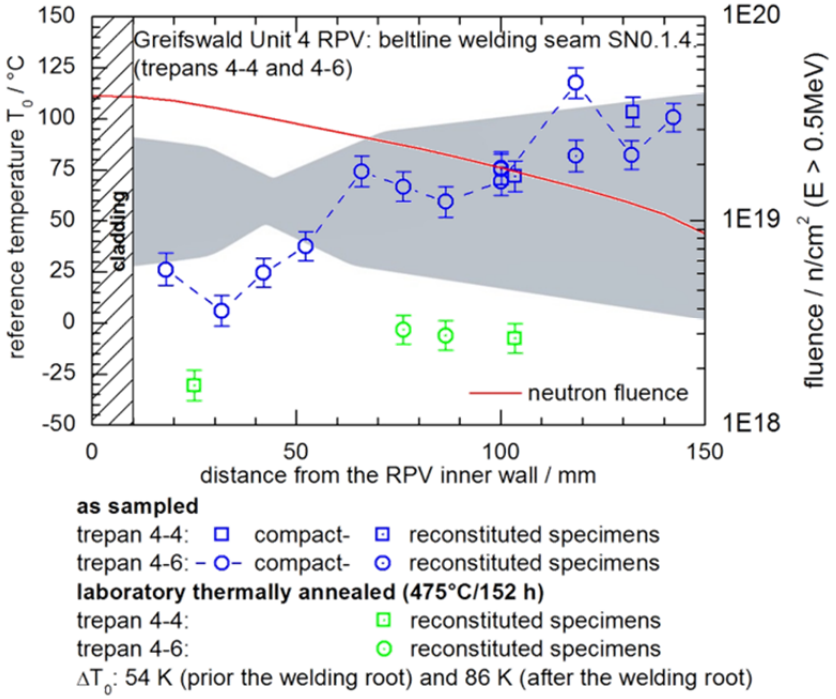

Fig. 41: Progression of the reference temperature, T_0, through the thickness of the Greifswald Unit 4 beltline welding seam SN0.1.4. measured on as sampled specimens and laboratory thermally annealed specimens (trepans 4-4 and 4-6).

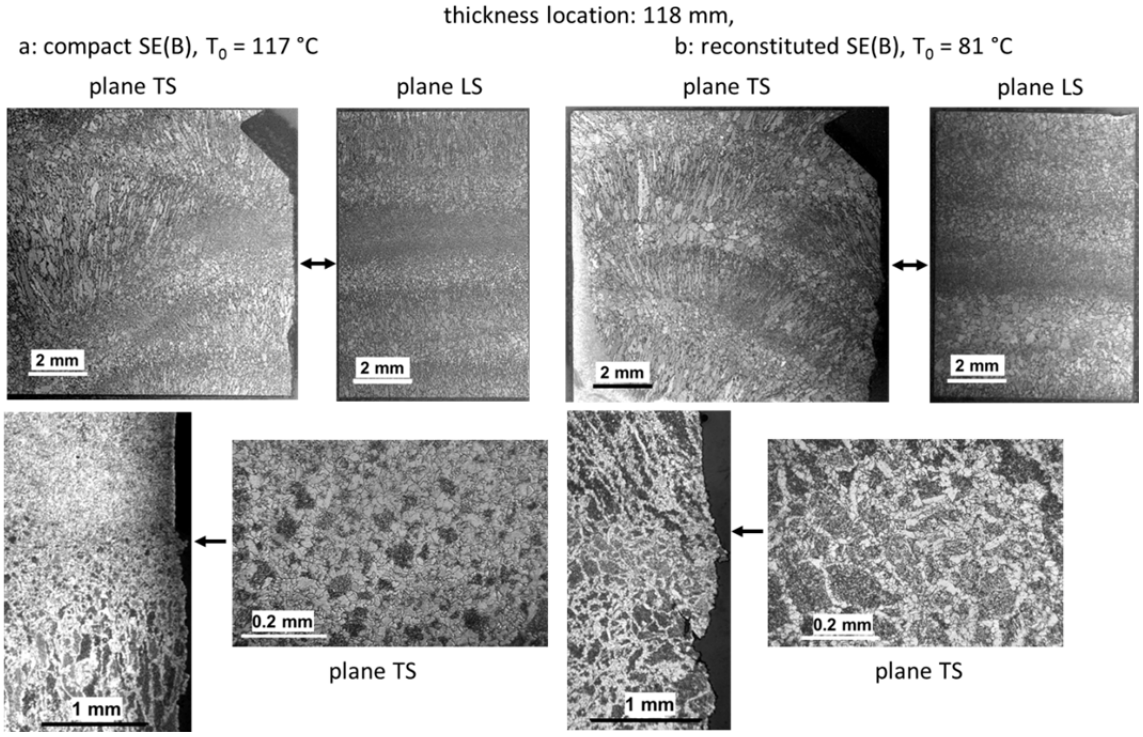

Fig. 42: Metallographic sections of a compact (a) and reconstituted (b) T-S oriented SE(B) specimen from the thickness location 118 mm of the Unit 4 beltline multilayer welding seam (arrow marks the position of the crack tip).

Fig. 43 shows SEM sections of the fractured surface of a specimen from the thickness location 118 mm with the highest T_0 of 117 °C as an example. Here the cleavage crack was initiated at misoriented grains. The specimen shows ductile dimples along the fatigue crack

front and cleavage facets in the fractured area. There are some intergranular planes, which can be ignored.

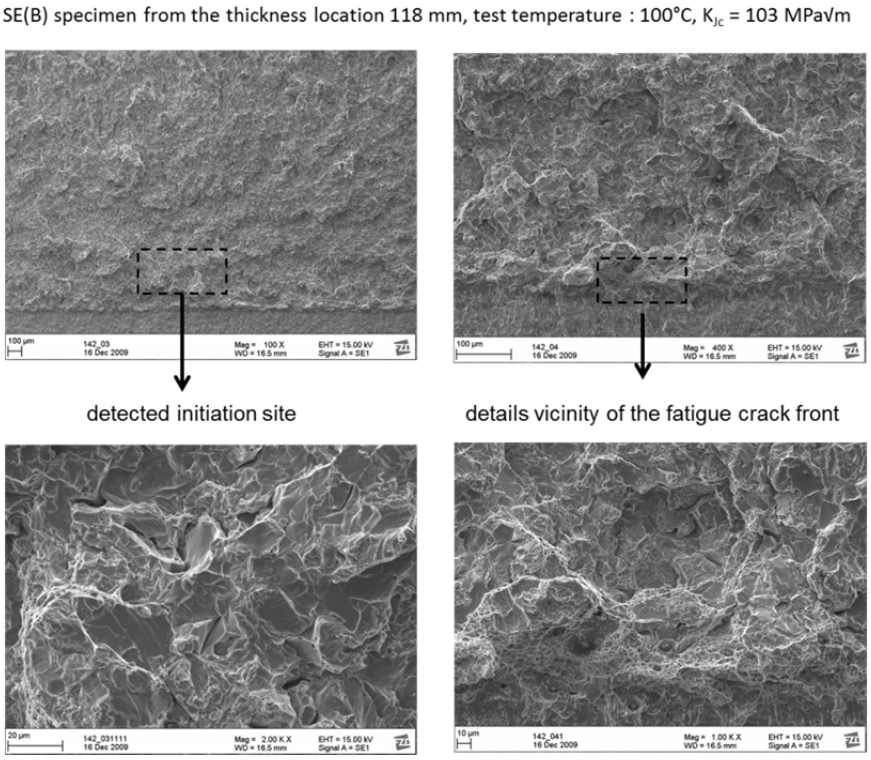

Fig. 43: SEM sections of the fractured surface of a SE(B) specimen from the thickness location 118 mm tested a 100 °C.

As show in Fig. 39 a distinct annealing effect was measured with SE(B) specimens thermally annealed on the laboratory scale. For the filling passes prior to the root, T_0 was determined as -31 °C and beyond the welding root as -7 °C in average. Thus the recovery compared to the average value of the irradiated condition is about 54 K and 86 K, respectively.

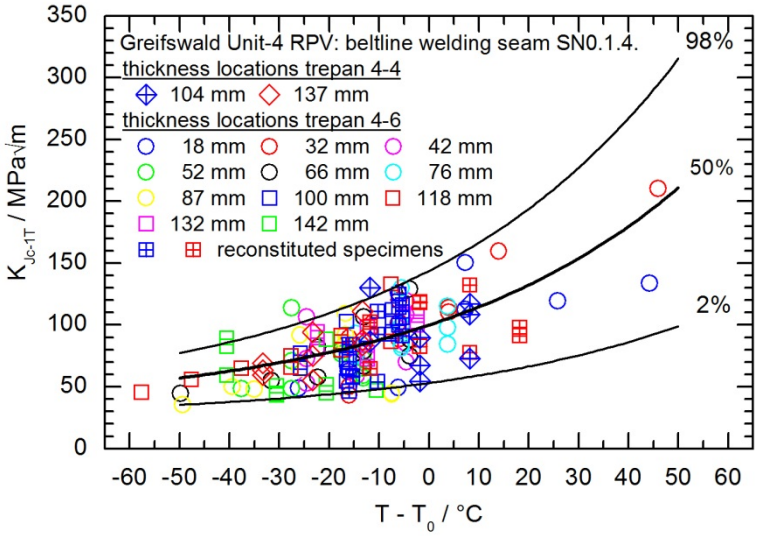

Fig. 44: K_{Jc-1T} values normalised with single-specimen-set T_0 values and MCs of the Unit 4 welding seam SN0.1.4..

Fig. 44 demonstrates the practicality of the MC approach on the WWER-440 weld metal. It summarizes the K_{Jc-1T} values measured on the T-S oriented SE(B) specimens from all thickness locations of the trepans 4-4 and 4-6 versus the test temperature normalised with

single-specimen-set T_0 values. The $K_{Jc\text{-}1T}$ values in general follow the MC-description, although the scatter was large and 11 out of 154 $K_{Jc\text{-}1T}$ values (7.1 %) are not enveloped by the 2 % and 98% tolerance curves, that is about twice as much as expected by the underlying MC concept. As shown in Fig. 41 the progression of T_0 was not significantly influenced by the attenuation of the neutron fluence within the thickness locations where the surveillance specimens for the WWER 440 second generation are sampled. Within this thickness range, a mean T_0 was calculated to be 80 °C. The scatter was rather high which resulted in a standard deviation of approximately 18 K and a span between the highest and lowest T_0 value of 58 K. The $K_{Jc\text{-}1T}$ values measured on SE(B) specimens from these thickness locations were summarized and the evaluated according to ASTM E1921 (Fig. 45, Table A 26). The T_0 was with 74 °C within the standard deviation of the of the single surveillance locations. In general, the $K_{Jc\text{-}1T}$ values followed the temperature-dependence of the MC in which 2 out of 94 $K_{Jc\text{-}1T}$ values (2.1 %) were not enveloped by the MC for 2% fracture probability. It is worth mentioning that the summarized data set includes specimens of test series whose single-evaluation show a span of T_0 values of 58 K (Fig. 41). The majority of K_{Jc} values measured at test temperatures above 80 °C were below the 50% MC. These values originated mostly from the test series with the highest single-evaluation T_0 values (Fig. 41, Table A 20). The VERLIFE reference curve enveloped all $K_{Jc\text{-}1T}$ values. The MM T_0^{MM} value amounted to 82 °C and all $K_{Jc\text{-}1T}$ values lie within the fracture toughness curves for 2 % and 98 % fracture probability. Nevertheless, the MLNH value according to Eq. (9) of the evaluated base metal (Fig. 45) amounted to 4.7 and is consequently assessed to be non-homogeneous.

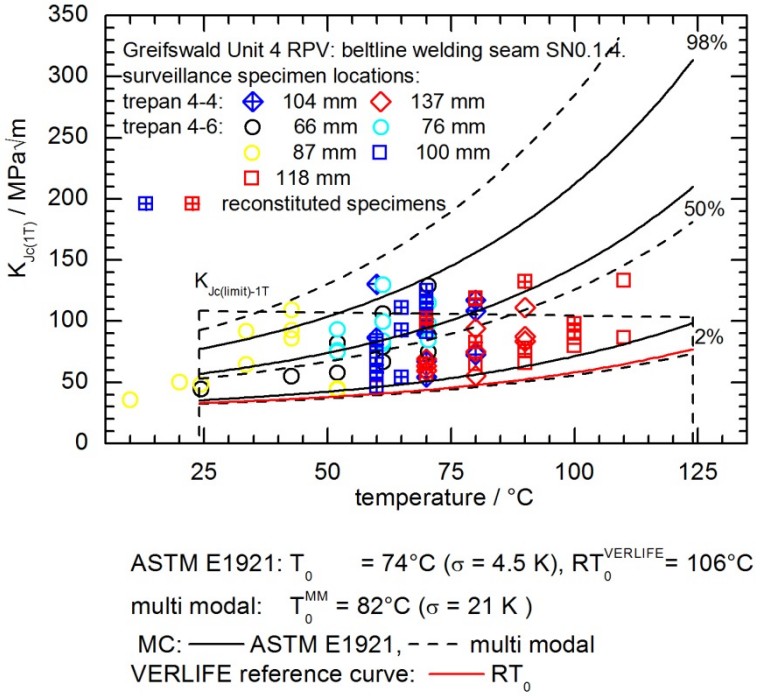

Fig. 45 $K_{Jc\text{-}1T}$ values, standard MCs and MM fracture toughness and VERLIFE reference curves measured with 0.4T-SE(B) specimens sampled from surveillance thickness locations of the Unit 4 beltline welding seam SN0.1.4..

Forged base metal ring 0.3.1.

The detailed progression of the neutron fluence through the thickness of the Unit 4 RPV forged base metal ring 0.3.1. is summarized in Table A 4 (trepan 4-1) and Table A 5 (trepan 4-2).

The hardness HV10 was measured in three lines on the plane TS as schematically depicted in Fig. 46. Fig. 47 shows the progression of the hardness HV10 through the thickness (fluence range from 5.38 to 1.20 · 10^{19}n/cm^2, E > 0.5 MeV) of the Unit 4 forged base metal ring 0.3.1.. The hardness HV10 values measured at the same thickness location scattered with a mean standard deviation of 4 HV10. A strong reduction of the hardness was measured at the thickness location of 18 mm. Afterward the hardness increased again and was then continuously reduced up to about 125 mm thickness. The following increase was within the scatter of the HV10 values between 100 mm and 125 mm thickness.

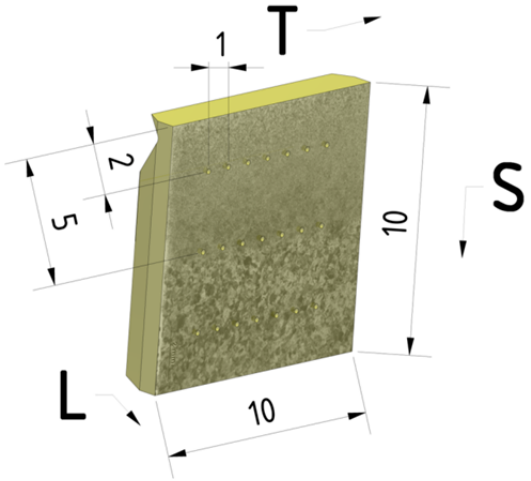

Fig. 46: Example of hardness HV10 measurements beyond the fractured surface of a 0.4T-SE(B) specimen.

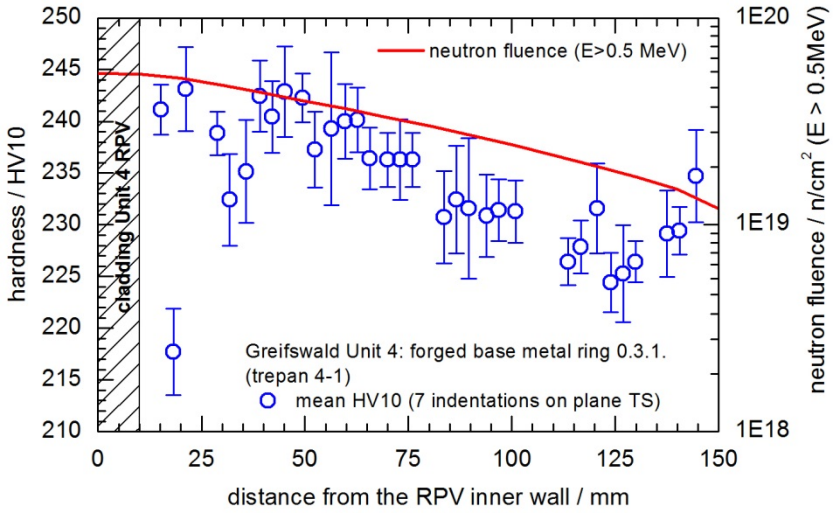

Fig. 47: Progression of the hardness HV10 through the forged base metal ring 0.3.1. of the Greifswald Unit 4 RPV (trepan 4-1).

Beyond the cladding the microstructure was influenced by the heat treatment during the welding of the cladding. Fig. 48 shows micrographs of the plane TS of the 0.4T-SE(B)-specimen from the thickness location 4-1.2 (Table A 24). This specimen is located in a thickness range from about 3 mm to 13 mm beyond the cladding (Fig. 12). The upper micrograph shows the overview of the whole plane TS with hardness HV10 values (mean value and SD of 9 indentations). It demonstrates the influence of microstructure on the hardness in a higher resolution. As shown in the microsections below, there is a fine grained

microstructure on the left side towards the cladding. With increasing distance from the cladding the grains became larger.

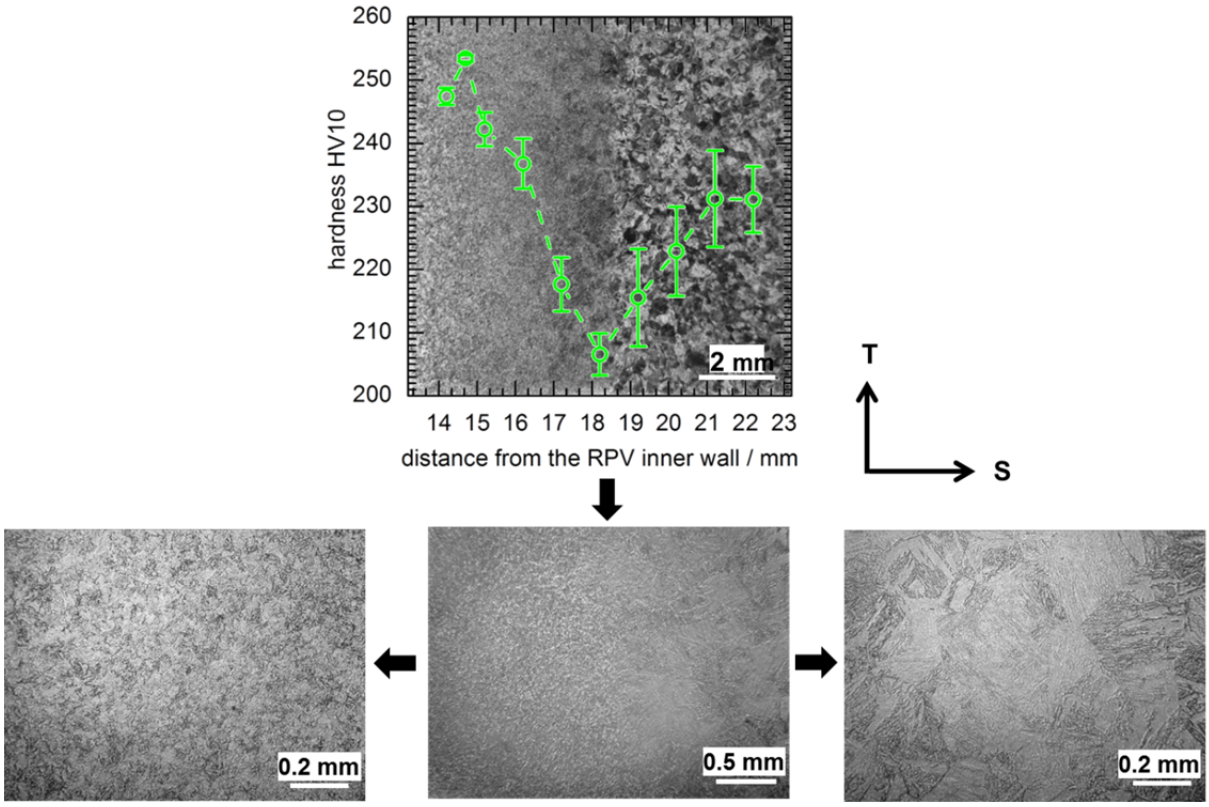

Fig. 48: Metallographic microsections and hardness HV10 values of the plane TS in the thickness range from 13 mm to 23 mm (beyond the cladding) in the forged base metal ring 0.3.1. of the Greifswald Unit 4 RPV.

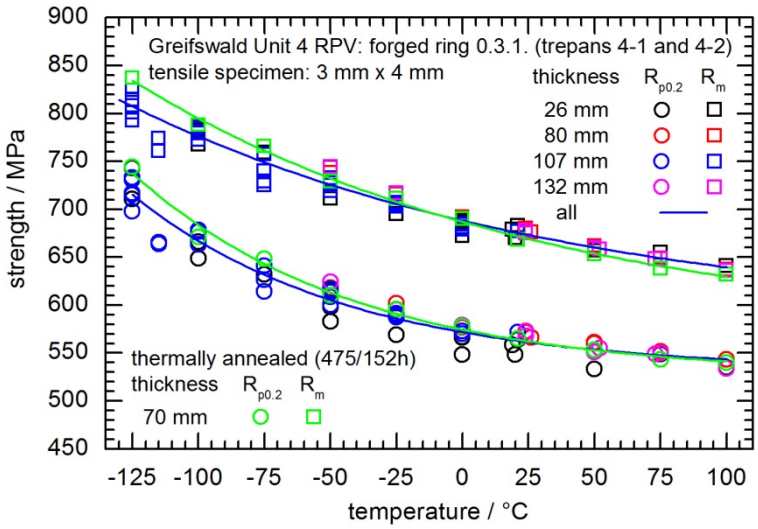

Fig. 49: Tensile strength vs. temperature measured on rectangular tensile specimens from different thickness locations of forged base metal ring 0.3.1. of the Greifswald Unit 4 RPV (trepans 4-1 and 4-2).

Fig. 49 shows the temperature dependence of the yield and ultimate tensile strength through the thickness of the base metal ring. The fitting parameters according to Eq. (6) are summarized in Table A 18. There is no significant change of the yield and ultimate tensile strength with decreasing neutron fluence towards the outer wall of the forged base metal ring

0.3.1. (Fig. 50). As shown in Fig. 49 and Fig. 50 there is no difference in the tensile strength values of the irradiated and additionally laboratory thermally annealed specimens. This indicates no irradiation induced strengthening within the fluence range from 5.38 to 1.20 · 10^{19}n/cm^2 (E > 0.5 MeV).

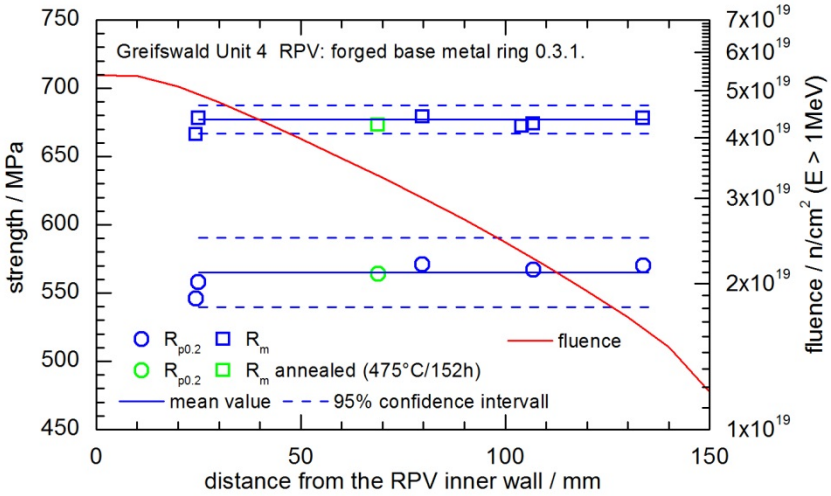

Fig. 50: Progression of the yield and ultimate tensile strength through the thickness of the Unit 4 forged base metal ring 0.3.1. at the position of the maximum neutron flux.

The hyperbolic tangent fit parameter and the TT_{47J} DBTT evaluated on Charpy V-notched specimens from the different thickness locations of the forged base metal ring are summarized in Table A 22.

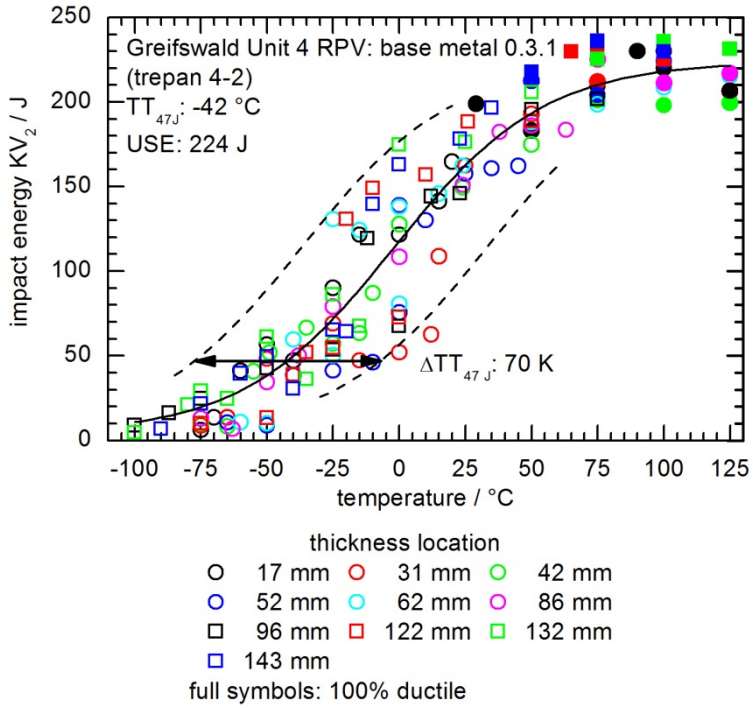

Fig. 51: Impact energy vs. temperature measured on Charpy V-notched specimens from different thickness locations of forged base metal ring 0.3.1. of the Greifswald Unit 4 RPV (trepan 4-2).

Fig. 51 graphically depicts the KV_2 values versus temperature. The KV_2 values strongly scatter and no systematic trend is visible between the different thickness locations. Therefore, the values from the different thickness locations were evaluated together (Table A 22). The hyperbolic tangent fit curve is depicted in Fig. 51. The KV_2 values are mainly within a span of

TT_{47J} ± 35 K. Fig. 52 shows the progression of the reference temperature T_0 and the Charpy-V transition temperature TT_{47J} through the forged base metal ring 0.3.1.. The TT_{47J} values show a slight decreasing trend towards outer wall, which can be neglected taking into account the scatter of the measured KV_2 values. The measured TT_{47J} values are -46 °C and -37 °C at the base metal beyond the cladding and at the RPV outer wall, respectively (Table A 19, Fig. 52).

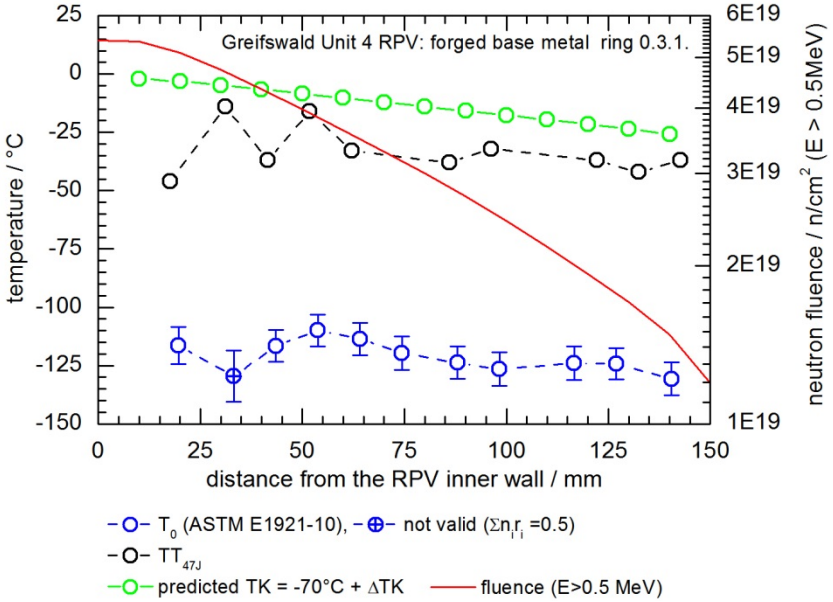

Fig. 52: Progression of the MC reference temperature T_0, the Charpy-V transition temperature TT_{47J} and the predicted T_K through the thickness of the Greifswald Unit 4 forged base metal ring 0.3.1..

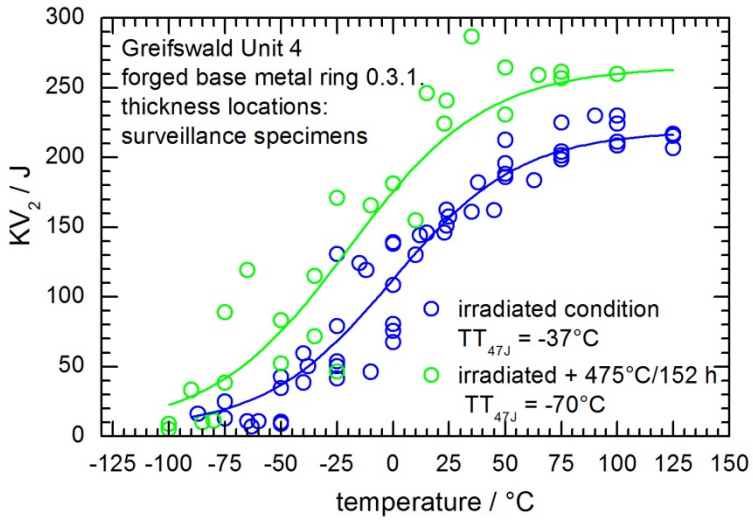

Fig. 53: Common evaluation of the impact energies KV_2 measured on Charpy V-notched specimens sampled from the from WWER-440 generation 2 surveillance thickness locations of the Unit 4 forged base metal ring 0.3.1..

Fig. 53 shows the summarized evaluation of the impact energies KV_2 measured on Charpy V-notched specimens sampled from the WWER-440 second generation surveillance thickness locations. The thermally annealed condition gave a TT_{47J} of -70 °C. Assuming this value as initial T_{K0} the measured irradiation induced shift is 33 K in this thickness range. The predicted T_K shift (ΔT_K) according to the Russian code [PNAEG-1986] of 67 K and 44 K at these locations, respectively, is considerably higher. In the thickness range beyond cladding and towards the outer RPV wall, MC T_0 values between -109 °C and -131 °C were measured

(Table A 24). As shown in Fig. 52 there is a scatter of T_0 within one standard deviation up to about 60 mm wall thickness followed by a continuous decrease by 16 K towards the outer wall. The mean value within the second generation surveillance locations amounts -119 °C with a SD of 6 K.

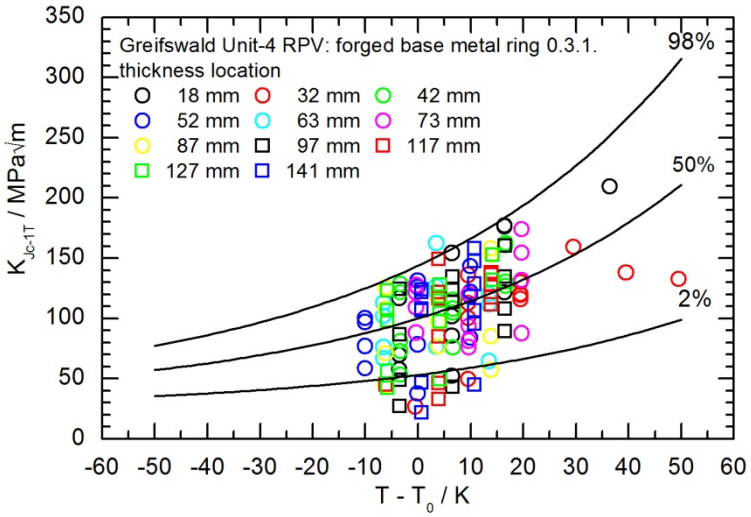

Fig. 54: K_{Jc-1T} values normalised to T_0 of the individual thickness location and MCs of the Unit 4 base metal ring 0.3.1..

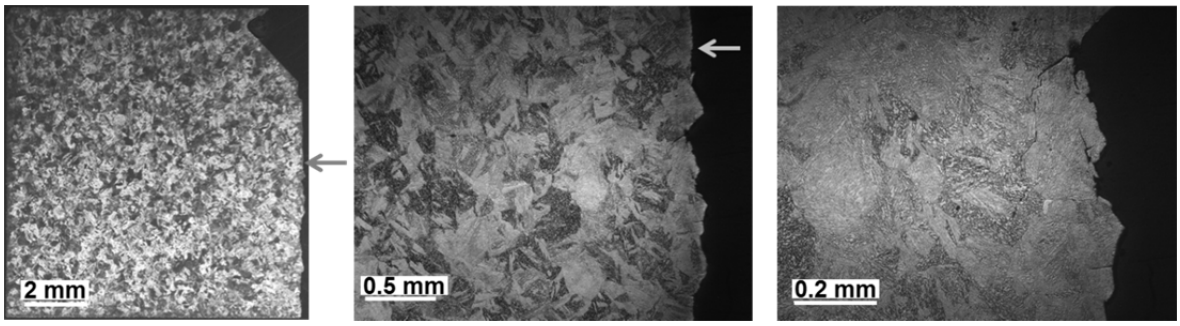

Fig. 55: Metallographic sections of a specimen from the thickness locations 32 mm (T_0 = -130 °C) in the forged base metal ring 0.3.1. of the Greifswald Unit 4 RPV (arrow marks the crack tip).

Fig. 54 shows the K_{Jc-1T} values versus the test temperature normalised with single-specimen-set T_0 values for all thickness locations. This summary shows that the K_{Jc-1T} values strongly scatter, whereby 17 of 131 or 13 % values lie below the fracture toughness curve for 2% fracture probability. Hence, the standard MC evaluation does not accurately describe the measured K_{Jc-1T} values. Some K_{Jc-1T} values were below 27 MPa√m, and in one case a K_{Jc} value of 22 MPa√m was measured. The result is similar to the investigated base metal ring 0.3.1. of the irradiated, thermally annealed and re-irradiated RPV of Greifswald Unit 1 (Fig. 26) and non-commissioned RPV of Greifswald Unit 8 [Viehrig 2006]. The reason for this was the non-homogeneous coarse grain microstructure, which resulted in about 20% intergranular planes in the fractured and fatigue precracked surface. As shown in Fig. 55, such a nonhomogeneous coarse grain ferritic bainitic microstructure is also typical for the investigated base metal ring 0.3.1. of Greifswald Unit 4. The left picture of Fig. 55 shows the microstructure in the vicinity of the crack tip with a large grain just in front of the crack tip. Another observation made during the metallographic examination was the occurrence of interganular cracks along the crack path (right picture of Fig. 55). Fig. 56 depicts SEM

pictures of the crack front from specimens with different K_{Jc} values. A large amount of intergranular planes were observed in both the fatigue crack and the cleavage crack. The initiation site for the cleavage fracture could not be detected in the displayed fractured surfaces.

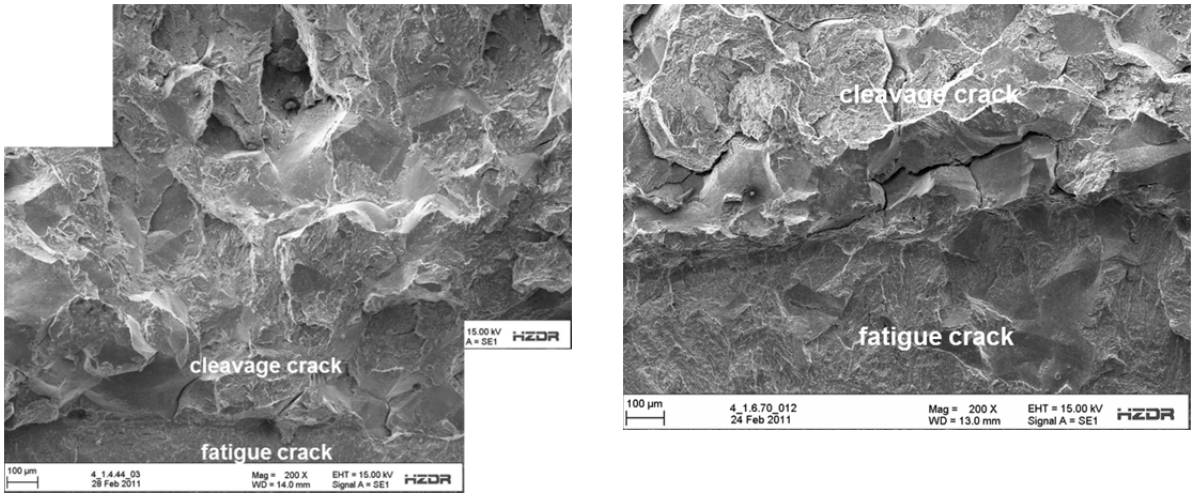

a) b)

Fig. 56: Fractured surfaces of the SE(B) specimens from thickness locations a): 33 mm (T = -130°C, K_{Jc} = 26.8 MPa√m) and b): 54 mm (T = -110°C, K_{Jc} = 160.3 MPa√m).

As depicted in Fig. 52 the decreasing neutron flux towards the RPV outer wall did not have a strong influence on the T_0. Therefore the values of the generation two surveillance thickness locations were summarised to one dataset and the T_0 value was evaluated according to ASTM E1921 to be -120 °C (Fig. 57, Table A 26).

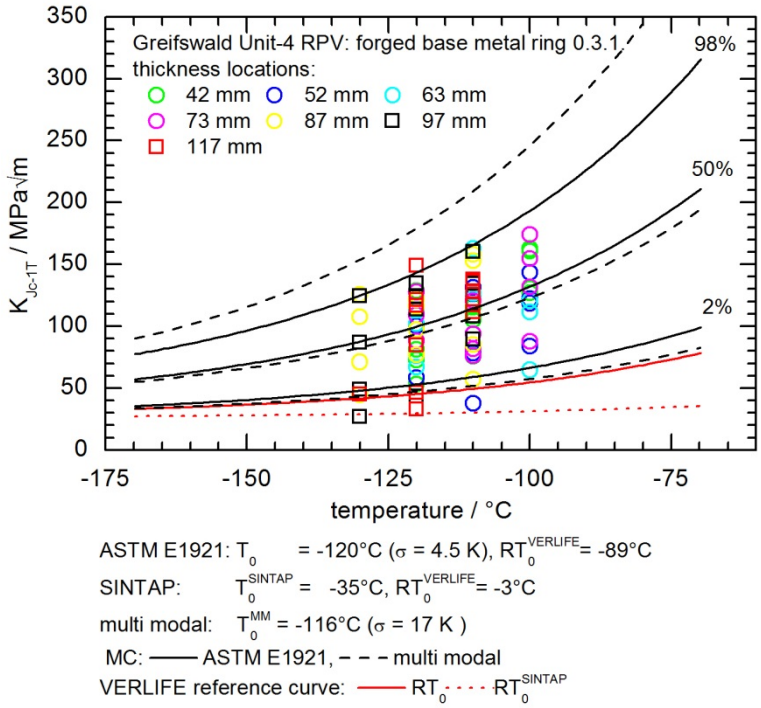

Fig. 57: $K_{Jc\text{-}1T}$ values, standard MCs and MM fracture toughness and VERLIFE reference curves measured with 0.4T-SE(B) specimens sampled from WWER-440 generation 2 surveillance thickness locations of the Unit 4 forged base metal ring 0.3.1..

The MC for 2%, fracture probability does not envelop 9 out of 84 $K_{Jc\text{-}1T}$ values (11 %). As expected from the results of the evaluation of single thickness locations, the standard MC

evaluation of the summarised dataset does not accurately describe the measured $K_{Jc\text{-}1T}$ values. The VERLIFE reference curve indexed with RT_0 and RT_0^{SINTAP} does not envelop 11 (13%) and 1 (1 %) out of 84 $K_{Jc\text{-}1T}$ values. The large number of values also enables the application of the MM approach [Wallin-2004, Viehrig-2006, Scibetta-2010]. Fig. 57 depicts the 2%, 50% and 98% MCs and MM fracture toughness curves. Also the MM approach results in a very low T_0^{MM} value of -116 °C and 5 out of 84 $K_{Jc\text{-}1T}$ values (6 %) are not enveloped by the MM fracture toughness curve for 2% fracture probability. This result shows that even the MM approach does not adequately describe the very low $K_{Jc\text{-}1T}$ values. The MLNH value (Eq. (9)) of the evaluated base metal summarised in Fig. 57 amounts to 3.7 and is consequently assessed to be nonhomogeneous. In the test temperature range from -100 °C to -130 °C K_{Jc} values from 22 MPa√m to 218 MPa√m were measured. For datasets which includes K_{Jc} values below approximately 26 MPa√m the SINTAP-3 approach is not applicable because the $T_0^{SINTAP\text{-}3}$ becomes imaginary [Viehrig-2012b].

The results of the J_R testing according to ASTM E1820 are summarized in Table A 25. Fig. 58 shows the J versus Δa data measured on 0.4T-SE(B) specimens from thickness locations between ¼-T to ¾-T from the forged base metal ring 0.3.1. of the Unit 4 RPV. The mean value J_Q value was 389 kJ/m^2 and the SD 30 kJ/m^2, which is above the maximum J-integral, J_{max}, capacity of the 0.4T-SE(B) specimen of about 310 kJ/m^2 at room temperature. There was a scatter of the interim J_Q values through the thickness of the forged base metal ring (Fig. 59). It suggests inhomogeneity of the base metal 15Kh2MFA. As shown in Fig. 59 the J_Q values determined at -25 °C are comparable to those at room temperature. In contrast to room temperature failed the majority of the specimens tested at -25 °C and below unstable by cleavage fracture after stable crack propagation. At room temperature all specimens showed ductile crack propagation. Therefore, at relevant coolant temperatures the fracture toughness is sufficient also for this nonhomogenous base metal.

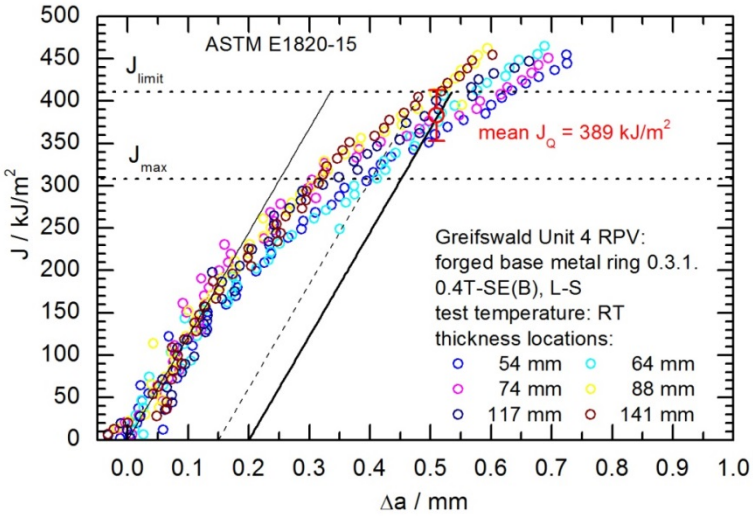

Fig. 58: J vs. Δa data measured on 0.4T-SE(B) specimens from thickness locations between ¼-T to ¾-T from the forged base metal ring 0.3.1. of the Unit 4 RPV (trepan 4-1).

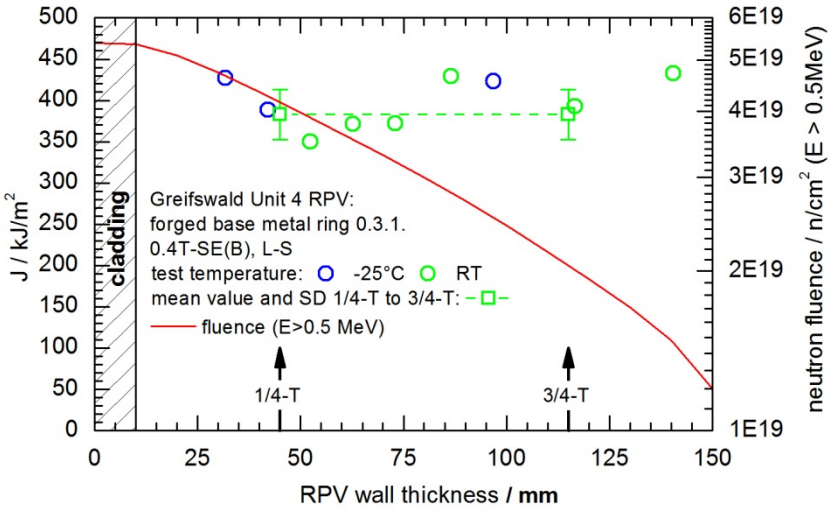

Fig. 59: J_Q values measured with 0.4T-SE(B) specimens sampled through the thickness of the forged base metal ring 0.3.1. of the Greifswald Unit 4 RPV (trepan 4-1).

Overlay cladding

The neutron fluence values of the disc with the overlay cladding of Unit 4 RPV are summarized in Table A 4 (trepan 4-1), Table A 5 (trepan 4-2), Table A 6 (trepan 4-4) and Table A 7 (trepan 4-6).

Table A 27 summarizes the fitting parameter according to Eq. (6) and the strength values calculated at 20 °C and 270 °C of the measured miniature tensile specimens (Fig. 7) from the cladding (layers 1 and 2) of trepans 4-1 and 4-6. Fig. 60 shows the yield and ultimate tensile strength vs. test temperature of the investigated overlay cladding materials. As depicted in Fig. 60 there was a minor difference between both layers, in terms of the development of the yield and ultimate tensile strength over the temperature range. On average the values of the layer 1 lay above layer 2. The yield and ultimate tensile strength values at room temperature (Table A 27) were about 30% higher than the yield strength of 314 MPa and ultimate tensile strength of 490 MPa for the initial condition of the WWER-440 overlay cladding as reported in [Timofeev-2006].

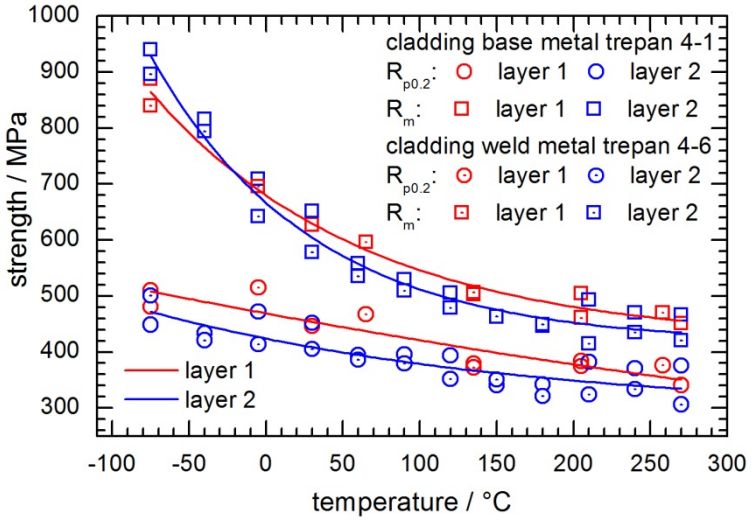

Fig. 60: Tensile strength characteristics of the cladding layers 1 and 2 vs. temperature.

Eq. (10) describes the modulus of elasticity vs. temperature provided for the WWER cladding [Margolin-2010] (Fig. 61). For comparison, Fig. 61 also depicts the effective modulus of

elasticity measured by unloading compliance based on the measured initial crack lengths, a_0, of the tested specimens (Table A 28 und Table A 29). The effective modulus of elasticity strongly scattered and showed almost no temperature dependency (Eq. 11). It deviates from the general progression provided by [Margolin-2010].

$$E(T) = 188.3 - 0.045 \cdot T - 3.2 \cdot 10^{-5} \cdot T^2 \text{ [RT till 300 °C]} \quad (10)$$

$$E_{eff}(T) = 195.8 + 0.0012 \cdot T \quad (11)$$

The Modulus of elasticity according to Eq. (10) was used for the fracture toughness evaluation according to ASTM E1820.

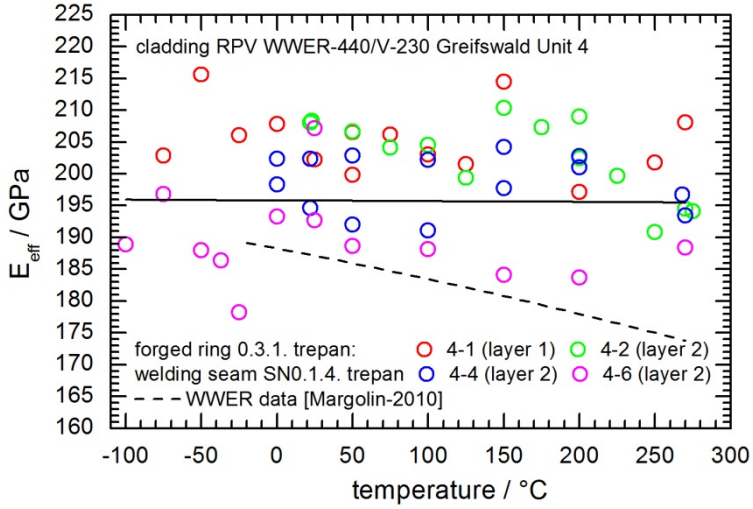

Fig. 61: E-modulus vs. temperature provided for the WWER overlay cladding [Margolin-2010] and the effective E-modulus measured by the unloading compliance.

Table A 28 and Table A 29 summarize the interim initiation J integral values, J_Q, and the equivalent fracture toughness values, K_{JQ}, evaluated according ASTM E1820 of the investigated overlay cladding materials. The majority of the tests yielded interim J_Q values because of not fulfilled validity criteria according to ASTM E1820. Fig. 62 and Fig. 63 depict the interim J_Q values vs. temperature. Generally, the scatter of the J_Q values was large, which was caused by the crack moving through the heterogeneous microstructure of the overlay cladding. Furthermore, the J-Δa data determined from the first partial unloading sequences tend to scatter, which had an impact on the evaluated crack initiation J_Q values. Both figures show that the J_Q values increased with temperature to a maximum at about ambient temperature and decreased again towards higher temperatures. The trend of the J_Q vs. temperature values has been approximated to a linear fit from ambient temperature till the inlet water temperature of 270 °C. Above ambient temperature the fracture toughness values, J_Q, were > 60 kJ/m^2. Such progression of the initiation fracture toughness is also reported in the literature [Haggag et al.-1990, Margolin-2010, Timofeev-2006]. The specimens from the cladding of trepans 4-1 and 4-6 fail unstably at -75 °C and -100 °C, respectively. At higher test temperatures some specimens showed crack jumps or unstable failure after ductile crack extension within the 0.15 mm and 1.5 mm exclusion lines. In this case only data up to the crack jumps were used to fit the power law regression curve according to ASTM E1820. In the summary, two fracture mechanisms were observed:

- transcrystalline ductile fracture and
- intercrystalline fracture.

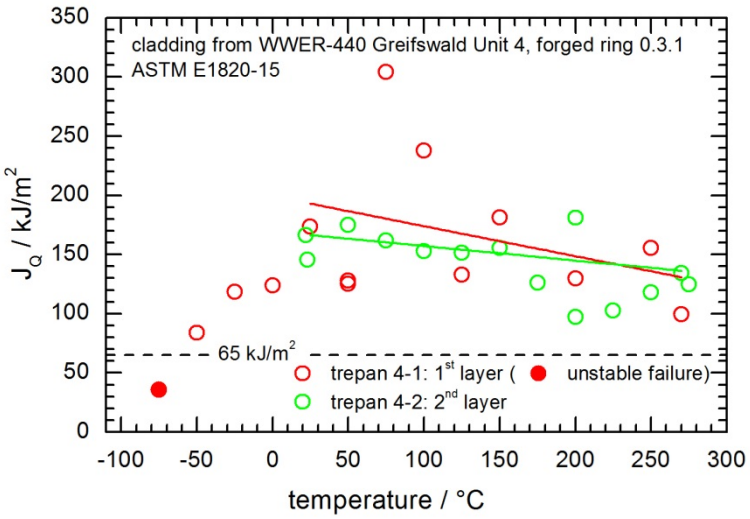

Fig. 62: Crack initiation fracture toughness values, J_Q, vs. temperature of the investigated cladding from the forged base metal ring 0.3.1. of the Greifswald Unit 4 RPV.

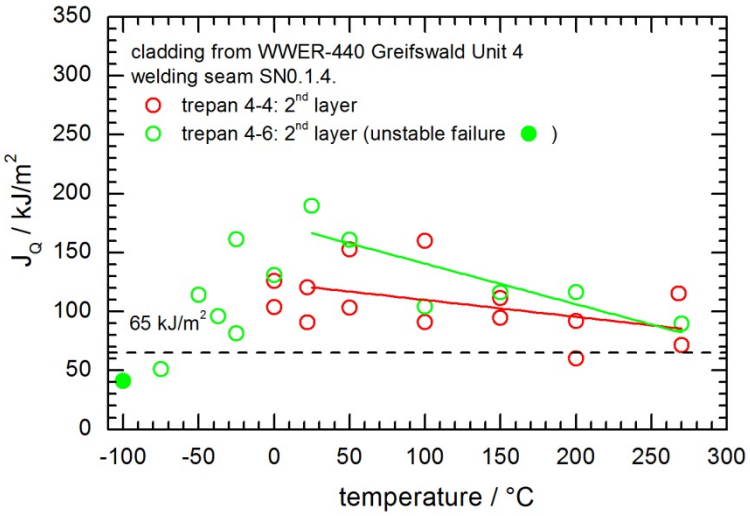

Fig. 63: Crack initiation fracture toughness values, J_Q, vs. temperature of the investigated overlay cladding from the welding seam SN0.1.4. of the Greifswald Unit 4 RPV.

Temperatures below 0 °C have no meaning for the RPV operation and PTS transients. Below -50°C specimens failed unstable. An example is the specimen 4-6.1.8 (Table A 29) tested at -100 °C. The specimen failed unstable by intercrystalline fracture as shown in Fig. 64. The increasing fracture toughness towards ambient temperature shown in Fig. 62 and Fig. 63 is the result of the reducing intercrystalline fracture and the decline above ambient temperature is caused by the decreasing yield strength (Fig. 60).

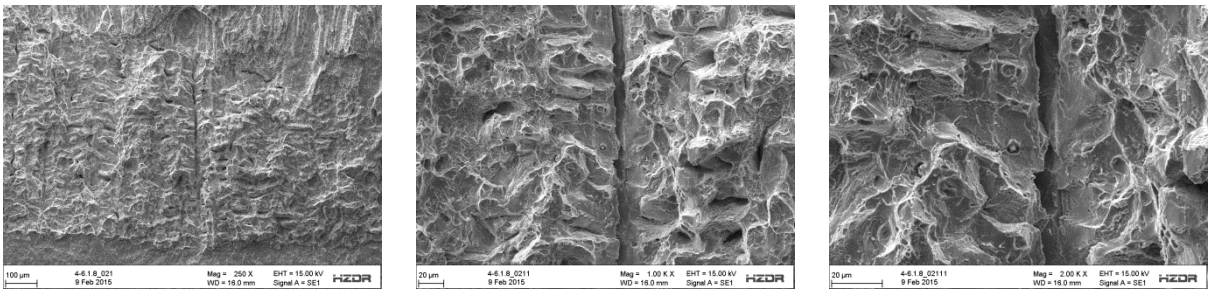

Fig. 64: SEM images of fractured surface the SE(B) specimen 4-6.1.8 (2nd layer of the cladding from the beltline welding seam SN0.1.4.) tested at -100 °C.

The location of the crack tip and the scatter of the J-Δa data are very important in terms of the evaluation of the initiation values J_Q according to ASTM E1820. The J-Δa data of many specimens exhibit an unsteady trend caused by the crack propagation through different microstructures (Fig. 12). Slight differences in the progression of the J-Δa data within the range of the J_R curve fit (between the 0.15 mm and 1.5 mm exclusion lines) can cause a large difference of the evaluated J_Q values. As an example Fig. 65 shows the load - LLD (a) and J - Δa (b) diagrams measured on the 0.4T-SE(B) specimen 4-6.1.12 (Table A 29) from the 2nd cladding layer of the welding seam SN0.1.4. (trepan 4-6). The specimen was tested according to ASTM E1820 at room temperature. As shown in Fig. 65a, there is discontinuity in the load - LLD progression. At about 1.1 mm LLD the decline of the load - LLD data became flatter and the slope of the unloading sequences was changed which resulted in a change of the slope of the J - Δa data. The steeper load decline from about 1.7 mm LLD and the shallow slope of the unloading sequences resulted in horizontal crack propagation (Fig. 65b). The J_R curve was evaluated with the data from the 0.15 mm Exclusion Line till J_{max}.

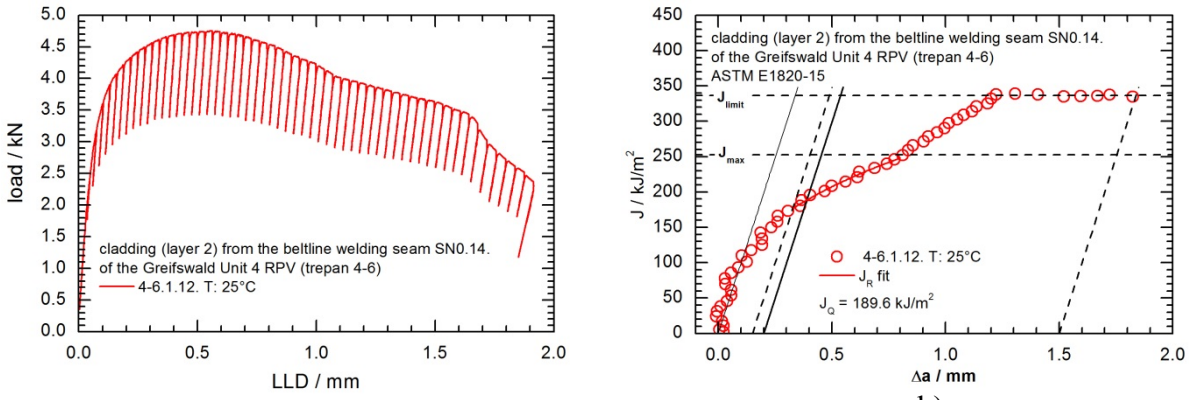

a) b)

Fig. 65: Load vs. load line deflection (a) and J vs. Δa (b) diagrams measured on the 0.4T-SE(B) specimen 4-6.1.12 (Table A 29) from the 2nd layer of cladding of the welding seam SN0.1.4. (trepan 4-6).

Examples of the fracture appearance are shown below. In general, the transcrystalline ductile fracture appeared as dimple fracture, whose size and shape was influenced by the microstructure of the cladding and the test temperature. Fig. 66 shows the SEM images of the SE(B) specimen 4-6.1.12. The overview of the fractured surface is shown in the upper left picture, where the range of the realised crack extension is marked. The dimples in the vicinity of the fatigue crack front change their shape and size. Close to the fatigue crack front up to about 1.2 mm crack extension, large dimples are visible (Fig. 66 detail 1), when J - Δa values reach the flat region of the graph as depicted in Fig. 65b. The diameter of dimple in the area of low tearing strength is smaller compared to that in the area of high tearing strength (details 2 and 3).

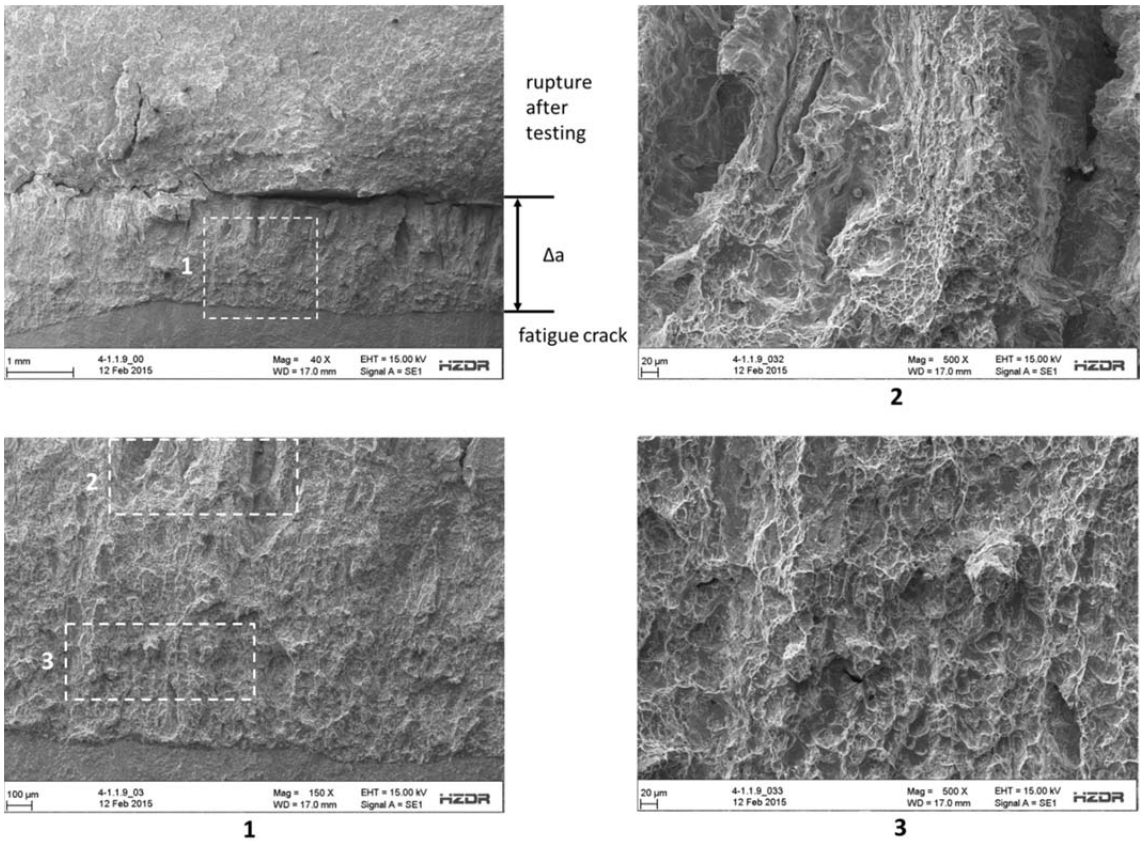

Fig. 66: SEM images of fractured surface the SE(B) specimen 4-6.1.9 (2nd layer of the cladding from the beltline welding seam SN0.1.4.) tested at 25 °C.

Larger crack jumps which are indicated as load drops in the load vs. COD diagram were visible for the cladding of the trepan 4-1 from the forged ring 0.3.1.. The neutron fluence accumulated by the overlay cladding of this trepan was about 30% higher than that of the trepans from the welding seam SN0.1.4. (Table 7). Furthermore the crack tip of the SE(B) specimens was located in the first layer of the cladding (Fig. 12). As shown in Fig. 62, the J_Q vs. temperature progression was in principle comparable to the overlay cladding from the weld metal trepans. However, this overlay cladding showed crack jumps during the loading above room temperature. In some cases strong load drops, caused by crack jumps, initiated the end of test criteria and finished the test after the following UC sequence. Fig. 67 shows the load - LLD and J - Δa diagrams of specimens tested at 50 °C and 75 °C. The load drops connected with the crack jumps were clearly visible in the load - LLD diagrams. The load values of specimen 4-1.1.9 tested at 50 °C (Table 9) reached the maximum at about 0.4 mm LLD and decreased afterwards interrupted by a load drops between 1.20 mm and 1.35 mm LLD followed by further loading. The load values of specimen 4-1.1.10 tested at 75 °C (Table 9) reached the maximum at about 0.8 mm LLD and decreased more gently up to a strong load drop at about 1.6 mm LLD. At that load drop, the loading of the specimen was automatically stopped after the subsequent UC sequence as a predetermined end of test criteria (50% load drop) was exceeded. These load vs. LLD progressions were also reflected in the J - Δa data. The J - Δa progression of the specimen 4-1.1.9 was shallower than that of specimen 4-1.1.10. The small load drop of specimen 4-1.1.9 caused a discontinuity in the J - Δa progression at about 1.1 mm Δa, while the specimen 4-1.1.10 failed at 0.8 mm Δa. With both specimens interim J_Q values were evaluated according to ASTM E1820.

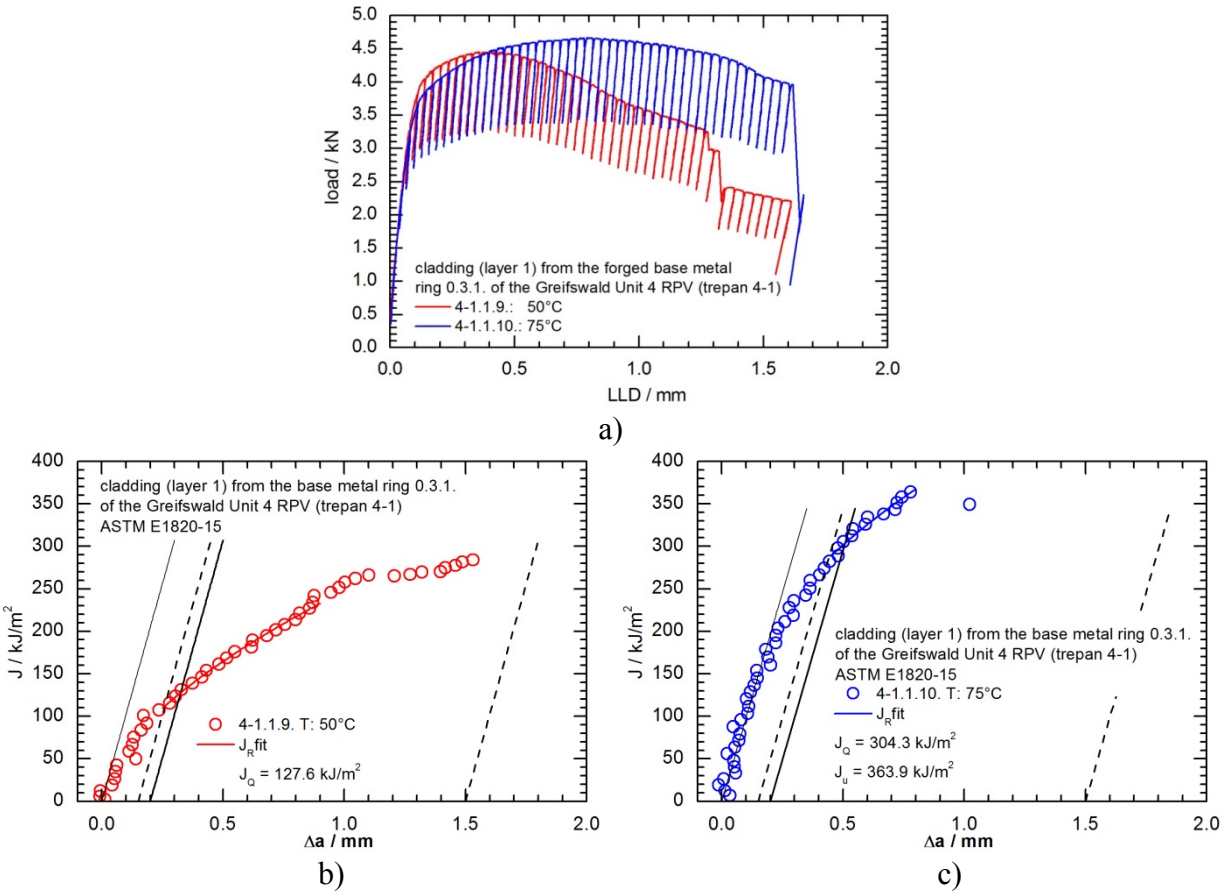

Fig. 67: Load vs. load line deflection (a) and J vs Δa diagrams measured on 0.4T-SE(B) specimens 4-1.1.9 (b) and 4-1.1.10 (c) from the 1st layer of cladding of the forged ring 0.3.1. (trepan 4-1).

Fig. 68 shows the SEM images of the SE(B) specimen 4-1.1.9 tested at 50 °C. As mentioned above, the load drop shown in Fig. 67a) and the discontinuity in the J-Δa progression at about 1.1 mm crack propagation (Fig. 67b) resulting from it was also reflected in the SEM images. The transition of the tearing is visible in region marked as detail 1. The details 2 and 3 show the fracture appearances before and after the load drop, respectively. Both details show ductile tearing, but the dimples of detail 3 are larger compared with that in detail 2. In addition, detail 2 shows elongated tears.

Fig. 69 shows SEM images of the transition between ductile tearing and unstable rupture of SE(B) specimen 4-1.1.10 (Table A 28). The two fracture modes: ductile tearing and unstable rupture (Fig. 67a and c) are clearly visible as dimples and intergranular bumpy planes, respectively.

As another example J_R curves of the specimens tested at 200 °C are summarized in Fig. 70. This figure poses again the problem with the J_R testing of overlay cladding material. The first J-Δa values measured with the first UC sequences scattered which was caused by the low precision compliance measurement. In addition, the tearing strength of the inhomogenous cladding microstructure varied within the range of the crack propagation. Both had an impact on the evaluated J_Q values, which varied from 60 kJ/m^2 to 181 kJ/m^2. In the operation and emergency temperature range of the RPV, the low J_Q value of 60 kJ/m^2 and its equivalent K_{JQ} value of 99 MPa√m of specimen 4-4.4.5. might represent a lower shelf value caused by the low tearing strength of the overlay cladding in the vicinity of the crack tip [Margolin-2010].

As shown in Fig. 62 and Fig. 63, low J_Q values were determined on specimens tested at 270 °C, which is about the inlet water temperature of the WWER-440 reactors. At this test temperature the span of the J_Q and K_{JQ} values reached from 89 kJ/m^2 to 134 kJ/m^2 and 119 MPa√m to 146 MPa√m, respectively (see Table A 28 and Table A 29), in which the lower values were measured on the specimens from the overlay cladding of the welding seam SN0.1.4. (trepans 4-4 and 4-6).

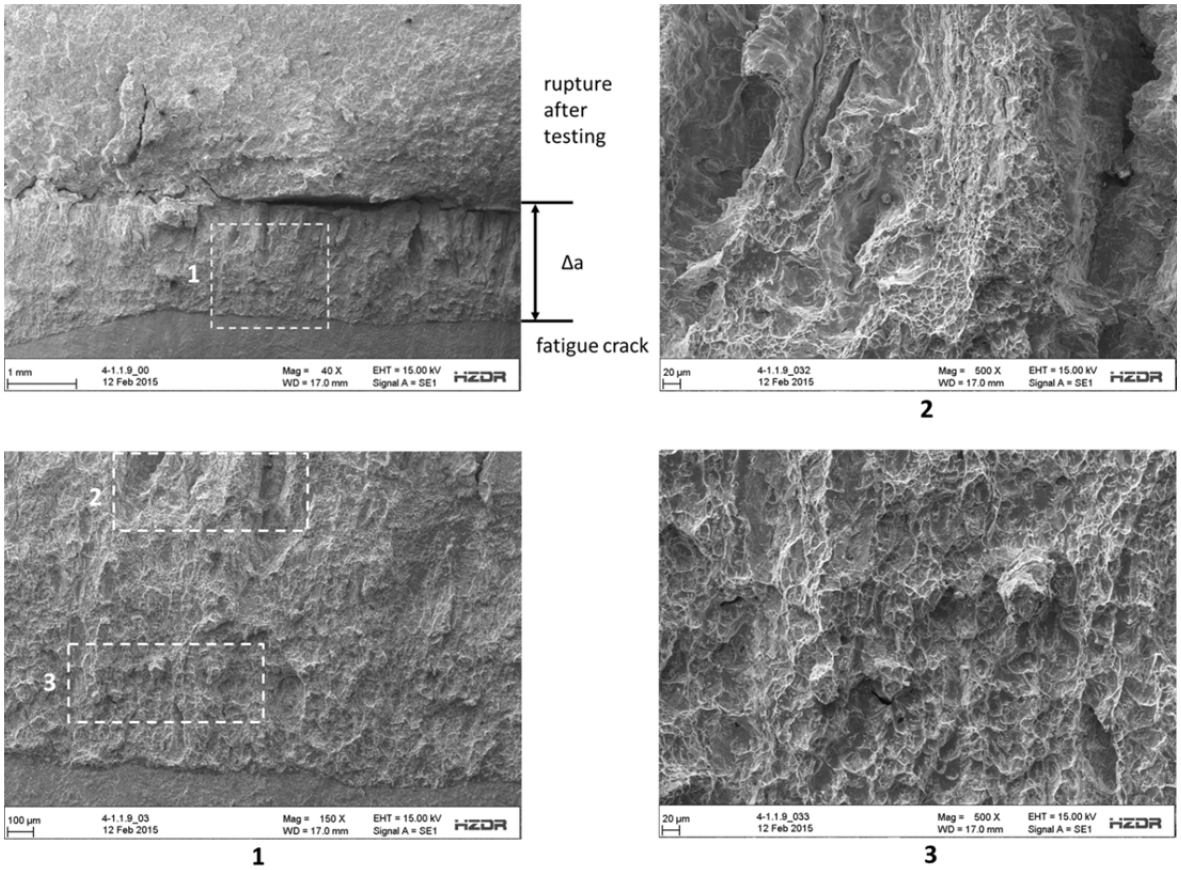

Fig. 68: SEM images of fractured surface the SE(B) specimen 4-1.1.9 (layer 1 of the cladding from the forged ring 0.3.1.) tested at 50 °C.

The integrity of the overlay cladding during a PTS scenario was assessed by a conservative estimation of the stress intensity factor (SIF) that could occur at a flaw [Viehrig-2015a]. The leading scenario for the WWER-440 is described by a stuck open pressurizer relief valve (which initiates the emergency core cooling system) followed by an inadvertent re-closure after one hour [Pistora-2003]. In [Abendroth-2007] and [Viehrig-2012a] fracture mechanics analyses of the RPV wall based on this scenario were performed. It was shown that the equivalent stress in the cladding, resulting from tension in axial and hoop direction, reaches the yield strength during the cold water injection. This is due to the larger thermal expansion coefficient of the cladding material compared to the ferritic RPV material.

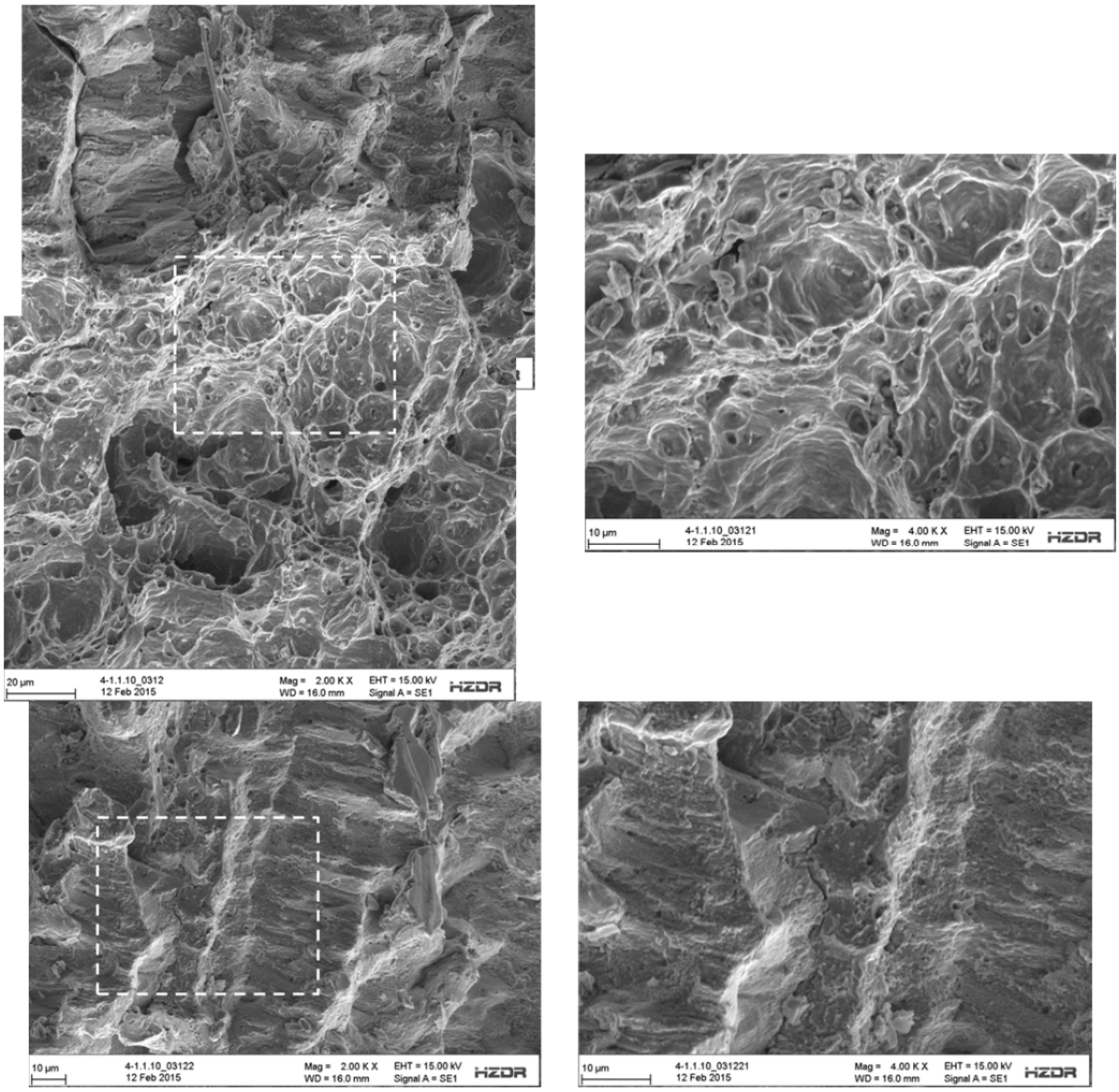

Fig. 69: SEM images of the transition between ductile tearing and unstable rupture of SE(B) specimen 4-1.1.10 (Fig. 67) tested at 75 °C.

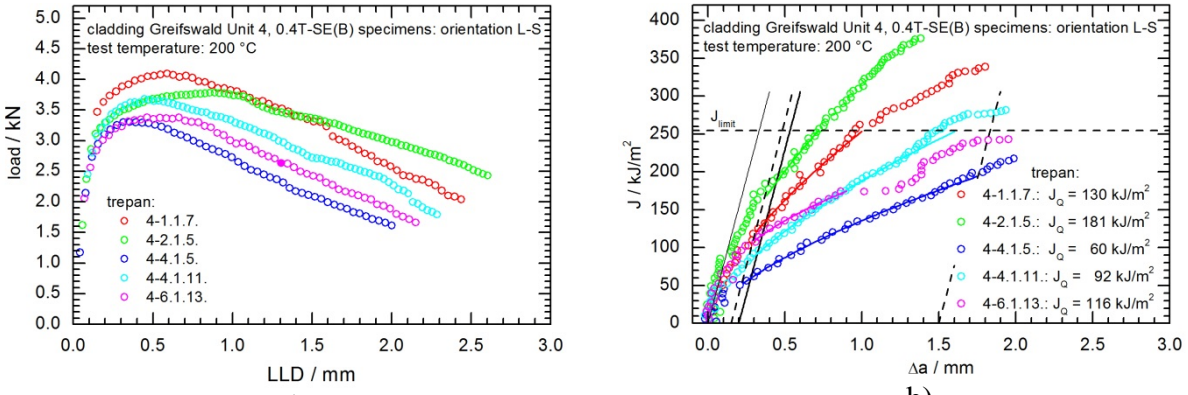

Fig. 70: Load vs. load line deflection (a) and J vs Δa diagrams measured on 0.4T-SE(B) specimens from the trepans: 4-1, 4-2, 4-4 and 4-6 tested at 200 °C.

Therefore we assumed the following conditions for the estimation of the SIF:

- uniform temperature in the cladding: T = 60 °C
- uniform hoop stress in the cladding: σ = 408 MPa (corresponds to the yield strength of the cladding at T = 60 °C)
- axially oriented semi-elliptical surface crack in the cladding with an aspect ratio a/c = 0.3

Two analytical formulae are used to calculate the SIF. The first one is according to the VERLIFE code [VERLIFE-2015]:

$$K_I = \sigma \cdot \sqrt{a} \cdot \frac{2 - 0.82 \cdot a/c}{\left[1 - \left(0.89 - 0.57\sqrt{a/c}\right)^3 \cdot (a/s)^{3/2}\right]^{3.25}} \quad (12)$$

and the second one according to a work of Dufresne [Dufresne-1981]:

$$K_I = \sigma \cdot \sqrt{\pi a} \cdot \left[1.14 - 0.48 \cdot \frac{a}{c} + \frac{(a/s)^2}{0.2 + 4.9 \cdot (a/c)^{1.2}}\right]. \quad (13)$$

Both equations are based on fits of FEM simulation results and calculate the SIF at the deepest point of the semi-elliptical crack. The SIFs calculated for different a/s ratios are listed in Table 11.

Table 11: SIFs in dependence on a/s calculated according to VERLIFE [VERLIFE-2015] and Dufresne [Dufresne-1981].

a/s	K_I^* MPa√m	K_I^{**} MPa√m
0.2	33.9	33.2
0.5	63.7	60.4
0.8	103.7	95.0

* according to VERLIFE [VERLIFE-2015]

** according to [Dufresne 1981]

The formula according to the VERLIFE code [VERLIFE-2015] is more conservative. Even in the case of the deep crack (a/s = 0.8), the estimated SIF is well below the K_{JQ} values measured in the temperature range of the PTS scenario (Table A 28 and Table A 29). Hence, it can be stated that the investigated Greifswald Unit 4 RPV overly cladding containing a flaw would not have failed during a PTS event.

Small-Angle Neutron Scattering Investigations

Small-angle neutron scattering (SANS) is capable to detect and characterize the nanometre-scale defects responsible for irradiation-induced property changes [Carter-2001]. In particular, reliable and robust estimates of the size distribution of these defects averaged over macroscopic volumes of some 10 mm^3 can be obtained. It is important to notice that the interpretation of SANS data depends on the availability of a good reference material. Usually, the unirradiated condition of the same material serves as a reference. However, the unirradiated conditions are not available for the Greifswald RPVs. Therefore, the SANS investigation is embedded in a previous study of surveillance material of the same kind, WWER-440-type in the unirradiated, as-irradiated, post-irradiation annealed and reirradiated conditions [Ulbricht-2007, -2011].

Experiments

Discs of dimensions 10 mm · 10 mm · 1 mm were cut from broken halves of 0.4T-SE(B) specimens at about 10 mm distance from the fracture surface to exclude any influence of plastic deformation. These discs were used in order to perform both SANS experiments and Vickers hardness tests subsequently. The investigated RPV base and weld metals from the Greifswald units are summarized in Table 12.

Table 12: Materials investigated by SANS.

unit	RPV material	thickness location	specimen	condition (Table 1)	neutron fluence
1	welding seam SN0.1.4	8 mm	1-1.1.1.	IAI	Table A 1
2	welding seam SN0.1.4	8 mm	2-3.1.2.	IA	Table A 3
4	welding seam SN0.1.4	32 mm	4-6.4.40	I	Table A 7
		32 mm	4-6.4.40	IA*	
		52 mm	4-6.6.60	I*	
		52 mm	4-6.6.60	IA*	
		86 mm	4-6.10.96	I*	
		86 mm	4-6.10.96	IA*	
		118 mm	4-6.14.134	I*	
		118 mm	4-6.14.134	IA*	
		132 mm	4-6.16.156	I*	
		132 mm	4-6.16.156	IA*	
4	forged base metal ring 0.1.3.	32 mm	4-1.4.39.	I	Table A 4
		32 mm	4-1.4.39.	IA*	

* second half of the 0.4T-SE(B) specimen was laboratory scale thermally annealed at 475°C/152 h

The SANS measurements were performed at the instrument V4 of HZB Neutrons Berlin [Keiderling-1995]. The wavelength of the neutron beam was 0.6 nm. In order to separate nuclear and magnetic scattering contributions, a magnetic field of 1.4 T was applied to the samples perpendicular to the neutron beam direction during the measurements. More details on the experimental setup are given in [Ulbricht-2007]. The software package BerSANS-PC [Keiderling-2002] was used for raw-data treatment including corrections, absolute calibration and separation of the magnetic contribution from the total intensities. Transformation into the cluster size domain was performed starting from the difference scattering curves with the post-irradiation annealed condition as reference. Further analysis is based on the indirect transformation method [Glatter-1980] and provides the size distribution of scatterers without assuming a certain type of distribution. The A-ratio, defined as the ratio of the scattering cross- section perpendicular and parallel to the magnetic field direction [Beaven-1986] was calculated. Insight into the nature of scatterers can be derived from the A-ratio.

Results

Finding of a reference material condition

The magnetic scattering cross-sections measured for the as-received unirradiated conditions of the three representative type Sv-10 KhMFT weld metals (I, II, III) [Ulbricht-2011] are plotted in Fig. 71 as a function of the scattering vector, Q. These scattering cross-sections form a scatter band as indicated by the solid lines. As there is no model for the scattering

curves of steels, the scatter band was constructed empirically so as to cover 95% of the measured data points. The scatter band serves as reference for the irradiated and annealed conditions. The measured SANS curves of the post-irradiation laboratory annealed conditions (specimens 4-6.4.40. and 4-6.6.60.) from the beltline welding seam SN0.1.4. of the Unit 4 RPV (Table 12), are completely within the scatter band (Fig. 72). Thus, the laboratory annealing of material from Unit 4 can be used as a reference for the non-existing unirradiated condition.

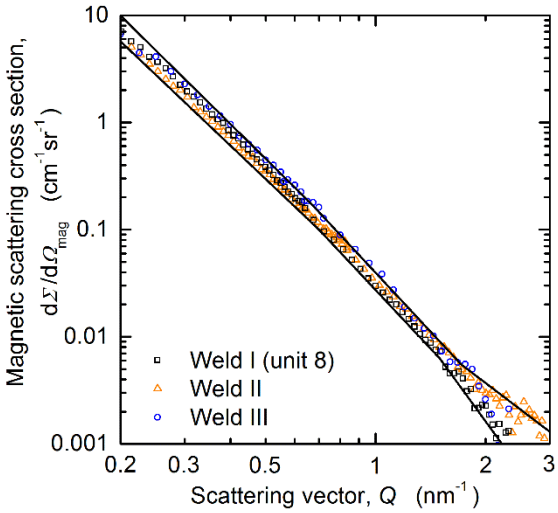

Fig. 71: Magnetic scattering cross-sections of the unirradiated condition of three type Sv-10 KhMFT weld metals. The solid lines indicate the scatter band.

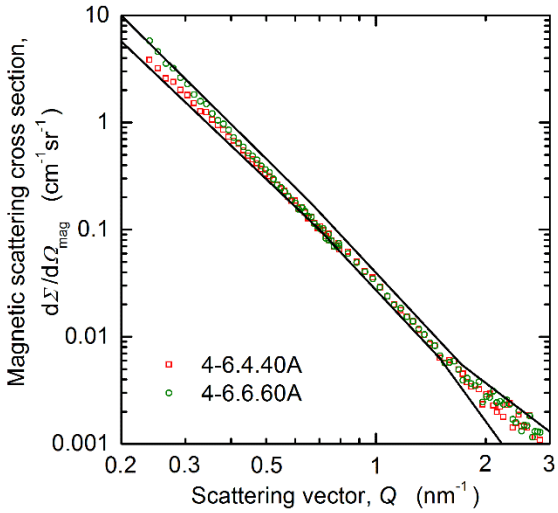

Fig. 72: Magnetic scattering cross-section of the post-irradiation laboratory annealed conditions of Unit 4 welds (4-6.4.40, 4-6.6-60, Table 12). The solid lines indicate the scatter band of the unirradiated conditions (see Fig. 71).

As-irradiated conditions

An irradiation-induced increase of the SANS cross-sections at high values of Q is clearly visible for all investigated as-irradiated conditions of Unit 4 RPV. Fig. 73 and Fig. 74 illustrate this fact for the magnetic and nuclear SANS intensities of the sample 4-6.4.40 (Table 12), respectively. The constant incoherent nuclear scattering contribution (Fig. 74), mainly caused by the different iron isotopes in the matrix, limits the resolution of the SANS measurements.

The complete set of measured magnetic difference scattering cross-sections for the different layers of the Unit 4 weld metals with the respective post-irradiation annealed condition taken as reference are shown in Fig. 75. The fitted curves which are depicted in Fig. 76 are used in order to reconstruct the size distributions. The total volume fraction, number density, average radius and A-ratio of the irradiation-induced clusters are summarized in Table 13.

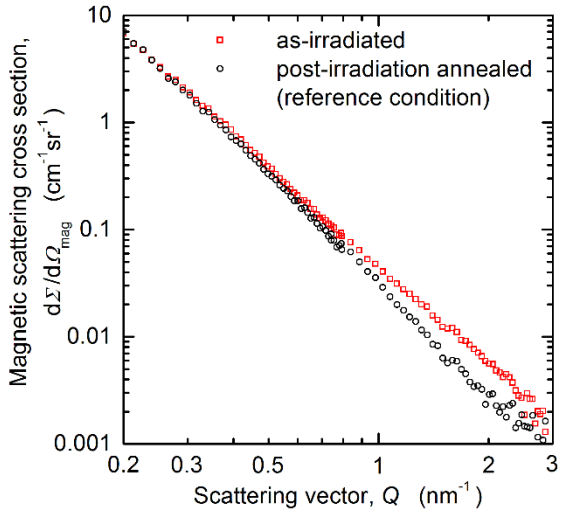

Fig. 73: Magnetic scattering cross-sections of weld 4-6.4.40 of the as-irradiated and of the post-irradiation annealed condition (Table 12).

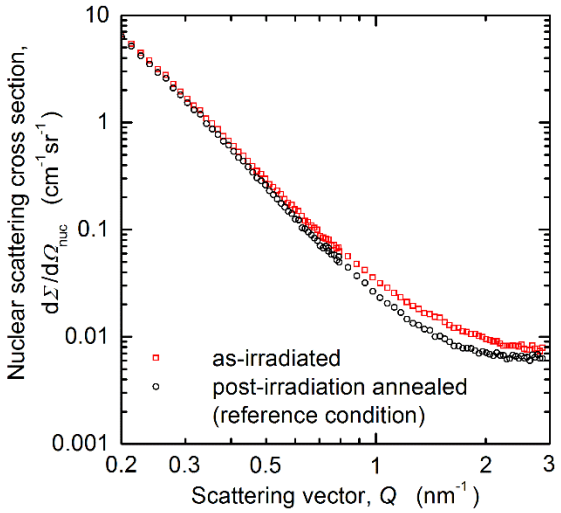

Fig. 74: Nuclear scattering cross-section of weld 4-6.4.40 of the as-irradiated and of the post-irradiation annealed condition (Table 12).

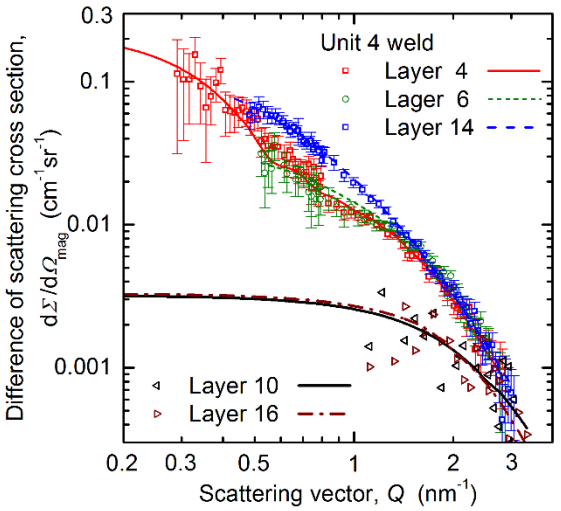

Fig. 75: Measured magnetic difference scattering curves with the post-irradiated annealed condition as reference for different layers of the welding seam of Unit 4 RPV.

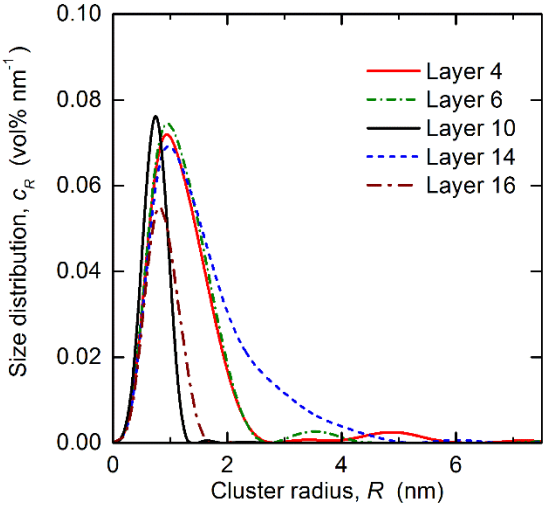

Fig. 76: Size distribution of irradiation-induced clusters for different layers of the welding seam of Unit 4 RPV.

Table 13: Volume fraction, c, number density N, mean radius and A-ratio of irradiation induced clusters obtained by SANS and measured Vickers hardness, HV10, of the same samples.

Layer	Fluence in 10^{19} cm^{-2}	c in vol%	N in 10^{16} cm^{-3}	R_{mean} in nm	A-ratio	HV10
4-6.4.40 4-6.4.40IA	2.3	0.102 ± 0.01 -	21 ± 6 -	0.87 -	2.2 ± 0.1 -	243 ± 3 204 ± 3
4-6.6.60	1.7	0.099 ± 0.01	22 ± 6	0.87	2.1 ± 0.01	245 ± 4
4-6.10.96	0.98	0.042 ± 0.005	21 ± 4	0.71	2.0 ± 0.01	226 ± 3
4-6.14.134	0.6	0.118 ± 0.01	20 ± 5	0.91	2.2 ± 0.01	234 ± 6
4-6.16.156	0.49	0.038 ± 0.005	16 ± 3	0.76	2.3 ± 0.01	217 ± 3
4-1.4.39 4-1.4.39IA	2.3	0.062 ± 0.005 -	15 ± 3 -	0.84 -	2.3 ± 0.03 -	251 ± 7 225 ± 5

The determined values of the volume fractions agree generally with the level of neutron exposure. An exception is thickness location 118 mm (specimen 4-6.14.134, Table 13) of the beltline welding seam SN0.1.4. of the Unit 4 RPV. The investigated disc from this thickness location had also a higher HV10 value as those from the thickness locations 86 mm and 132 mm (specimens 4-6.10.96 and 4-6.16.156, Table 13). The relationship between hardening and the square root of the volume fraction of irradiation-induced clusters $\Delta HV10 = 970c^{1/2}$ derived from the same kind of weld material in [Ulbricht-2007] is in reasonable agreement with the measured values in Table 13. The measured A-ratios agree for all layers of the weld metal, but are significantly higher than the value of A-ratio = 1.6 reported in [Ulbricht-2007]. This finding indicated differences in cluster composition. The smaller neutron flux of the RPV wall material is a possible explanation for the higher A-ratio. The estimated vacancy fraction in the clusters was about 14% for the Unit 4 beltline welding seam SN0.1.4. (for calculation basis see [Ulbricht-2007]).
The corresponding results for the Unit 4 forged base metal ring 0.3.1. (thickness location 32 mm, specimen 4-1.4.39, Table 12) are shown in Fig. 77 and Fig. 78 and also in Table 13. The base material had a lower susceptibility to form nano-scaled clusters in comparison with the weld metal under the same irradiation conditions. Size and type of clusters were similar to the investigated weld metal.

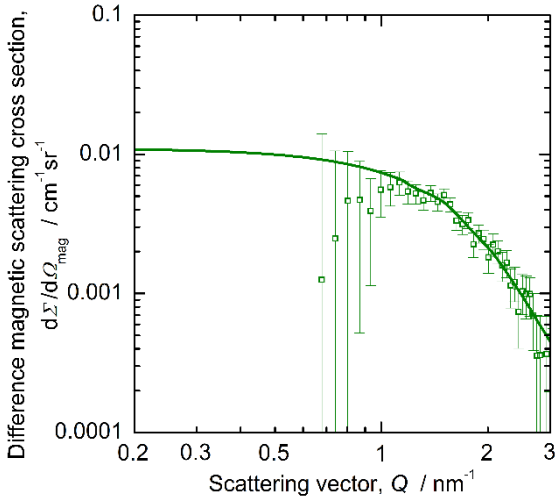

Fig. 77: Measured magnetic difference scattering curve with the post-irradiated annealed condition as reference for layer 4 of the base material of Unit 4.

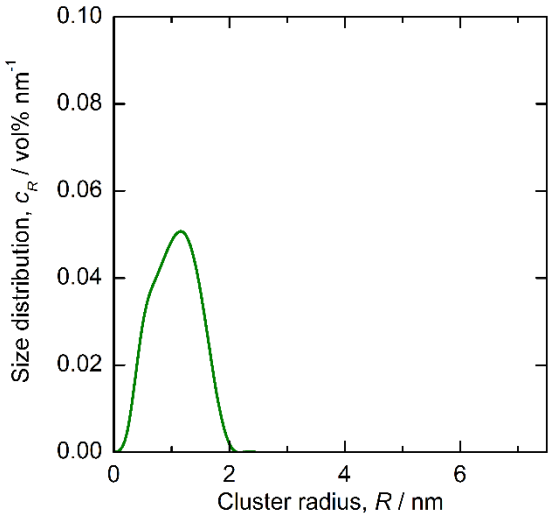

Fig. 78: Size distribution of irradiation-induced clusters for layer 4 of the base material of Unit 4.

Post-irradiation annealed conditions and re-irradiated condition

It was shown above that laboratory annealing indicates complete dissolution of irradiation-induced clusters without any visible coarsening. The SANS result for the large-scale annealing of Greifswald Unit 1 (sample 1-1.1.1) and Unit 2 (sample 2-3.1.2) are presented in Fig. 79 in the same manner as Fig. 71 and Fig. 72. It is found that both samples exhibit a slightly increased scattering cross-section at medium Q-values. This indicates that not only dissolution of irradiation-induced clusters occurred but also partial coarsening could appear. Such behaviour was also reported in [Ulbricht-2007]. No effect of re-irradiation was observed for the beltline welding seam SN0.1.4. of the Unit 1 RPV. Due to both the lack of appropriate

measurements on reference conditions and the measured small effects it is impossible to calculate size distributions for welds of Unit 1 and 2 with reasonable accuracy.

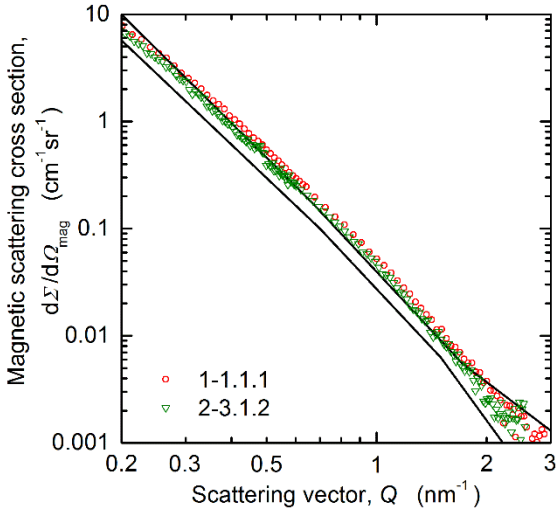

Fig. 79: Magnetic scattering cross-sections of the post-irradiated annealed condition of weld sample 2-3.1.2 and re-irradiated weld sample 1-1.1.1. (Table 12). The solid lines indicate the scatter band of the unirradiated conditions.

Summary and Conclusions

Post mortem investigations were performed on the reactor pressure vessels of 1st generation WWER-440/V-230 reactors of the Greifswald NPP. Trepans were sampled from the beltline weld seam SN0.1.4. and the forged base metal ring 0.3.1. of the units 1, 2 and 4 RPVs, which represented different material conditions (irradiated, annealed and re-irradiated). Charpy size SE(B) specimens from defined locations through the thickness of the RPV wall were tested according to the test standard ASTM E1921. The specimen orientation was T-S and L-S for the beltline welding seams SN0.1.4. and the forged base metal ring 0.3.1., respectively and followed the Russian Code [PNAEG-1986, Brumovsky-2005]. In addition Charpy V-notched and tensile specimens were machined from selected thickness locations of the RPV wall. The main focus of the investigations was on the application of the Master Curve Concept and the VERLIFE integrity assessment procedure [VERLIFE-2015, Brumovsky-2018a] based on it. The results are compared with the test parameters which are to be determined in the current RPV integrity assessment codes and predictions. Two of the PRV were large scale thermally annealed which allows to validate this mitigation method.

The results can be summarised as follows:

- As expected because of the attenuated neutron loading, the hardness and yield and ultimate tensile strength values decreased beyond the root of the Unit 4 multilayer beltline welding seam SN0.1.4. towards the RPV outer wall. The hardness and yield and ultimate tensile strength values of the large-scale thermally annealed beltline welding seams of the Unit 1 and 2 RPVs are significantly lower compared to Unit 4. In particular the scatter of the hardness values is rather high through the multilayer beltline welding seams of the three units and indicates inhomogeneous material.
- There was a large variation in the evaluated through-thickness T_0 values of the investigated multilayer beltline welding seams SN0.1.4.. Within the sampling range of

the surveillance specimens for the WWER 440 second generation RPVs, the T_0 values varied with a span of 58 K without a decreasing trend towards the outer RPV wall. This was also the case for the large-scale thermally annealed Unit 1 and 2 beltline welding seam, where the T_0 span was 59 K and 49 K, respectively.

- The cleavage fracture toughness values $K_{Jc,}$ measured on specimens sampled through the thickness of the multilayer beltline welding seam SN0.1.4., strongly depend on the intrinsic weld bead microstructure and the different filling materials used for weld root and the main weld. Hence, the position of the fatigue crack tip of the pre-cracked SE(B) specimen at the multilayer welding seam was crucial and defined the cleavage fracture toughness. The reasons for the differences in the fracture toughness of the individual thickness location had to be seen in microstructural features, which are not resolved in the optical microscope. The investigation of these microstructural features would require target-oriented measurements with electron backscattering diffraction, transmission electron microscopy and atom probe tomography.
- The test standard ASTM E1921 qualifies such materials as non-uniform and not amenable to the statistical analysis methods employed in this test standard. Fracture toughness K_{Jc} data of non-uniform steels should be evaluated with modified MC-based approaches like SINTAP [SINTAP-1999] and multi-modal [Wallin-2004, Scibetta-2010, Viehrig-2006] approaches. These evaluation approaches provide a reference temperature which is representative for the brittle fraction (SINTAP) and the continuous distribution of K_{Jc-1T} values (MM) of the material to be assessed.
- These results indicate that when surveillance specimens sampled from different thickness locations of the multilayer welding seam SN0.1.4. were grouped to one test series, it must be emphasized that K_{Jc} values measured in a specified range of test temperatures scatter strongly and can be invalid because of violating the specimen size criteria, $K_{Jc(limit)}$.
- The T_0 values evaluated with specimens sampled from the forged base metal ring 0.3.1. of the Greifswald Unit 4 RPV were in the range from -121 °C to -130 °C and indicated no irradiation induced embrittlement within the through thickness fluence range from 5.38 to $1.20 \cdot 10^{19}$ n/cm^2 (E > 0.5 MeV). The summarized evaluation of the K_{Jc} values from the surveillance thickness locations gave a T_0 value of -120 °C, but 9 out of 84 K_{Jc-1T} values (11 %) were not enveloped by the MC for 2% fracture probability. The application of the MM approach [Wallin-2004, Viehrig-2006, Scibetta-2010] on the summarised dataset did not significantly improve the situation. Here the number of not enveloped values is reduced to about 8%. It was pointed out that depending on the test temperature and the number of specimens, there is a threshold K_{Jc} value below which the reference temperature evaluated according to the SINTAP procedure step 3, $T_0^{SINTAP-3}$, becomes imaginary, which applied to values below 26 MPa√m in the present case.
- It was demonstrated that T_0 evaluated according to the SINTAP MC extension represented the brittle fraction of the data sets and is therefore suitable for the nonhomogeneous base metal.
- The less irradiation susceptibility of the steel 15Kh2MFA of forged Unit 4 RPV ring was also demonstrated with tensile und Charpy-V impact testing, where no hardening and TT_{47J} values in the range from -19 °C to -49 °C were measured, respectively.

- The less irradiation susceptibility of the 15Kh2MFA base metal is confirmed by the results investigated on the irradiated, thermally annealed and two campaigns again operated Greifswald Unit 1 RPV. Here T_0 values in the range from -105 °C to -110 °C through the wall thickness were investigated. The Charpy-V TT_{47J} values in the range from 2 °C to -26 °C are even higher compared to not annealed Unit 4 after the operation for 11 campaign.
- Table 14 summarizes for the investigated RPV materials the VERLIFE reference temperatures and the temperatures when the VERLIFE reference curve reaches toughness level of 80 MPa√m, which is relevant for a pressurized thermal shock event.

Table 14: VERLIFE reference temperatures and temperatures when the VERLIFE reference curve reaches a toughness of 80 MPa√m.

Unit	material	T_0	T_0^{SINTAP}	VERLIFE		T (80 MPa√m)	
				RT_0	RT_0^{SINTAP}	RT_0	RT_0^{SINTAP}
		°C	°C	°C	°C	°C	°C
1	welding seam SN0.1.4.	-25	16	-6	47	27	69
	forged base metal ring 0.3.1	-109	-59	-83	-33	-62	-12
2	welding seam SN0.1.4.	-26	0	5	31	26	53
4	welding seam SN0.1.4.	74	84	105	115	127	136
	forged base metal ring 0.3.1.	-120	-35	-89	-3	-67	18

- The MM approach is more adequate for the investigated non-homogeneous multilayer weld metal. As a consequence a large number of specimens (minimum 18) is required to get a valid T_0^{MM} [Scibetta-2010]. There are no standard analytical expressions for fracture toughness vs. temperature curves of defined fracture probabilities, therefore, T_0^{MM} cannot be applied to index the VERLIFE [VERLIFE-2015] and others like ASME [ASME-N629] and ENSI [ENSI-B01/d] reference curves.
- In general, irradiation induced ductile-to-brittle transition temperature shift predicted by the Russian PNAE G code [PNAE G-1986] was not confirmed by the values measured on specimens from the multilayer beltline welding seam 0.1.4. and the forged base metal ring 0.3.1..
- There is clear effect of the thermal annealing at 475 °C for 152 h measured by:
  - Charpy-V tests with ΔTT_{47J} = 106 K beyond the Unit 4 welding root and
  - MC tests with $\Delta T0$ = 47 K and = 91 K before and beyond the Unit 4 welding root, respectively. The T_0 values of the thermally annealed specimens from the Unit 4 beltline welding seam lie within the scatter of the T_0 progression of the large-scale thermally annealed beltline welding seam of the Greifswald Unit 2 RPV. The efficiency of the large-scale thermal annealing of the Greifswald WWER 440/V230 RPVs could be confirmed.
- For the as-irradiated conditions of Unit 4 weld metal, size distributions and A-ratios of irradiation-induced clusters were determined by SANS measurements. Cu-enriched clusters of similar volume fraction, size and hardening were found as also observed for surveillance specimens investigated in [Ulbricht-2007] but significantly higher A-ratios indicating differences of the cluster composition. The smaller neutron flux of the RPV wall material is a candidate explanation for the higher A-ratio. The determined vacancy fraction in the clusters is 14% for weld of Unit 4.

- The volume fraction of irradiation induced clusters measured by SANS decreased with the attenuation of the neutron loading through the thickness of the beltline welding seam SN0.1.4. of the Unit 4 RPV. An exception was the thickness location 118 mm, where also the highest T_0 was measured, the volume fraction of clusters and the hardness was locally higher.
- The laboratory annealing of weld material from Unit 4 indicates dissolution of the irradiation-induced clusters without any visible coarsening. In contrast, SANS results obtained for the annealed welds from Unit 1 and 2 indicate partial coarsening. No effect of re-irradiation was observed for weld of Unit 1 as expected because of the short duration of re-irradiation and the smaller rate of cluster formation reported in [Ulbricht-2007]. All annealing treatments resulted in a partial or complete recovery of the hardness.
- The investigation of the overlay cladding from the decommissioned first generation WWER-440 Greifswald Unit 4 RPV contributes to the understanding in terms of its stability under real operation conditions.
- As the initial strength and fracture toughness data of the cladding were missing, the radiation susceptibility of the investigated overlay cladding could not be assessed. Tensile strength data in the literature (Timofeev-2006) indicated an irradiation induced increase of the yield strength by 30%.
- The main focus in the investigation of the cladding was on the measurement of J vs. Δa curves by using the unloading compliance technique and the evaluation of initiation fracture toughness values according to the test standard ASTM E1820.
- The fracture toughness of the cladding is reduced by intercrystalline fracture at low temperature and the decreasing yield strength at high temperature. This resulted in a maximum of the initiation fracture toughness values, K_{JQ}, in the temperature range between ambient temperature and 80 °C.
- A significant scatter was caused by the crack moving through the heterogeneous microstructure of the overlay cladding. Furthermore, the J-Δa data determined from the first partial unloading sequences tend to scatter, which has a strong impact on the evaluated crack initiation J_Q values.
- Crack jumps and unstable failure were found after 1 mm ductile crack extension above ambient temperatures and below -50 °C, respectively. Above ambient temperature, the lowest initial fracture toughness values, K_{JQ}, were determined to be about 100 MPa√m. This value is above the stress intensity factors estimated for a postulated surface crack in the overlay cladding during a PTS transient [Abendroth-2007, Viehrig-2015b]. It can be stated that the overlay cladding of the Greifswald Unit 4 RPV would remain intact and increase confidence in the safety of the structural integrity of the RPV after the operation up to 25 % of the designed neutron loading for 30 full power years. An increase of the neutron fluence can shift the range of unstable crack extension and the occurrence of crack jumps to lower fracture toughness values and higher temperatures, respectively, which might affect the integrity of the RPV.

References

Abendroth-2007: Abendroth, M., Altstadt, E.: Fracture mechanical analysis of a thermal shock scenario for a VVER-440 RPV, Scientific technical reports of Forschungszentrum Dresden-Rossendorf FZD-474 ISSN 1437-322X, June 2007.

Ahlstrand-1993: Ahlstrand, R., Klausnitzer, E. N., Langer, D., Leitz, Ch., Pastor, D. Valo, M.: Evaluation of the recovery annealing of the reactor pressure vessel of NPP Nord (Greifswald) Units 1 and 2 by means of subsize impact specimens. Radiation Embrittlement of Nuclear Reactor Pressure Vessel Steels: An International Review (Fourth Volume), ASTM STP 1170. Lendell E. Steel, Ed., American Society for testing and materials, Philadelphia, 1993, pp. 321-343.

Alekseenkov-1997: Alekseenkov, N. N., Amaev, A., Gorynin, I., Nikolaev, V.A.: Radiation Damage of Nuclear Power Plant Vessel Steels. American Nuclear Society, La Grange Park, Illinois, USA, 1997.

ASME N-629: American Society of Mechanical Engineers: Use of fracture toughness test data to establish reference temperature for pressure retaining materials. Section XI, Division1, ASME Boiler and Pressure Vessel Code Case N-629, ASME, New York, 1999.

ASME NB-2300: American Society for Mechanical Engineers, Rule for construction of nuclear power plants. ASME Boiler and Pressure Vessel Code, Sect. III: Rep.. ASME NB-2300, ASME, New York, 2002.

ASTM E1823-07: Standard Terminology Relating to Fatigue and Fracture Testing, Annual Book of ASTM Standards, ASTM International, West Conshohocken, PA, 2007.

ASTM E1921-09: ASTM Standard Test Method for Determination of Reference Temperature, T_0, for Ferritic Steels in the Transition Range, *Annual Book of ASTM Standards*, ASTM International, West Conshohocken, PA, 2009.

ASTM E399-09: Standard Test Method for Linear-Elastic Plane-Strain Fracture Toughness K_{Ic} of Metallic Materials, ASTM International, 2009.

Barz-1998a: Barz, H.-U., Böhmer, B., Konheiser, J. and Stephan I.: High-Precision Monte Carlo calculations, experimental verification and adjustment of fluences in the pressure vessel cavity of a VVER-1000. Proc. 1998 ANS Radiation Protection and Shielding Division Topical Conference Technologies for the New Century, April 19-23, 1998, Nashville, Tennessee, USA, Vol. 1, pp. 447-454.

Barz-1998b: Barz, H.-U, Konheiser, J.: Monte-Carlo Programm TRAMO - Möglichkeiten und Anleitung zur Nutzung. FZR Bericht-245, Rossendorf, Dezember 1998.

Baers-1992: Baers, L. B. and Hasanen, E. K.: Experimental estimation of neutron fluxes from niobium impurities in the pressure vessel steel of nuclear power reactors. Nuclear Instruments and Methods in Physics Research A317 (1992) 577-580.

Boehmer-1999: Boehmer, B., Boehmert, J., Mueller, G., Rindelhardt, U. and Utke, H.: Embrittlement studies of the reactor pressure vessel of the Greifswald-440 reactors. Technical Report Task 4: Data Collection, Project Reference: NUCRUS96601 Technical Report, published October 1999, TACIS service DG IA, European Commission, TACIS Information Office, European Commission, Aarlenstraat 88 1/06 Rue d' Arlon, 1040 Brussels, Belgium.

Bondarenko-1962: Bondarenko, I. I., Group Constants for Nuclear Reactor Calculations. Constants Bureua, New York, 1964.

Beaven-1986: P. A. Beaven, F. Frisius, R. Kampmann, R. Wagner: Analysis of defect microstructures in irradiated ferritic alloys. in: Janot, C., Petry, W., Richter, D., Springer, T. (Eds.): Atomic Transport and Defects in Metals by Neutron Scattering. Springer Proceedings in Physics, vol. 10, Springer Verlag, Berlin, 1986, p. 228.

Brumovsky-1997: Brumovský, M., Novosad, P., Vacek, M.: Cladding Properties Changes During Operation. Proceedings of the IAEA specialists meeting on irradiation effects and mitigation, Vladimir, Russia 15-19 September 1997, IWG-LMNPP-92/2, IAEA, Vienna, Austria, 1997.

Brumovsky-2003: Brumovský, M.: Unified procedure for lifetime assessment of component and piping in WWER NPPs - VERLIFE. European Commission, Final Report, Contract N° FIKS-CT-2001-20198, September 2003.

Brumovsky-2005: Brumovský, M., Valo, M., Kryukov, A., Gillemot, F., Debarberis, L. and Kang, K.: Guidelines for prediction of irradiation embrittlement of operating WWER-440 reactor pressure vessels, IAEA-TECDOC-1442, IAEA, Vienna, 2005.

Brumovsky-2018a: Brumovský, M.: The Bases for WWER Vessel Surveillance Programs: General Requirements. International Review of Nuclear Reactor Pressure Vessel Surveillance Programs, ASTM STP1603, Server, W. L. and Brumovský, M. (Eds.), ASTM International, West Conshohocken, PA, 2018, pp. 54–67, http://dx.doi.org/10.1520/STP16032016016.

Brumovsky-2018b: Brumovský, M.: Structural Integrity Lessons Learned in WWER RPV Surveillance Specimen Programs. International Review of Nuclear Reactor Pressure Vessel Surveillance Programs, ASTM STP1603, Server, W. L. and Brumovský, M. (Eds.), ASTM International, West Conshohocken, PA, 2018, pp. 404–431, http://dx.doi.org/10.1520/STP160320170027.

Carter-2001: Carter, R. G., Soneda, N., Dohi, K., Hyde, J. M., English, C. A.,W. L. Server, W. L.: Microstructural characterization of irradiation-induced Cu-enriched clusters in reactor pressure vessel steels. Journal of Nuclear Materials 298 (2001) 211–224.

Chadwick-2006: Chadwick, et al.: ENDF/B-VII.0: Next Generation Evaluated Nuclear Data Library for Nuclear Science and Technology. Nuclear Data Sheets Volume 107, Issue 12, December 2006, Pages 2931-3060.

DIN EN 10045-1 (1991): Metallic Materials: Charpy Impact Test; Part 1. DIN-Taschenbuch 19, Werkstoffprüfnormen für metallische Wekstoffe 1, Beut Verlag GmbH, 2003.

Dufresne-1981: Dufresne J.: Probabilistic application of fracture mechanics. In Advances in Fracture Research. Fracture 81, 2, 517-531,1981.

ENSI-B01/d: Alterungsüberwachung, Richtlinie für die schweizerischen Kernanlagen. Swiss Federal Nuclear Safety Inspectorate ENSI, August 2012.

Gillemot-2007: Gillemot, F., Horvath, M., Uri, G., Fekete, T., Houndeffo, E., Acosta, B., Debarberis, L. Viehrig, H.-W.: Radiation stability of WWER RPV cladding materials. Int. J. Pres. Ves. Pip. 84, 469-474, 1981. http://dx.doi.org/ 10.1016/j.ijpvp.2007.04.004.

Haggag-1990: Haggag, F.M., Corwin, W.R., Nanstad R.K.: Effects of irradiation on the fracture properties of steel weld overlay cladding. Nucl. Eng. Des. 124, 129-141, 1990. http://dx.doi.org/10.1016/0029-5493(90)90359-6.

IAEA-1997: N.N.: Guidelines on pressurized thermal shock analysis for WWER nuclear power plants. IAEA-EBP-WWER-08, IAEA, Vienna, 1997.

ISO 148-1: Metallic materials - Charpy pendulum impact test - Part1: Test method, 2009.

ISO 6892-1: Metallic materials - Tensile testing - Part 1: Method of test at room temperature, 2009.

Keiderling-1995: Keiderling, U., Wiedenmann, A.: New SANS instrument at the BER II reactor in Berlin. Germany, Physica B 213-214 (1995) 895-897.

Keiderling-2002: Keiderling, U.: The new 'BerSANS-PC' software for reduction and treatment of small angle neutron scattering data. Applied Physics A 74 [Suppl.] (2002) S1455–S1457.

Konheiser-2006: Konheiser, J., Rindelhardt, U., Viehrig, H.-W., Böhmer, B. and Gleisberg, B.: Pressure vessel investigations of the former Greifswald NPP: fluence calculations and Nb based fluence measurements. ICONE14/FEDSM2006 Proceedings, Contribution ICONE 14-89578, 2006M.

KTA 3201.2: Safety Standards of the Nuclear Safety Standards Commission (KTA), KTA 3201.2 (06/96) (incl. rectification from BAnz 129, 13.07.00): Components of the reactor coolant pressure boundary of light water reactors, Part 2: Design and Analysis . KTA-Geschaeftsstelle c/o Bundesamt fuer Strahlenschutz (BfS), Albert-Schweitzer-Strasse 18, 38226 Salzgitter, Germany.

Margolin-2017: Margolin, B. Z., Fomenko, V. N., Gulenko, A. G., Kostylev, V. I., Shvetsova, V. A.: Further improvement of the Prometey model and Unified Curve method part 1. Improvement of the Prometey model. Eng. Fracture Mechanics, Volume 182, September 2017, 467-486.

Margolin-2010: Margolin, B. Z.: personal information.

MacFarlane-1994: MacFarlane, R. E., Muir, D. W.: The NJOY Nuclear Data Processing System (Version 91), Los Alamos, LA-12740-M, 1994.

MacFarlane-2001: MacFarlane, R. E.: ENDF-102 Data formats and procedures for the evaluated nuclear data file ENDF-6. Revised April 2001, BNL-NCS-44945-01/04-Rev.

Pistora-2003: Pistora V., Kral P.: Evaluation of pressurised thermal shocks for VVER440/213 reactor pressure vessel in NPP Dukovany. Transactions 17th Int. Conf. on Struct. Mech. Reactor Technology (SMIRT-17), 2003 Paper G01-3.

PNAE G-1986: PNAE G-7-008-86: Strength calculation norms for nuclear power plant equipment and piping. Energoatomizad, Moscow, 1989.

Rindelhard-2009: Rindelhardt, U., Viehrig, H.-W., Konheiser, J., Gleisberg, B.: Weld material investigations of a VVER-440 reactor pressure vessel: Results from the first trepan taken from the former Greifswald NPP. J. Eng. for Gas Turbines and Power, 131 (2009), 022904-1 - 022904-7.

Rosinski-1999: Rosinski, S.: Application of Master Curve fracture toughness methodology for ferritic Steels. (PWRMRP-01) PWR Materials Reliability Project (PWRMRP), EPRI, Palo Alto, CA, USA: 1999TR-108390, Revision 1.

Rosinski-2000: Rosinski, S. T., Server, W. L.: Application of the Master Curve in the ASME Code. International Journal of Pressure Vessels and Piping, Volume 77, Issue 10, 15 August 2000, pp. 591-598.

Scibetta 2010: Scibetta, M.: Treatment of non homogeneous data set. ASTM E8 Workshop on MC for Inhomogeneous Materials, San Antonio, TX, 17 November 2010.

Server-2000: Server, W. L., Rosinski, S.T.: Technical basis for application of the Master Curve approach in reactor pressure vessel integrity assessment. Effects of Radiation on Materials. 19th International Symposium, ASTM STP 1366, Hamilton, M. L., Kulmar, A. S., Rosinsky, S. T. and Grossbeck, M. L. (Eds.), American Society for Testing and Materials, West Conshohocken, PA, 2000,pp. 127-142.

Server-2005: Server, W. L. et al.: IAEA guidelines for application of the Master Curve approach to reactor pressure vessel integrity in nuclear power plants. IAEA-Technical Reports Series 429, IAEA in Austria, March 2005.

Shibata-2002: Shibata, K., at al.: Japanese Evaluated Nuclear Data Library Version 3 Revision-3: JENDL-3.3. J. Nucl. Sci. Technol. 39, 1125 (2002)

SINTAP-1999: Structural Integrity Assessment Procedures for European Industry (SINTAP). Final Version: WEM/SINTAP/PROC_7/CONTENTS REGP (05/11/99), November 1999.

Soneda-2013: Soneda, N.: Embrittlement of RPV steels due to formation of irradiation-induced solute atom clusters. IAEA Technical Meeting on Degradation of primary components of pressurised water cooled nuclear reactors: Current issues and future challenges, 5-8 November 2013, Vienna, Austria.

Suschowk-2002: Suschowk, G.: Daten zur Berechnung von Neutronenflussdichten in den Reaktordruckgefäßen der Blöcke 1 bis 4 der EWN GmbH, Technische Unterlage 6252/BK/H0031266, 2002.

Timofeev-2006: Timofeev, B. T., Karzov, G. P.: Assessment of the WWER-440/V-213 reactor condition. Int. J. Pres. Ves. Pip., 83, 3 (2006) 216-226.

Ulbricht-2007: Ulbricht, A., Bergner, F., Böhmert, J., Valo, M., Mathon, M.-H., Heinemann, A.: SANS response of VVER440-type weld material after neutron irradiation, post-irradiation annealing and reirradiation. Philosophical Magazine 87 (2007) 1855-1870.

Ulbricht-2011: Ulbricht, A., Altstadt, E., Bergner, F., Viehrig, H.-W., Keiderling, U.: Small-angle neutron scattering investigation of as-irradiated, annealed and reirradiated reactor pressure vessel weld material of decommissioned reactor. J. Nucl. Mater. 416 (2011) 111–116.

Valo-2010: Valo, M., Pre-characterisation of Greifswald trepan samples. Research Report VTT-R-03746-10 (2010).

VERLIFE-2015: IAEA-NULIFE-VERLIFE 2011: Guidelines for Integrity and Lifetime Assessment of Components and Piping in WWER Nuclear Power Plants during Operation. IAEA, Vienna, Austria, 2015.

Viehrig-2000: Viehrig, H.-W., Böhmert, J., Dzugan, J., Richter, H.: Master Curve Evaluation of Irradiated Russian VVER Type Reactor Pressure Vessel Steels. Effects of Radiation on Materials: 20th International Symposium, June 2000, ASTM STP 1405, Rosinski, S. T., Grossbeck, M. L., Allen, T. R. and Kumar, A. S. (Eds.), American Society for Testing and Materials, West Conshohocken, 109-124.

Viehrig-2006: Viehrig, H.-W., Scibetta, M., Wallin, K.: Application of advanced Master Curve approaches on WWER-440 reactor pressure vessel steels. International Journal Pressure Vessel and Piping 83(2006) Issue 8, August 2006, pp. 584-592.

Viehrig-2007: Viehrig, H.-W., Rindelhardt, U. and Schuhknecht, J.: Post mortem investigations of the NPP Greifswald WWER-440 reactor pressure vessels. Proceedings of the 19th

International Conference on Structural Mechanics in Reactor Technology, 12-17 August 2007, Toronto, Canada.

Viehrig-2009a: Viehrig, H.-W., Schuhknecht, J., Rindelhardt, U., Weiss, F.-P.: Investigation of the beltline welding seam of the Greifswald WWER-440 unit 1 reactor pressure vessel. Journal of ASTM International 6(2009)5.

Viehrig-2009b: Viehrig, H.-W. and Schuhknecht, J.: Fracture mechanics characterisation of the WWER-440 reactor pressure vessel core welding seam. International Journal of Pressure Vessels and Piping 86 (2009) Issue No. 4, pp. 239-245.

Viehrig-2011: Viehrig, H.-W., Houska, M., Ulbricht, A., Konheiser, J., Altstadt E. and Noack, K.: Scientific technical cooperation with Russia: Investigation of the mechanisms of neutron embrittlement and annealing procedures as well as fluence calculations for reactor pressure vessels of WWER-type reactors. Final Report Reactor Safety Research-Project No.: 150 1331, Report No.: HZDR\FWS\2011\06, December 2011.

Viehrig-2012a: Viehrig, H.-W., Altstadt, E., Houska, M., Valo, M.: Fracture mechanics characterisation of the beltline welding seam of the decommissioned WWER-440 reactor pressure vessels of nuclear power plant Greifswald Unit 4. Int. J. Pres. Ves. Pip. 89, 129-136. http://dx.doi.org/ 10.1016/j.ijpvp.2011.10.016.

Viehrig-2012b: Viehrig, H.-W., Houska, M, Altstadt, E., Kuechler, R.: Fracture mechanics characterisation of forged base metal ring of the decommissioned reactor pressure vessel of NPP Greifswald WWER-440 Unit 4. Effects of Radiation on Nuclear materials: 25th Volume on June 15-17 2011 in Anaheim, CA; STP 1547, Takuya Yamamoto. Guest Editor, pp. 69-84, doi:10.1520/STP104056, ASTM International, West Conshohocken, PA 2012.

Viehrig-2015a: Viehrig, H.-W., Houska, M., Altstadt, E.: Radiation and annealing response of WWER 440 beltline welding seams. J. Nuclear Materials 456(2015), 334-343.

Viehrig-2015b: Viehrig, H.-W., Altstadt, E., Houska, M.: Radiation response of the overlay cladding from the decommissioned WWER-440 Greifswald Unit 4 reactor pressure vessel. Nuclear Eng. and Design 286 (2015), 227–236.

Viehrig-2018: Viehrig, H.-W., Altstadt, E., Houska, M., and Valo, M.: Validation of Surveillance Concepts and Trend Curves by the Investigation of Decommissioned Reactor Pressure Vessels. International Review of Nuclear Reactor Pressure Vessel Surveillance Programs, ASTM STP1603, Server, W. L. and Brumovsky, M., (Eds.), ASTM International, West Conshohocken, PA, 2018, pp. 457–483, http://dx.doi.org/10.1520/STP160320160127

Wallin-2004: Wallin, K., Nevasmaa, P., Laukkanen, A., Planmann T.: Master Curve analysis of inhomogeneous ferritic steels. Eng. Fracture Mechanics. Volume 71, Issues 16-17, November 2004, pp. 2329-2346.

Wallin-2010: Wallin, K.: personal discussion, 2010.

Acknowledgement

This study was supported by the German Federal Ministry of Economics and Technology, (Reactor Safety Research Project Grant No. 1501331), and by the European Commission through the FP7 project LONGLIFE (contract No. 249360).

The authors would like to thank Prof. Dr. Udo Rindelhard and Prof. Dr. Frank-Peter Weiß for the continuous support in the realization of the project.

Our special thanks apply to the company Studsvik GmbH & Co. KG, Niederlassung Blankenloch and Energiewerke Nord GmbH for the realization of the sampling at reactor pressure vessels at place.

Appendix

Table A 1: Neutron loading of the discs machined though the thickness of the trepan 1-1 from the beltline welding seam SN0.1.4. of the Greifswald Unit 1 RPV.

disc code	discs		fluence E>0.5 MeV			flux E>0.5 MeV total	fluence E>1 MeV			flux E>0.5 MeV total
	thickness mm	location* mm	before annealing 10^{19} n/cm^2	after annealing 10^{17} n/cm^2	total 10^{19} n/cm^2	10^{10} n/cm^{2}s	before annealing 10^{19} n/cm^2	after annealing 10^{17} n/cm^2	total 10^{19} n/cm^2	10^{10} n/cm^{2}s
0		0	3.930	11.668	3.942	9.442	2.533	7.329	2.540	6.085
1-1.1	10	8	3.897	11.825	3.909	9.362	2.422	7.114	2.429	5.819
1-1.2	3	15	3.798	11.623	3.810	9.125	2.294	6.785	2.300	5.510
1-1.3	10	22	3.659	11.250	3.670	8.790	2.147	6.385	2.153	5.158
1-1.4	3	29	3.494	10.784	3.505	8.394	1.993	5.956	1.999	4.788
1-1.5	10	36	3.315	10.275	3.326	7.965	1.839	5.526	1.845	4.418
1-1.6	10	42	3.131	9.755	3.140	7.522	1.689	5.109	1.694	4.058
1-1.7	3	53	2.844	8.964	2.853	6.834	1.472	4.508	1.477	3.537
1-1.8	10	60	2.663	8.465	2.671	6.398	1.343	4.148	1.347	3.226
1-1.9	10	70	2.399	7.729	2.406	5.763	1.163	3.641	1.166	2.794
1-1.10	3	77	2.233	7.256	2.240	5.365	1.055	3.329	1.058	2.535
1-1.11	10	84	2.075	6.792	2.082	4.986	0.956	3.034	0.959	2.296
1-1.12	10	94	1.852	6.117	1.858	4.450	0.821	2.621	0.823	1.972
1-1.13	3	101	1.716	5.694	1.721	4.123	0.742	2.372	0.744	1.782
1-1.14	10	107	1.588	5.294	1.593	3.816	0.671	2.144	0.673	1.611
1-1.15	10	118	1.405	4.728	1.410	3.376	0.575	1.838	0.576	1.380
1-1.16	3	125	1.284	4.362	1.289	3.087	0.515	1.653	0.517	1.239
1-1.17	10	131	1.155	3.969	1.159	2.776	0.455	1.469	0.456	1.093

* distance of the disc centre from the RPV inner wall

Table A 2: Neutron loading of the discs machined though the thickness of the trepan 1-4 from the forged base metal ring 0.3.1. of the Greifswald Unit 1 RPV.

disc code	discs		fluence E>0.5 MeV			flux E>0.5 MeV total	fluence E>1 MeV			flux E>0.5 MeV total
	thickness mm	location* mm	before annealing 10^{19} n/cm^2	after annealing 10^{17} n/cm^2	total 10^{19} n/cm^2	10^{10} n/cm^{2}s	before annealing 10^{19} n/cm^2	after annealing 10^{17} n/cm^2	total 10^{19} n/cm^2	10^{10} n/cm^{2}s
0		0	5.150	16.087	5.166	12.374	3.291	9.996	3.301	7.906
1-4.1	10	8	5.147	16.131	5.163	12.367	3.171	9.626	3.181	7.618
1-4.2	3	15	5.019	15.802	5.035	12.058	3.007	9.146	3.016	7.224
1-4.3	10	22	4.825	15.276	4.840	11.593	2.813	8.586	2.822	6.759
1-4.4	10	33	4.439	14.185	4.453	10.665	2.473	7.602	2.481	5.942
1-4.5	10	43	4.108	13.221	4.121	9.871	2.205	6.817	2.212	5.297
1-4.6	3	49	3.873	12.521	3.886	9.306	2.022	6.278	2.029	4.859
1-4.7	10	56	3.647	11.836	3.659	8.763	1.853	5.773	1.859	4.453
1-4.8	10	66	3.321	10.837	3.331	7.979	1.621	5.072	1.627	3.896
1-4.9	10	77	3.010	9.880	3.020	7.234	1.414	4.439	1.419	3.398
1-4.10	3	84	2.812	9.270	2.822	6.758	1.289	4.054	1.293	3.097
1-4.11	10	90	2.619	8.678	2.628	6.293	1.172	3.694	1.175	2.815
1-4.12	10	101	2.336	7.819	2.343	5.613	1.008	3.196	1.011	2.422
1-4.13	10	111	2.067	7.017	2.074	4.969	0.862	2.759	0.865	2.071
1-4.14	3	118	1.899	6.520	1.906	4.565	0.775	2.505	0.778	1.863
1-4.15	10	125	1.737	6.045	1.743	4.175	0.695	2.275	0.697	1.670
1-4.16	10	132	1.558	5.526	1.564	3.746	0.610	2.040	0.612	1.466

* distance of the disc centre from the RPV inner wall

Table A 3: Neutron loading of the discs machined though the thickness of the trepan 2-3 from the beltline welding seam SN0.1.4. of the Greifswald Unit 2 RPV.

disc code	discs		fluence E>1 MeV	flux E>1 MeV	fluence E>0.5 MeV	flux E>0.5MeV
	thickness mm	location* mm	10^{19} n/cm^2	10^{10} n/cm^{2}s	10^{19} n/cm^2	10^{10} n/cm^{2}s
0		0	3.104	8.832	4.738	13.482
2-3.1	10	8	2.959	8.419	4.710	13.402
2-3.2	3	15	2.795	7.952	4.586	13.048
2-3.3	10	22	2.611	7.429	4.406	12.539
2-3.4	10	32	2.322	6.608	4.082	11.616
2-3.5	3	39	2.137	6.081	3.855	10.970
2-3.6	10	46	1.961	5.579	3.628	10.323
2-3.7	10	56	1.714	4.879	3.294	9.372
2-3.8	10	66	1.494	4.250	2.976	8.470
2-3.9	3	73	1.361	3.872	2.777	7.902
2-3.10	10	80	1.237	3.520	2.585	7.357
2-3.11	10	90	1.066	3.034	2.310	6.574
2-3.12	10	101	0.915	2.605	2.054	5.845
2-3.13	3	107	0.827	2.353	1.895	5.393
2-3.14	9	113	0.757	2.155	1.764	5.019
2-3.15	10	123	0.659	1.876	1.562	4.445
2-3.16	10	133	0.565	1.607	1.335	3.800

* distance of the disc centre from the RPV inner wall

Table A 4: Neutron loading of the discs machined though the thickness of the trepan 4-1 from the forged base metal ring 0.3.1. of the Greifswald Unit 4 RPV.

disc code	discs		fluence E>1 MeV	flux E>1 MeV	fluence E>0.5 MeV	flux E>0.5MeV
	thickness mm	location* mm	10^{19} n/cm^2	10^{10} n/cm^{2}s	10^{19} n/cm^2	10^{10} n/cm^{2}s
0		0	3.481	12.556	5.384	19.419
4-1.1	10	9	3.320	11.976	5.373	19.379
4-1.2	10	20	3.031	10.931	5.112	18.436
4-1.3	3	26	2.814	10.149	4.871	17.567
4-1.4	10	33	2.594	9.357	4.610	16.627
4-1.5	10	44	2.276	8.209	4.214	15.199
4-1.6	10	54	1.988	7.172	3.840	13.851
4-1.7	10	64	1.734	6.256	3.495	12.605
4-1.8	10	74	1.511	5.450	3.172	11.442
4-1.9	3	81	1.378	4.969	2.968	10.706
4-1.10	10	88	1.254	4.522	2.770	9.992
4-1.11	10	98	1.083	3.905	2.481	8.949
4-1.12	10	107	0.946	3.413	2.238	8.072
4-1.13	10	117	0.824	2.973	2.011	7.254
4-1.14	10	127	0.704	2.538	1.775	6.402
4-1.15	3	134	0.632	2.278	1.625	5.859
4-1.16	10	141	0.561	2.024	1.467	5.290

* distance of the disc centre from the RPV inner wall

Table A 5: Neutron loading of the discs machined though the thickness of the trepan 4-2 from the forged base metal ring 0.3.1. of the Greifswald Unit 4 RPV.

disc code	discs thickness mm	discs location* mm	fluence E>1 MeV 10^{19} n/cm^2	flux E>1 MeV 10^{10} n/cm^{2}s	fluence E>0.5 MeV 10^{19} n/cm^2	flux E>0.5MeV 10^{10} n/cm^{2}s
0		0	3.481	12.556	5.384	19.419
4-2.1	10	7	3.366	12.139	5.399	19.473
4-2.2	10	18	3.092	11.152	5.175	18.665
4-2.3	3	24	2.878	10.382	4.945	17.834
4-2.4	10	31	2.658	9.588	4.687	16.907
4-2.5	10	42	2.336	8.424	4.290	15.472
4-2.6	10	52	2.042	7.363	3.911	14.105
4-2.7	10	62	1.781	6.424	3.560	12.840
4-2.8	3	69	1.627	5.868	3.342	12.054
4-2.9	10	76	1.485	5.355	3.133	11.299
4-2.10	10	86	1.289	4.650	2.828	10.200
4-2.11	10	96	1.114	4.020	2.536	9.148
4-2.12	5	104	0.995	3.590	2.327	8.392
4-2.13	10	112	0.887	3.197	2.128	7.675
4-2.14	10	122	0.758	2.734	1.883	6.791
4-2.15	10	132	0.645	2.327	1.653	5.964
4-2.16	10	143	0.538	1.940	1.411	5.091

* distance of the disc centre from the RPV inner wall

Table A 6: Neutron loading of the discs machined though the thickness of the trepan 4-4 from the beltline welding seam SN0.1.4. of the Greifswald Unit 4 RPV.

disc code	discs		fluence E>1 MeV	flux E>1 MeV	fluence E>0.5 MeV	flux E>0.5MeV
	thickness mm	location* mm	10^{19} n/cm^2	10^{10} n/cm^{2}s	10^{19} n/cm^2	10^{10} n/cm^{2}s
0		1	2.589	9.336	4.105	14.806
4-4.1	10	8	2.530	9.125	4.106	14.810
4-4.2	10	15	2.395	8.639	3.996	14.411
4-4.3	3	25	2.162	7.797	3.746	13.510
4-4.4	10	28	2.066	7.453	3.635	13.109
4-4.5	10	39	1.816	6.548	3.325	11.993
4-4.6	10	49	1.591	5.738	3.028	10.923
4-4.7	10	59	1.396	5.035	2.755	9.938
4-4.8	10	70	1.226	4.421	2.503	9.028
4-4.9	10	80	1.073	3.869	2.264	8.167
4-4.10	10	90	0.931	3.358	2.034	7.338
4-4.11	10	101	0.800	2.885	1.813	6.538
4-4.12	3	113	0.660	2.382	1.564	5.641
4-4.13	10	119	0.598	2.157	1.446	5.214
4-4.14	10	132	0.486	1.752	1.213	4.377
4-4.15	10	140	0.427	1.542	1.085	3.914

* distance of the disc centre from the RPV inner wall

Table A 7: Neutron loading of the discs machined though the thickness of the trepan 4-6 from the beltline welding seam SN0.1.4. of the Greifswald Unit 4 RPV.

disc code	discs thickness mm	discs location* mm	fluence E>1 MeV 10^{19} n/cm^2	flux E>1 MeV 10^{10} n/cm^{2}s	fluence E>0.5 MeV 10^{19} n/cm^2	flux E>0.5MeV 10^{10} n/cm^{2}s
0		0	2.591	9.343	4.092	14.758
4-6.1	10	7.8	2.526	9.109	4.104	14.801
4-6.2	10	18.1	2.321	8.370	3.920	14.140
4-6.3	3	24.9	2.154	7.770	3.737	13.479
4-6.4	10	31.7	1.984	7.156	3.536	12.752
4-6.5	10	42	1.740	6.277	3.228	11.641
4-6.6	10	52.3	1.525	5.502	2.938	10.598
4-6.7	3	59.1	1.400	5.048	2.760	9.956
4-6.8	10	65.9	1.285	4.634	2.592	9.348
4-6.9	10	76.2	1.126	4.062	2.349	8.472
4-6.10	10	86.5	0.981	3.537	2.116	7.633
4-6.11	3	93.3	0.890	3.211	1.967	7.094
4-6.12	10	100.1	0.805	2.902	1.821	6.568
4-6.13	9	109.25	0.698	2.519	1.633	5.892
4-6.14	10	118.4	0.605	2.181	1.458	5.260
4-6.15	10	125.2	0.544	1.962	1.337	4.822
4-6.16	3	132	0.489	1.764	1.220	4.401
4-6.17	10	142.3	0.405	1.460	1.036	3.737

* distance of the disc centre from the RPV inner wall

Table A 8: Summary of tensile test results measured on rectangular tensile specimens from different thickness locations of the beltline welding seam SN0.1.4. of the Greifswald Unit 1 RPV (trepan 1-1).

specimen geometry	thickness location		condition	parameter Eq. (6)							
				$R_{p0.2}$				R_m			
	code	distance		σ_{YG}	b	h	20°C	σ_{YG}	b	h	20°C
mm · mm		mm		MPa			MPa	MPa			MPa
3 · 4	1-1.2	15	IAI	425.7	588.1	0.00620	521	468.8	731.8	0.00531	623
3 · 4	1-1.4	29	IAI	455.7	994.0	0.00940	519	499.4	939.7	0.00709	617
3 ·4	1-1.7	53	IAI	385.5	600.8	0.00530	513	456.0	784.5	0.00548	614
3 · 4	1-1.10	64	IAI	320.0	556.1	0.00420	482	352.0	678.7	0.00349	596
3 · 4	1-1.13	100	IAI	425.6	2893.7	0.01420	471	379.7	693.2	0.00416	585
3 ·4	1-1.16	124	IAI	407.2	722.3	0.00790	479	509.5	1543.1	0.01050	585
3 · 4	1-1.2&4	15-29	IAI	442.8	738.2	0.00770	520	488.1	821.8	0.00624	620
3 · 4	1-1.10&13&16	64-124	IAI	407.3	1025.5	0.00916	477	453.3	833.7	0.00627	586

Table A 9: Charpy-V test results measured on reconstituted Charpy V-notched specimens from different thickness locations of the large scale thermally annealed and re-irradiated beltline welding seam SN0.1.4. of the Greifswald Unit 1 RPV (trepan 1-1).

disc code	location* mm	parameter Eq. (8)				TT_{47J}	USE
		A	B	C	T_0		
		J	J		°C	°C	J
1-1.1	5	65	61	40	74	62	126
1-1.3	19	77	72	40	59	42	149
1-1.5	33	79	74	39	36	17	153
1-1.12	91	62	59	43	36	25	121
1-1.14	104	74	71	40	42	26	145

* distance of the notch tip from the RPV inner wall

Table A 10 Summary of MC (ASTM E1921) test results measured on SE(B) specimens from different thickness locations of the large scale thermally annealed and re-irradiated beltline welding seam SN0.1.4.of the Greifswald Unit 1 RPV (trepan 1-1).

thickness location		ASTM E1921									SINTAP	VERLIFE		
code	distance* mm	T_0 °C	σT_0 K	$\sum n_i r_i$	r	N	$< K_{Jc-1T}^{2\%}$		$> K_{Jc-1T}^{98\%}$		T_0^{SINTAP} °C	RT_0 °C	$< K_{Jc-1T}^{VERLIFE}$	
1-1.1	8	9.3	7.9	1.17	7	9	2		0		32.8	43.1	0	
1-1.3	22	48.9	7.2	1.29	9	9	0		0		48.9	82.7	0	
1-1.5	36	35.1	7.2	1.30	9	9	0		0		35.1	68.9	0	
1-1.6	46	-7.8	8.4	1.00	6	9	0		1		-7.8	26.0	0	
1-1.8	59	-3.8	7.2	1.40	9	9	0		0		5.3	30.0	0	
1-1.9	70	-36.3	7.9	1.12	7	10	1		0		-13.4	-2.8	0	
1-1.9(R)	70	-23.1	7.5	1.11	8	9	0		1		-2.7	10.7	0	
1-1.11	83	-35.1	8.4	1.00	6	9	1		0		37.2	-1.3	1	
1-1.12	94	22.3	7.5	1.17	8	9	1		1		45.3	56.1	0	
1-1.14	107	-31.3	7.9	1.20	7	9	0		0		-31.3	2.5	0	
1-1.15	118	-7.5	7.5	1.24	8	9	0		0		8.9	26.3	0	
1-1.17	131	58.9	9.0	0.79	5	9	0		1		64.4	92.7	0	
		mean	mean		∑	∑	∑	%	∑	%	mean	mean	∑	%
all thickness locations		-	-		89	109	5	4.6	4	3.7	-	-	1	0.9
surveillance locations		-20.7	15.0		36	46	3	6.5	2	4.3	16.6	13.6	1	2.2

* distance from the inner RPV wall

welding root region

surveillance specimen locations 2nd generation of WWER-440

Table A 11: Summary of J_R testing according to ASTM E1820 of SE(B) specimens from different thickness locations of the large scale thermally annealed and re-irradiated beltline welding seam SN0.1.4.of the Greifswald Unit 1 RPV (trepan 1-1).

thickness location		T	J_Q	K_{JQ}
code	distance*	°C	kJ/m^2	MPa√m
1-1.1.9.	8	200	140	162
1-1.3.19.	22	200	134	159
1-1.5.29.	36	200	148	167
1-1.6.40	46	200	151	169
1-1.8.49	59	200	239	212
1-1.11.70	83	200	135	159
1-1.14.90	107	200	167	177
1-1.15.99	118	200	151	168

* distance from the inner RPV wall

Table A 12: Summary of tensile test results measured on rectangular tensile specimens from different thickness locations of the large scale thermally annealed and re-irradiated forged base metal ring of the Greifswald Unit 1 RPV (trepan 1-4).

specimen geometry	thickness location		condition	parameter Eq. (6)							
				$R_{p0.2}$				R_m			
	code	distance		σ_{YG}	b	h	20°C	σ_{YG}	b	h	20°C
mm · mm		mm		MPa			MPa	MPa			MPa
3 · 4	1-4.2	15	IAI	415.5	468.1	0.00326	596	0	969.7	0.00111	700
3 · 4	1-4.6	49	IAI	501.2	760.1	0.00739	588	161.6	874.0	0.0017	693
1 · 2	1-4.10	84	IAI	534.0	1357.5	0.01195	575	516.8	647.9	0.00478	676
3 · 4	1-4.14	120	IAI	493.4	552.2	0.00640	578	0	953.8	0.00115	681
3 · 4	1-4.2&6&10&14	15-120	IAI	517.8	777.2	0.00845	583	267.3	743.0	0.00194	688

Table A 13: Charpy-V test results measured on compact Charpy V-notched specimens from different thickness locations of the of the large scale thermally annealed and re-irradiated forged base metal ring of the Greifswald Unit 1 RPV(trepan 1-4).

disc code	location* mm	Parameter Eq. (8)				TT_{47J}	USE
		A	B	C	T_0		
		J	J		°C	°C	J
1-4.3	22	105	95	27	35	16	200
1-4.5	43	105	95	40	42	14	200
1-4.8	66	105	95	30	29	8	200
1-4.12	101	103	98	30	25	6	201
all	22-101	105	95	38	25	-2	200

Table A 14 Summary of MC (ASTM E1921) test results measured on SE(B) specimens from different thickness locations of the large scale thermally annealed and re-irradiated forged bases metal ring 0.3.1. of the Greifswald Unit 1 RPV (trepan 1-4).

thickness location		ASTM E1921									SINTAP	VERLIFE		
code	distance* mm	T_0 °C	σT_0 K	$\sum n_i r_i$	r	N	$< K_{Jc-1T}^{2\%}$		$> K_{Jc-1T}^{98\%}$		T_0^{SINTAP} °C	RT_0 °C	$< K_{Jc-1T}^{VERLIFE}$	
1-4.1	8	-116.3	7.5	1.33	8	12	1		2		-66.4	-83.2	1	
1-4.4	32	-104.6	6.7	1.76	11	13	0		1		-91.3	-71.6	0	
1-4.7	56	-106.1	7.0	1.67	10	12	1		2		-31.7	-73.0	1	
1-4.9	77	-111.7	6.6	1.93	12	12	1		1		-71.5	-78.6	1	
1-4.11	90	-106.2	7.2	1.48	9	11	0		1		-89.5	-72.9	0	
1-4.13	111	107.5	6.6	2.00	12	12	1		0		-58-3	-74.4	1	
1-4.16	132	-119.5	7.0	1.67	10	12	2		2		-93.1	-86.4	0	
		mean	**mean**		∑	∑	∑	**%**	∑	**%**	**mean**	**mean**	∑	**%**
all thickness locations		-	-		72	84	6	7.1	9	10.7	-	-	4	4.8
surveillance locations		-107.2	2.7		54	60	3	5.0	5	8.3	-68.8	-74.7	3	5.0

* distance from the inner RPV wall

thickness location of surveillance specimens WWER-440 2nd generation

Table A 15 Summary of J_R testing according to ASTM E1820 of SE(B) specimens from different thickness locations of the large scale thermally annealed and re-irradiated forged base metal ring of the Greifswald Unit 1 RPV (trepan 1-4).

thickness location		**T**	**$J_{Q/IC}$**	**$K_{JQ/IC}$**	**Jc**	**K_{Jc}**
code	**distance***	**°C**	**kJ/m²**	**MPa√m**	**kJ/m²**	**MPa√m**
1-4.1.123	8	22	319	246		
1-4.1.124	8	-25	350	258		
1-4.4.152	32	22	333	251	416	281
1-4-7.179	56	23	299	238		
1-4.8.193	66	23	302	240		
1-4.8.194	66	-25	306	241		
1-4.9.204	77	21	345	256		
1-4.9.208	77	24	339	254	345	256
1-4.11.221	90	21	296	237		
1-4.11.222	90	-25	330	251	431	286
1-4.13.249	111	21	339	254		
1-4.16.263	132	24	233	211		
1-4.16.264	132	-25	333	252	382	270
mean	¼-T to ¾-T	RT	322	247		
SD	¼-T to ¾-T	RT	22	8		

J_c/K_{Jc} unstable failure or pop-in

Table A 16: Summary of tensile test results measured on rectangular tensile specimens from different thickness locations of the large scale thermally annealed beltline welding seam SN0.1.4. of the Greifswald Unit 2 RPV (trepan 2-3).

specimen geometry	thickness location		condition	parameter Eq. (6)							
				$R_{p0.2}$				R_m			
	code	distance		σ_{YG}	b	h	20°C	σ_{YG}	b	h	20°C
mm · mm		mm		MPa			MPa	MPa			MPa
3 · 4	2-3.2	15	IA	422.7	572.1	0.00736	489	0.0	865.7	0.00124	602
3 · 4	2-3.5	39	IA	412.1	1352.3	0.00969	491	0.0	1067.4	0.00192	608
3 · 4	2-3.9	73	IA	359.7	1818.2	0.01206	413	102.3	909.0	0.00241	551
3 · 4	2-3.13	107	IA	423.8	2936.9	0.01573	453	432.7	859.1	0.00629	569

Table A 17: Summary of MC (ASTM E1921) test results measured on SE(B) specimens from different thickness locations of the large scale thermally annealed beltline welding seam SN0.1.4. of the Greifswald Unit 2 RPV (trepan 2-3).

thickness location		ASTM E1921									SINTAP	VERLIFE		
code (Table A 3)	distance* mm	T_0 °C	σT_0 K	$\sum n_i r_i$	r	N	$< K_{Jc-1T}^{2\%}$		$> K_{Jc-1T}^{98\%}$		T_0^{SINTAP} °C	RT_0 °C	$< K_{Jc-1T}^{VERLIFE}$	
2-3.1	8	-37.8	8.4	1.00	6	9	2		0		-1.7	-4.0	0	
2-3.3	22	-37.9	7.2	1.36	9	9	0		1		-23.5	-4.1	0	
2-3.4	32	-12.3	7.5	1.17	8	10	0		1		-12.3	21.2	0	
2-3.6	46	-61.6	7.9	1.10	7	9	0		0		-61.6	-27.8	0	
2-3.7	56	-20.8	7.9	1.04	7	9	0		0		-20.8	13.0	0	
2-3.8	66	-42.7	8.4	1.00	6	10	1		0		-8.5	-9.2	0	
2-3.10	80	-30.6	7.9	1.07	7	10	1		0		1.8	2.9	0	
2-3.11	90	-7.1	9.0	0.83	5	10	2		0		24.9	26.4	0	
2-3.12	101	3.9	7.5	1.18	8	9	0		0		3.9	37.7	0	
2-3.15	123	6.2	7.5	1.19	8	9	0		1		22.6	40.0	0	
2-3.16	133	-13.6	7.2	1.45	9	10	2		1		62.4	19.9	1	
		mean	**mean**		$\sum$	$\sum$	$\sum$	**%**	$\sum$	**%**	**mean**	**mean**	$\sum$	**%**
all thickness locations		-	-		80	104	8	7.7	4	3.8	-	-	1	1.0
surveillance locations		-19.5	18.5		40	48	4	8.3	0	0	-0.8	14.0	0	0

* distance from the inner RPV wall

welding root region

surveillance specimen locations 2nd generation of WWER-440

Table A 18: Summary of tensile test results measured on rectangular tensile specimens from different thickness locations of the beltline welding seam SN0.1.4. of the Greifswald Unit 4 RPV (trepans 4-4 and 4-6)

specimen geometry	thickness location		condition	parameter Eq. (6)							
				$R_{p0.2}$				R_m			
	code	distance		σ_{YG}	b	h	20°C	σ_{YG}	b	h	20°C
mm · mm		mm		MPa			MPa	MPa			MPa
3 · 4	4-4&6.3	25	I	0.0	704.3	0.00077	562	518.5	534.8	0.00443	665
3 · 4	4-6.7	59	I	500.2	671.5	0.00784	568	426.5	657.0	0.00339	670
1 · 2	4-6.10	87					511*				661*
3 · 4	4-6.11	93	I	434.0	461.8	0.00532	531	497.4	517.1	0.00412	652
3 · 4	4-4.12	113	I	0.0	670.6	0.00102	497	0.0	818.6	0.00094	622
1 · 2	4-4.13	122	I				509*				621*
3 · 4	4-6.15	125	I	409.8	510.7	0.00602	497	517.8	624.7	0.00605	624
1 · 2	4-6.16	132	I				498*				609*
3 · 4 & 1 · 2	4-4&6.10&11&12	87-122	I	439.9	978.0	0.00887	513	368.2	614.7	0.00271	646
1 · 2	4-6.10	87	IA				439*				563
1 · 2	4-4.10	93	IA	0	676.2	0.00166	416	470.8	783.1	0.00763	555
1 · 2	4-4.13	122	IA				402*				553*
1 · 2	4-6.16	132	IA				395*				538*
1 · 2	4-4&6.10&13	87-122	IA	0.0	676.2	0.00166	416	470.8	783.1	0.00763	555

* mean value of 6 tests at 20°C

Table A 19: Charpy-V test results measured on compact Charpy V-notched specimens of the trepan 4-4 from different thickness locations of the beltline welding seam SN0.1.4. of the Greifswald Unit 4 RPV (trepan 4-4).

disc code	location* mm	condition	Parameter Eq. (8) A J	B J	C	T_0 °C	TT_{47J} °C	USE J
4-4.2	17	I	69	64	40	97	83	133
4-4.4	31	I	60	56	25	44	38	116
4-4.5	41	I	55	52	19	43	40	107
4-4.6	51	I	58	56	60	85	73	114
4-4.7	62	I	46	42	60	112	113	88
4-4.8	72	IA	88	86	56	44	15	174
4-4.9	82	I	59	56	76	136	119	115
4-4.10	93	IA	87	84	35	38	20	171
4-4.11	103	I	60	57	60	148	134	117
4-4.13	119	I	53	50	50	126	120	103
4-4.15	140	I	65	61	40	105	93	126
4-4.7-13.		I	63	60	80	149	127	123
4-4.8&10.		IA	89	86	41	43	21	175

* distance from the inner RPV wall

welding root region surveillance specimen locations 2nd generation of WWER-440

Table A 20: Summary of MC (ASTM E1921) test results measured on SE(B) specimens from different thickness locations of the beltline welding seam SN0.1.4. of the Greifswald Unit 4 RPV (trepans 4-4 and 4-6).

code	distance*	ASTM E1921									SINTAP	VERLIFE		
		T_0	σT_0	$\sum n_i r_i$	r	N	$< K_{Jc-1T}^{2\%}$		$> K_{Jc-1T}^{98\%}$		T_0^{SINTAP}	RT_0	$< K_{Jc-1T}^{VERLIFE}$	
	mm	°C	K								°C	°C		
4-6.2	18	26.2	7.9	1.10	7	10	1		0		46.7	59.7	0	
4-6.4	32	6.0	7.5	1.26	8	10	1		0		32.1	39.5	1	
4-6.5	42	24.6	7.0	1.52	10	10	0		1		33.1	58.1	0	
4-6.6	52	37.6	7.0	1.51	10	10	0		1		56.2	71.1	0	
4-6.8	66	74.2	7.5	1.26	8	10	0		0		76.6	107.7	0	
4-6.9	76	66.7	7.2	1.43	9	10	0		0		66.7	100.2	0	
4-6.10	87	59.4	7.5	1.15	8	10	3		0		92.0	92.9	0	
4-6.12	100	69.4	7.0	1.52	10	10	0		0		69.4	102.9	0	
4-6.12(RL)	100	75.3	7.5	1.26	8	9	0		0		84.0	109.1	0	
4-6.12(RR)	100	76.0	7.9	1.05	7	8	0		0		97.7	110.1	0	
4-4.11(RR)	103	71.8	7.5	1.33	8	8	0		1		90.0	105.9	0	
4-6.14	118	117.6	7.5	1.13	8	10	0		1		117.6	151.1	0	
4-6.14(RR)	118	81.8	7.9	1.17	7	10	0		0		92.0	115.3	0	
4-6.16	132	82.3	7.0	1.60	10	10	0		0		82.3	115.8	0	
4-4.14	132	103.3	7.2	1.36	9	9	0		0		103.3	137.1	0	
4-6.17	142	100.6	7.0	1.40	10	10	1		1		141.0	134.1	0	
		mean	**mean**		**∑**	**∑**	**∑**	**%**	**∑**	**%**	**mean**	**mean**	**∑**	**%**
all thickness locations		-	-		137	154					-	-	1	0.6
surveillance locations		76.9	7.5		73	85	3	3.5	2	2.4	87.3	110.6	0	0.6

* distance from the inner RPV wall

welding root region surveillance specimen locations 2nd generation of WWER-440

Table A 21: MC test results investigated on reconstituted thermally annealed (475 °C/152 h) specimens of beltline welding seam SN0.1.4. of the Greifswald Unit 4 RPV (trepans 4-4 and 4-6).

code	distance*	ASTM E1921							SINTAP	VERLIFE	
	mm	T_0 °C	σT_0 K	$\sum n_i r_i$	r	N	$< K_{Jc-1T}^{2\%}$	$> K_{Jc-1T}^{98\%}$	T_0^{SINTAP} °C	RT_0 °C	$< K_{Jc-1T}^{VERLIF}$
4-4.2&4-IA	25	-30.6	7.5	1.15	8	8	1	0	4.2	3.5	0
4-6.9-IA	76	-3.3	7.2	1.36	9	9	0	0	-3.3	30.5	0
4-6.9-IA	76	-39.3	9.0	0.98	6	7	1	0	-3.3	-2.7	0
4-6.10-IA	87	-6.2	7.2	1.36	9	9	1	0	42.9	27.6	1
4-4.11-IA	103	-7.6	7.2	1.43	9	9	1	0	39.3	26.2	1

* distance from the inner RPV wall

Table A 22: Charpy-V test results measured on Charpy V-notched specimens of the trepan 4-2 from the forged base metal ring 0.3.1. of the Greifswald Unit 4 RPV (trepan 4-2).

disc code	location* mm	A J	B J	C	T_0 °C	TT_{47J} °C	USE J
4-2.2	18	106	104	30	-27	-46	210
4-2.4	31	106	104	50	18	-14	210
4-2.5	42	104	102	50	-5	-37	206
4-2.6	52	112	108	30	5	-16	220
4-2.7	62	102	98	37	-10	-33	200
4-2.10	86	114	110	45	-6	-38	224
4-2.11	96	115	110	50	4	-32	225
4-2.14	122	113	110	40	-9	-37	223
4-2.15	132	118	115	48	-7	-42	233
4-2.16	143	113	110	40	-9	-37	223
all		114	110	57	-2	-42	224

Table A 23: Summary of tensile test results measured on rectangular tensile specimens from different thickness locations of the forged base metal ring 0.3.1. of the Greifswald Unit 4 RPV (trepans 4-1 and 4-2).

specimen geometry	thickness location		condition	parameter Eq. (6)							
				$R_{p0.2}$				R_m			
	code	distance		σ_{YG}	b	h	20°C	σ_{YG}	b	h	20°C
mm · mm		mm		MPa			MPa	MPa			MPa
3 · 4	4-2.3.	24	I	504.2	1190.3	0.01145	558	522.2	633.8	0.00507	678
3 · 4	4-1.3.	25	I	449.9	251.8	0.00288	558	0	837.0	0.000717	678
3 · 4	4-2.8.	69	IA	526.8	1232.5	0.01192	564	558.2	609.6	0.00571	673
3 · 4	4-1.9.	80	I	523.8	882.4	-0.01	571	570.9	661.7	0.00617	679
3 · 4	4-2.12.	104	I	539.7	1327.4	0.01306	567	565.7	690.1	0.00637	674
3 · 4	4-1.12.	107	I	541.3	1088.0	0.01282	576	584.4	506.4	0.0059	674
3 · 4	4-1-15	134	I	506.2	770.0	0.00852	570	591.5	920.6	0.00807	678
3 · 4	all	24 - 134	I	531.4	1104.7	0.01212	663	579.4	549.0	0.00593	674

Table A 24: Summary of MC (ASTM E1921) test results measured on SE(B) specimens from different thickness locations of the forged base metal ring 0.3.1. of the Greifswald Unit 4 RPV (trepan 4-1).

code	distance* mm	ASTM E1921 T_0 °C	σT_0 K	$\sum n_i r_i$	r	N	$< K_{Jc-1T}^{2\%}$		$> K_{Jc-1T}^{98\%}$		SINTAP T_0^{SINTAP} °C	VERLIFE RT_0 °C	$< K_{Jc-1T}^{VERLIFE}$	
4-1.2	18	-116.4	7.9	1.17	7	11	1		0		-90.9	-83.1	0	
4-1.4	32	-129.5	11.1	0.50	3	12	2		0		44.4	-96.4	1	
4-1.5	42	-116.6	6.7	1.83	11	13	0		0		-105.2	-83.6	0	
4-1.6	52	-109.9	6.7	1.83	11	12	1		0		-50.6	-76.8	1	
4-1.7	63	-113.4	7.0	1.67	10	11	0		1		-100.8	-80.1	0	
4-1.8	73	-119.6	7.2	1.50	9	12	0		0		-119.6	-86.5	0	
4-1.10	87	-123.8	7.0	1.67	10	12	2		0		-94.5	-90.7	0	
4-1.11	97	-126.6	7.2	1.50	9	12	3		0		32.7	-93.5	2	
4-1.13	117	-123.9	7.2	1.50	9	12	3		0		-35.8	-90.8	2	
4-1.14	127	-124.2	6.7	1.83	11	12	2		0		-86.9	-91.1	1	
4-1.16	141	-130.7	7.0	1.67	10	12	3		0		n.d.	-97.6	2	
		mean	**mean**		∑	∑	∑	**%**	∑	**%**	**mean**	**mean**	∑	**%**
all thickness locations		-	-		100	131	17	13.0	1	0.8	-	-	9	6.9
surveillance locations		-119.1	6.1		69	84	9	10.7	1	1.2	-74.0	-86.0	5	5.9

n.d.: not determinable (infinite value)

* distance from the inner RPV wall

thickness location of surveillance specimens WWER-440 2nd generation

Table A 25: Summary of J_R testing according to ASTM E1820 of SE(B) specimens from different thickness locations of the forged base metal ring of the Greifswald Unit 4 RPV (trepan 4-1).

thickness location		T	$J_{O/IC}$	$K_{JO/IC}$	Jc	K_{Jc}
code	distance*	°C	kJ/m²	MPa√m	kJ/m²	MPa√m
4-1.4.41	32	-25	427	285	439	289
4-1.5.65	42	-25	389	272	458	295
4-1.6.79	52	-25			359	262
4-1.6.80	52	20	350	258		
4-1.7.93	63	-25			371	266
4-1.7.94	63	23	372	266		
4-1.8.107	73	-25			147	167
4-1.8.108	73	22	372	266		
4-1.10.129	87	-25			369	265
4-1.10.132	87	22	429	286		
4-1.11.145	97	-25	423	284		
4-1.11.146	97	-50			227	208
4-1.13.173	117	-25			444	291
4-1.13.174	117	23	393	273		
4-1.14.187	127	-25				
4-1.14.188	127	-50			251	219
4-1.16.211	141	-25			332	251
4-1.16.212	141	22	433	287		

* distance from the inner RPV wall, J_c/K_{Jc} unstable failure or pop-in

Table A 26: Summary of MC (ASTM E1921) test results measured on SE(B) specimens from the WWER/V213 surveillance thickness locations of the forged base metal rings 0.3.1. and beltline welding seam of the investigated Greifswald RPVs.

Unit	material	con-dition	ASTM E1921							SINTAP	multi modal					VERLIFE	
			T_0 °C	σT_0 K	$\sum n_i r_i$	r	N	$< K_{Jc-1T}^{2\%}$	$> K_{Jc-1T}^{98\%}$	T_0^{SINTAP} °C	T_0^{MM} °C	σ K	$< K_{Jc-1T}^{2\%}$	$> K_{Jc-1T}^{98\%}$	RT_0 °C	$< K_{Jc-1T}^{VERLIF}$
1	SN0.1.4.	IAI	-25.4	4.9	6.48	42	55	7	4	15.9	-16	35	2	0	6.1	0
1	0.3.1.	IAI	-108.7	4.8	7.36	45	49	4	1	-59.2	-100	23	2	0	-82.8	3
2	SN0.1.4.	IA	-26.4	5.1	5.17	32	48	7	4	-0.3	-20	33	0	0	5.2	0
4	SN0.1.4.	I	74.3	4.5	12.11	77	94	2	4	83.9	82	21	0	0	105.6	0
4	SN0.1.4.	IA	-20.8	5.3	4.48	28	34	3	2	18.8	-14	21	2	0	11.0	0
4	0.3.1.	I	-119.8	4.5	11.50	69	84	9	2	-34.7	-116.0	17	5	0	-88.5	1

Table A 27: Summary of tensile test results measured on miniature tensile specimens from the cladding of the Greifswald Unit 4 RPV (trepans 4-1, 4-2, 4-4 and 4-6).

specimen geometry mm · mm	trepan	code	layer	parameter Eq. (6)									
				$R_{p0.2}$					R_m				
				σ_{YG} MPa	b	h	20°C MPa	270°C MPa	σ_{YG} MPa	b	h	20°C MPa	270°C MPa
1 · 2	4-1	4-1.1.	1	0.0	590.1	0.00099	442	345	436.8	2327.2	0.00829	642	463
1 · 2	4-1	4-1.1.	2	301.9	305.8	0.00317	423	357	430.4	3414.0	0.00948	643	450
1 · 2	4-6	4-6.1.	1	62.6	603.6	0.00132	473	357	392.1	1481.9	0.006	648	449
1 · 2	4-6	4-6.1.	2	282.5	569.1	0.00527	404	315	400.0	3394.7	0.0096	604	418
1 · 2	4-1, 4-6	4-1.1., 4-6.1.	1	0	629.8	0.00108	459	350	417.7	1830.8	0.00712	645	456
1 · 2	4-1, 4-6	4-1.1., 4-6.1.	2	290.6	410.2	0.0041	414	335	415.1	3401.0	0.00954	623	434

Table A 28: Summary of the crack initiation J values, J_Q, and the converted fracture toughness values, K_{JQ}, of the investigated overlay cladding from the forged base metal ring 0.3.1 of the Greifswald Unit 4 RPV (trepan 4-1 and 4-2).

specimen code	T °C	E_{eff} (a_0) GPa	J_Q kJ/m^2	K_{JQ} MPa√m	specimen code	T °C	E_{eff} (a_0) GPa	J_Q kJ/m^2	K_{JQ} MPa√m
4-1.1.1	25	202.2	175	172	4-2.1.1.	22	208.1	166	168
4-1.1.2	-25	206.0	119	143	4-2.1.2.	50	206.6	175	172
4-1.1.3	-50	215.6	84	120	4-2.1.3.	100	204.6	153	159
4-1.1.4	0	207.8	124	146	4-2.1.4.	150	210.3	156	160
4-1.1.5*	-75	202.9	36	79	4-2.1.5.	200	202.5	181	171
4-1.1.6	100	203.0	238	199	4-2.1.6.	270	194.5	134	146
4-1.1.7	200	197.1	130	145	4-2.1.7.	75	204.1	162	165
4-1.1.8	270	208.1	100	125	4-2.1.8.	125	199.4	152	158
4-1.1.9	50	206.5	128	147	4-2.1.9.	175	207.4	126	143
4-1.1.10	75	206.2	304	226	4-2.1.10.	225	199.7	103	128
4-1.1.11	150	214.5	181	172	4-2.1.11.	250	190.9	118	137
4-1.1.12	250	201.8	156	157	4-2.1.12.	275	194.1	125	141
4-1.1.13	125	201.6	133	148	4-2.1.13.	23	208.4	146	157
4-1.1.14	50	199.8	125	145	4-2.1.14.	200	209.0	98	126

* unstable failure: J_c value

Table A 29: Summary of the crack initiation J values, J_Q, and the converted fracture toughness values, K_{JQ}, of the investigated overlay cladding from the welding seam SN0.1.4. of the Greifswald Unit 4 RPV (trepans 4-4 and 4-6).

specimen code	T °C	E_{eff} (a_0) GPa	J_Q kJm^{-2}	K_{JQ} MPa√m	specimen code	T °C	E_{eff} (a_0) GPa	J_Q kJm^{-2}	K_{JQ} MPa√m
4-4.1.1	22	202.3	91	124	4-6.1.2	-25	176.2	161	168
4-4.1.2	50	192.1	153	161	4-6.1.3	-50	188.0	114	140
4-4.1.3	100	191. 1	160	163	4-6.1.4	-75	196.8	51	94
4-4.1.4	150	204.2	112	135	4-6.1.5*	-25		82	118
4-4.1.5	200	202.8	60	99	4-6.1.6	0	193.3	131	150
4-4.1.6	268	196.7	115	135	4-6.1.7	-37	186.4	96	129
4-4.1.7	22	194.6	120	143	4-6.1.8*	-100	188.9	41	85
4-4.1.8	50	202.9	103	132	4-6.1.9	100	188.1	104	132
4-4.1.9	100	202.2	91	123	4-6.1.10	50	188.7	161	165
4-4.1.10	150	197.7	95	125	4-6.1.11	150	184.1	116	138
4-4.1.11	200	201.0	92	122	4-6.1.12	25	192.7	187	179
4-4.1.12	270	193.4	72	106	4-6.1.13	200	183.7	116	137
4-4.1.13	0	198.3	126	147	4-6.1.14	270	188.4	89	119
4-4.1.14	0	202.3	104	133					

* unstable failure: J_c value

HZDR
HELMHOLTZ
ZENTRUM DRESDEN
ROSSENDORF

Bautzner Landstr. 400
01328 Dresden, Germany
Tel. +49 351 260-3246
Fax +49 351 260-13246
h.w.viehrig@hzdr.de
http://www.hzdr.de